PROTEIN AND HYDRATION SHELL DYNAMICS OF ZN^{II}-SUBSTITUTED CYTOCHROME *C*

By

Jennifer Jo Mueller

A DISSERTATION

Submitted to
Michigan State University
in partial fulfillment of the requirements
for the degree of

Chemistry—Doctor of Philosophy

2013

PROTEIN AND HYDRATION SHELL DYNAMICS OF ZN^{II}-SUBSTITUTED CYTOCHROME *C*

By

Jennifer Jo Mueller

This dissertation describes two studies that provide new information on the nature of the protein and solvent dynamics that is probed in Zn^{II}-substituted cytochrome *c* (ZnCytc) by the intrinsic Zn^{II} porphyrin, which serves as a probe of the surrounding protein and solvent.

In the first study, the nature of the partially unfolded structures that are generated in ZnCytc upon optical excitation significantly above the vibronic origin of the Q ($S_0 \rightarrow S_1$, $\pi \rightarrow \pi^*$ transition) band was investigated using continuous-wave fluorescence spectroscopy. The results show that step-like transitions of the fluorescence Stokes shift correspond to the activation threshold for changes in structure from the native state to a partially unfolded state associated with the Ω loop formed by residues 20–35, which is adjacent to the Cys14 and Cys17 thioether linkages from the porphyrin to the polypeptide backbone. The excitation energy for optical formation of the unfolded state is consistent with the previous determination by Englander and coworkers using hydrogen-exchange NMR spectroscopy in ferrocytochrome *c* in the presence of Gdm^+.

In the second study, the hydration shell of ZnCytc was probed using the indolecyanine dye Cy5 using femtosecond pump–continuum-probe spectroscopy. Cy5 was attached to a surface lysine residue by a flexible linker so that it senses the

viscosity of the surrounding medium owing to its nonpolar solvation response. The main conclusion of this work is that the hydration shell is as much as 200 times as viscous as bulk water. A simple structural interpretation of this finding is that longer or more persistent chains of hydrogen-bonded water molecules are present than in the bulk.

DISCLAIMER AND COPYRIGHT CLAUSE

The views expressed in this work are those of the author and do not necessarily reflect the official policy or position of the Department of the Navy, Department of Defense, or the United States Government.

I am a military service member. This work was prepared as part of my official duties. Title 17, USC, §105 provides that 'Copyright protection under this title is not available for any work of the U.S.Government.' Title 17, USC, §101 defines a U.S. Government work as a work prepared by a military service member or employee of the U.S. Government as part of that person's official duties.

TABLE OF CONTENTS

LIST OF TABLES

LIST OF FIGURES

KEY TO ABBREVIATIONS

3PEPS, three-pulse photon echo peak shift

Chl, chlorophyll

ESA, excited state absorption

fbCytc, free-base cytochrome *c* (metal-free)

FeCytc, ferric cytochrome *c*

FRET, Förster resonance energy transfer

FSS, fluorescence Stokes shift

fwhm, full-width at half maximum

Gdm^+, guanidinium ion

HX-NMR, hydrogen-exchange nuclear magnetic resonance imaging

IVE, intramolecular vibrational excitation

IVR, intramolecular vibrational redistribution

LH, light-harvesting

LHCII, light-harvesting complex II

LP-SVD, linear prediction-singular value decomposition

Lut, lutein

MALDI-TOF MS, matrix-assisted desorption/ionization time-of-flight mass spectrometry

Neo, neoxanthin

NHS, N-hydroxysuccinimidyl

NPQ, non-photochemical quenching

OPA, optical parametric amplifier

PB, photobleaching

Vio, violaxanthin

RC, reaction center

SE, stimulated emission

ZnCytc, zinc^{II}-substituted cytochrome *c*

CHAPTER 1

Background and Significance

Summary

This dissertation presents two studies of protein and solvent dynamics in a model for a single-chlorophyll-binding chromoprotein: Zn^{II}-substituted cytochrome *c* (ZnCytc.) The main goals of this work were to determine how the structure of the protein dissipates excess vibrational energy and to determine how the surrounding hydration shell is coupled to and damps these protein motions. This is particularly relevant to photosynthetic systems, which use chromophores to absorb a broad solar spectrum and harmlessly dissipate unneeded energy. The single Zn^{II} porphyrin in ZnCytc is an analog to the photosynthetic chromophores and acts as an intrinsic probe in these studies. An additional point of significance that is distinct from photosynthesis comes from the possibility that the vibrational excitation can be used to generate partially unfolded structures. The proteins could then be studied as they refold spontaneously.

In this first chapter, we review the background for these two areas with an emphasis on the theory of protein folding, previous studies and the background that led to this work, and a brief review of photosynthesis. The goal of the first part of this work was to test hypotheses proposed in previous research on intramolecular vibrational excitation (IVE). IVE was proposed as a method to study protein unfolding and refolding as an alternative to current methods which rely on chemical

and thermal denaturation. The significance of this question relates to using a new method to reproducibly denature a protein under solution conditions favoring the native state using vibration obtained via optical excitation and to provide further insight into transfer of vibrational energy in photosynthetic systems. The goal of the second part of this work was to study differences in the behavior of water molecules in the hydration shell of a protein compared to water molecules in bulk water. The results indicate that water molecules in the hydration shell of ZnCytc exhibit higher viscosity than water molecules in the bulk, which hinder motion of other molecules in that region. These findings improve our understanding of the role played by the hydration layer in stabilizing the native fold and damping its unfolding motions.

1.1 Energy Landscape and Protein-Folding Funnel Theory

Proteins in solution tend to exhibit two states, the native state and the denatured state, but a microscopic analysis of protein crystal structure suggests a number of alternate conformations. The energy landscape/protein-folding funnel picture is an attempt to rationalize this paradox. The energy landscape picture introduced by Frauenfelder, Sligar, and Wolynes,[1] is a way to describe the potential energy of a protein as a function of protein conformations. The potential-energy surface is envisioned as a surface modulated by very large number of minima, which define the different conformations that the polypeptide can adopt. The barriers between these minima sort the landscape into tiers according to their heights compared to thermal fluctuations ($\Delta E = k_{\mathrm{B}}T$). Under specific solution conditions and at a given temperature, there are many possible conformations for a protein. The full energy landscape encompasses all conformational states the protein can access given a full range of solution conditions and temperatures. Under solution conditions favoring the native state, a protein is free to access only the part of the energy landscape with low energy barriers between potential wells. In order to reach another tier on the hierarchy of conformational states, more activation energy is required. The native state can be disrupted by adding energy in the form of heat, which can overcome the activation barriers, or by adding a denaturant, which can alter the shape of the activation barriers and allow access to previously inaccessible conformations.

Onuchic and Wolynes[2] suggested that the energy landscape for a biologically active polypeptide is a funnel-shaped landscape that leads an unfolded protein toward the native state as it seeks lower energy configurations, with the native state

at the minimum of the potential energy surface. Under solution conditions that favor the native state, the protein is effectively trapped at the bottom of the potential energy well. Adding heat to the system by increasing the temperature will allow the protein to sample more conformations, effectively climbing the sides of the funnel. Alternatively, adding a denaturant to the system alters the shape of the energy landscape, which may also allow the protein to sample a wider variety of conformations than are accessible under native-state conditions. It is expected that there are a variety of paths along the energy landscape/protein-folding funnel for a protein to follow as it approaches the native state rather than a single sequential pathway following specific intermediate states.[3-5] This leads to the questions of how protein intermediates move toward the native state, whether these pathways can be observed, and how the hydration shell of the protein is involved in directing motion over activation barriers along the energy landscape.

1.2 Dynamic Solvation

The study of dynamic solvation investigates how solvent molecules move or are reorganized in response to a change in chemical or electronic structure of a solute. In liquids, solvent dynamics have frequently been studied using time-resolved fluorescence spectroscopy. After optical excitation, the fluorescence spectrum shifts to the red because the solvent molecules reorganize around the fluorescent probe solute, which typically has a larger dipole moment in the excited state. Nonpolar solvation involves reorganization due to changes in the probe's structure or size as a result of the optical excitation.

1.2.1 Dynamic Solvation in Proteins

The fluctuations of proteins due to diffusive motion on the energy landscape from minimum to minimum can be characterized using a similar approach to that used to characterize dynamic solvation in liquids. The first work in this area was performed by McLendon, Mukamel, and coworkers,[6] who characterized the fluorescence Stokes' shift (FSS) response of apomyoglobin with an extrinsic chromophore. Replacement of the native heme with a fluorescent porphyrin makes the myoglobin suitable for picosecond spectroscopy experiments. Similar experiments were performed by the Beck group on the femtosecond timescale in in the alpha subunit of C-phycocyanin and in ZnCytc.[7] Equilibrium fluctuations can be measured in proteins by dynamic solvation because proteins exhibit some properties of liquids.[8] By treating a protein in solution as a liquid, responses can be studied using dynamic Stokes shift experiments[7,9,10] Using time-resolved fluorescence spectroscopy, Beck and Tripathy showed that the activation enthalpy for unfolding of free-base cytochrome *c* (fbCytc) is significantly lower than for ZnCytc (structure of cytochrome *c* shown in Figure 1.1) and that the time scales of dynamic solvation change due to structural perturbation. They also showed that the fluorescence Stokes shift (FSS) response function of fbCytc is significantly slower than that of ZnCytc, due to an increase of core and surface fluctuations relative to ZnCytc.[9]

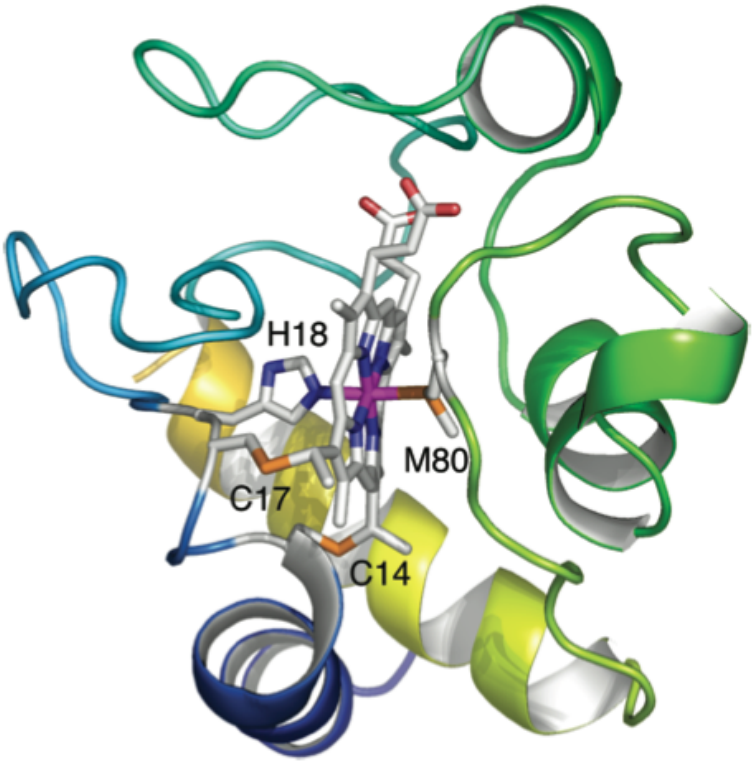

Figure 1.1. Structure of horse heart ferricytochrome *c* (1HRC.pdb) obtained by x-ray crystallography.[11] Reprinted with permission from Tripathy and Beck, 2010 American Chemical Society. The porphyrin is shown as a stick figure. The cysteine ligands, Cys14 and Cys17, and axial ligands, His18 and Met80, are also shown as stick structures. The protein is otherwise shown as ribbons. The iron center of the porphyrin is shown in magenta. The metal-center is removed in fbCytc. ZnCytc is obtained by replacing the iron center with Zn^{II}.[9] For interpretation of the references to color in this and all other figures, the reader is referred to the electronic version of this dissertation.

1.2.2 Fluorescence Stokes Shift Response of ZnCytc

Tripathy and Beck reviewed the theory and application of the FSS response in their studies of dynamic solvation in liquids and in proteins.[9] The potential energy curve of the excited state of the intrinsic chromophore was thought to be shifted horizontally along the solvation coordinate relative to the potential energy curve of the ground state (see Figure 1.2). The expected shift meant that the excited molecule was not at the equilibrium position on its potential energy curve, so forces on the

molecule pushed it toward equilibrium. Subsequently, when the molecule relaxed by emitting radiatively, the energy gap between the ground and excited states was smaller than the gap of the vertical transition from equilibrium position of the ground state to the excited state. Thus, the time-resolved fluorescence spectrum shifts to the red as time increases and eventually reaches an equilibrium value. These shifts were measured from a set of picosecond time-resolved fluorescence spectra, which were obtained as slices of a time–intensity–wavelength surface assembled from a series of single-wavelength fluorescence transients acquired with the detection wavelength scanned across the fluorescence spectrum. Time-resolved spectra were obtained by assembling the data as a time-wavenumber-intensity surface and slicing the surface at specific delay times.

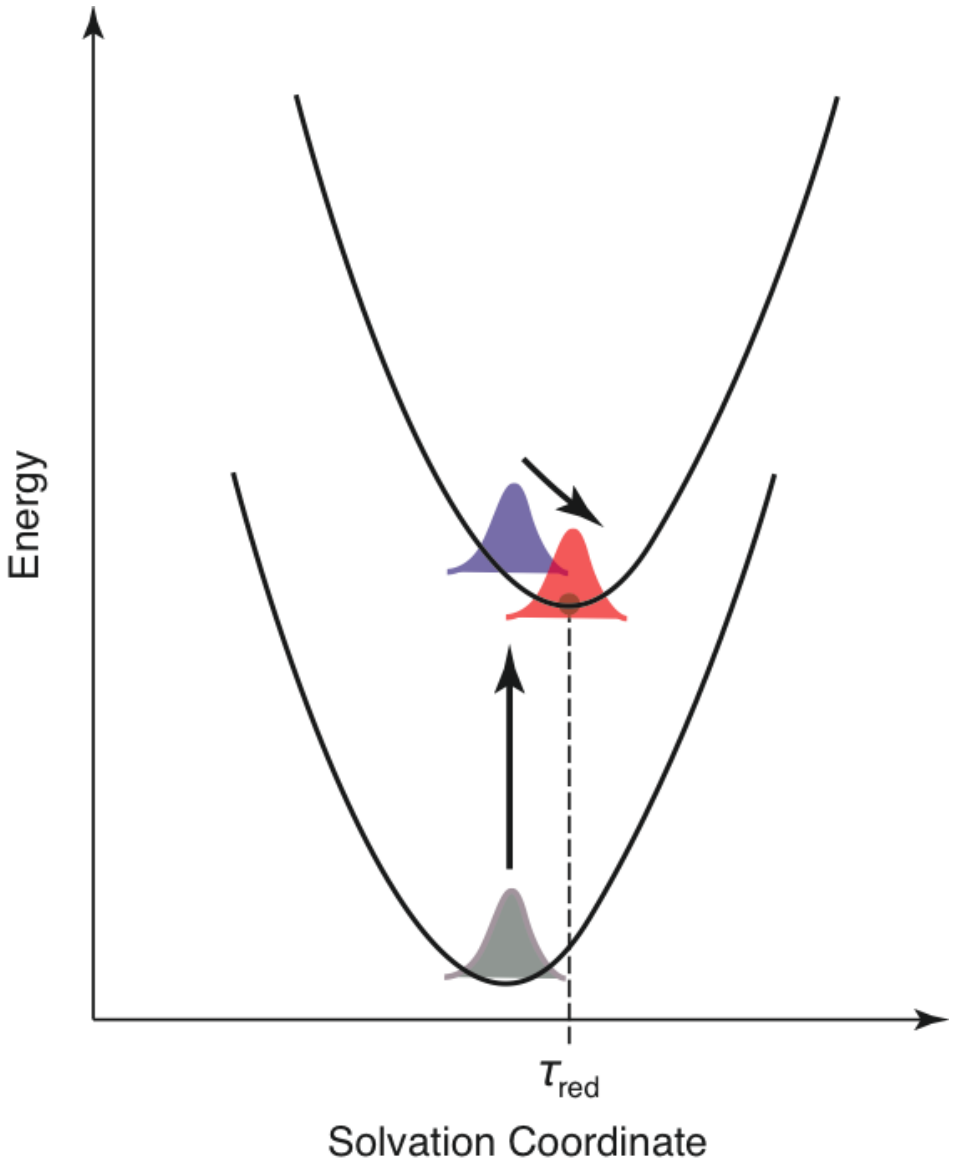

Figure 1.2. Potential energy curves representing the ground state (bottom) and excited state (top) showing the change in energy gap between the two states following optical excitation. Upon excitation, a vertical transition occurs. Due to a small shift along the solvation coordinate, the molecule is not at the lowest energy state of the excited-state potential energy curve. As the system moves toward equilibrium in the excited state, the energy gap decreases, resulting in a red shift of fluorescence. After Maroncelli *et al.*, 1994.[12]

The FSS is also called the solvent-response function, $S_\nu(t)$[13-16] It describes reorganization of solvent molecules surrounding a molecule in a condensed phase medium that occurs after electronic excitation. An electronic excitation from the

ground state to the first excited state, S_1, is generally accompanied by a change in the dipole moment of the molecule, the probe chromophore.[9] $S_\nu(t)$ has been defined using the time evolution of the mean frequency of the time-resolved fluorescence spectrum:

$$S_\nu(t) = \frac{\nu(t) - \nu(\infty)}{\nu(0) - \nu(\infty)} \tag{1.1}$$

In polar liquids, most properties of $S_\nu(t)$ observed experimentally have been calculated by treating the solvent as a dielectric continuum.[13,17] The Beck Lab has treated the optical transition of the probe as a step-function change in the electric field to which surrounding solvent molecules react.[9] There are fluctuations of the local electric field due to random motions of solvent molecules and the change in orientation of their dipole moment around the chromophore. These fluctuations help to understand the molecular character of $S_\nu(t)$.[9] In the time domain, the ground-to-excited state transition frequency, $\omega = 2\pi\nu$, of the probe exhibits fluctuations from the frequency averaged over time or the frequency averaged instantaneously over the ensemble. Those fluctuations are described by a time-correlation function for the probe's optical transition, $M(t)$,

$$M(t) = \frac{\Delta\omega(0)\Delta\omega(t)}{(\Delta\omega)^2} \tag{1.2}$$

that describes the loss of memory of the system over time. $M(t)$ is equivalent to the fluorescence Stokes' shift in the linear response regime where the fluctuation-dissipation relation holds. $M(t)$ is determined from the time averaged and instantaneous ground-to-excited state transition frequencies, ω and $\omega(t)$,

respectively, and $\Delta\omega(t)=\omega-\omega(t)$, the fluctuation averaged over the ensemble.[13,14] At reference time, t=0, there is no loss of memory of the instantaneous transition frequency, $\omega(0)$, but as time evolves, the system retains less and less of its character from t=0.[9]

The memory function, $M(t)$, is equal to $S_V(t)$ at high temperatures and in the linear response regime. Most probe/solvent systems have a linear response because excitation of the chromophore usually results in a small change in the dipole moment of the molecule and therefore effects a small perturbation to the motions and structure of the solvent molecules.[18,19]

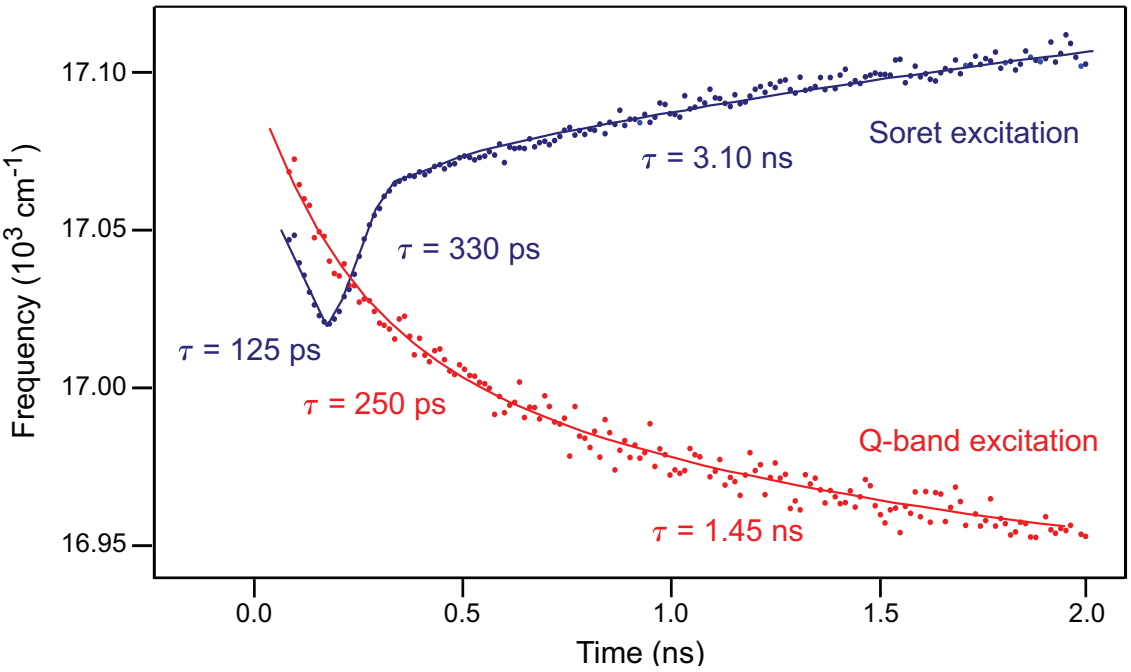

Figure 1.3. Dynamic Stokes shift of the ZnCytc fluorescence spectrum. Reprinted with permission from Lampa-Pastirk and Beck, 2006, American Chemical Society. The response shows an initial red-shift followed by a blue-shift of fluorescence for ZnCytc in water at room temperature following excitation in the Soret band (blue) and a red-shift following excitation of the Q-band (red). In each case, the center frequency of the 0-0 transition was plotted as a function of time delay after excitation.[20]

By using three solvents to vary viscosity and polarity, water, a water/glycerol mixture, and a water/methanol mixture, the Beck Lab was able to compare effects on the FSS. In water, there is an initial red shift, then a blue shift. At increased viscosity, the initial red shift is smaller, the turn-around is delayed, and the blue shift is slower. At lower viscosity, there is half the blue shift relative to pure water, no initial red shift, and a final red shift. It is likely that the initial red shift is not visible at low viscosity because it occurs on a time scale shorter than can be observed with the instrument that was used. The final red shift that is observed at low viscosity is not observed at high viscosity, presumably because it occurs too late to be detected. Overall, there are three phases, an initial red shift that includes unfolding motions and solvent entering the hydrophobic core, a blue shift when the structure is comparable to the thermally unfolded equilibrium state, and a final red shift that occurs during refolding and relaxation back to the native state.[20]

There are two main and independent factors that affect the three phases. Activation energy barrier height and hydrodynamic friction both affect the transition between phases and are completely independent of each other. Lower polarity corresponds to lower activation energy barrier height. Lower viscosity corresponds to lower solvent friction. Friction between the solvent and exposed peptides contributes directly to the kinetic control of the product state. The observations made by the Beck Lab suggest that the transition state more closely resembles the unfolded state than the native state and that perturbation by temperature or solution composition involves macroscopic state changes.[20]

It is thought that the vibrational energy is transferred from the chromophore to the protein by intramolecular vibrational redistribution (IVR) through Cys14 and Cys17, not through the binding site peptides.[11] Though the vibrational energy is ultimately transferred to the solvent, transfer to the solvent is slow, on the order of 20 ps, which allows the protein to be affected by the vibrations. These effects can result in small structural changes, leading to stages of unfolding.[20] The data showed an unusual bidirectional response with excitation of the Soret band and a biexponential shift in the time-resolved fluorescence spectrum when excited at 584nm (see Figure 1.3). The fast component is thought to be random motions of the hydrophobic core. The slow component is due to motions of the protein in areas contacting solvent.[20]

1.2.3 Intramolecular Vibrational Excitation

Intramolecular Vibrational Excitation (IVE) experiments in the Beck Lab have used optically-driven excitation from the ground state into multiple vibrational levels above the first excited state.[20] If there is energy in excess of the gap between the S_0 and S_1 states that optically excites a chromophore, the excited molecule will relax to the lowest vibrational state of the first excited electronic state before relaxing to the ground state by emitting a photon or sometimes relaxes vibrationally before transferring excitation to another chromophore in the photosynthetic system. The vibrational relaxation occurs by transferring energy to the surrounding media, in this case, a protein. The transfer of excess vibrational energy to the protein occurs within 2-4 ps.[21,22] The protein ultimately transfers the vibrational energy to

the surrounding solvent.[20] IVE experiments present an integrated response rather than the time-resolved response shown in the aforementioned studies.

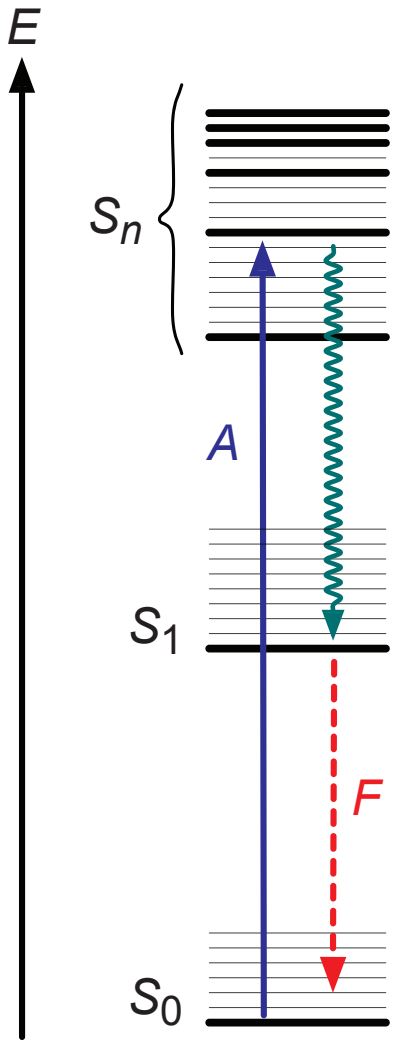

Figure 1.4. Electronic and vibrational energy levels as found in molecules like the porphyrin of ZnCytc. Reprinted with permission from Lampa-Pastirk and Beck, 2006, American Chemical Society. After an initial optical excitation (blue), vibrational relaxation to the S_1 state occurs (green), followed by fluorescence emission (red).[20]

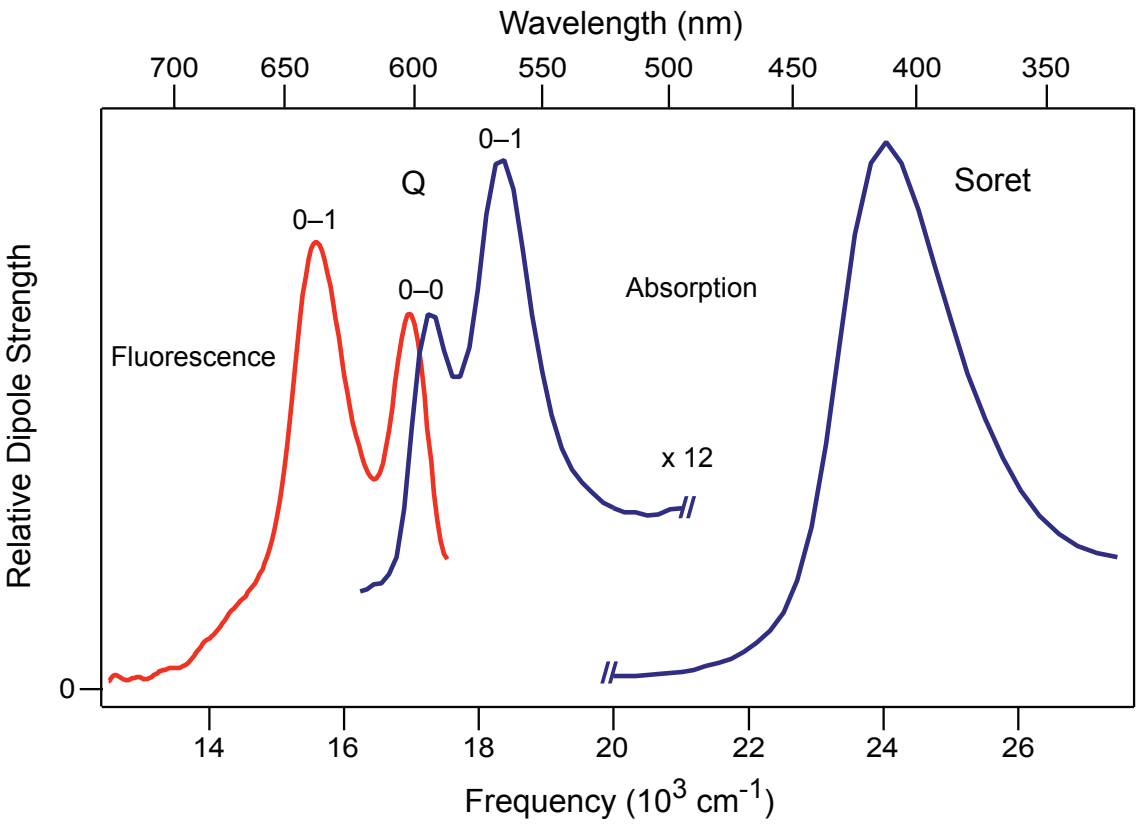

Figure 1.5. Absorption (A) and fluorescence (F) dipole strength spectra obtained at room temperature. Reprinted with permission from Lampa-Pastirk and Beck, 2006, American Chemical Society. The vibrational structure of the Q-band absorption and fluorescence spectra is due to the 0-0 and 0-1 vibronic transitions.[20]

As described earlier, an ensemble of folding trajectories would be expected based on the protein-folding funnel potential energy surface hypothesis. The native state of the protein is expected to be at the lowest point on the potential energy surface.[23,24] Research using IVE performed by the Beck Lab has shown that an ensemble of folding trajectories may not accurately describe the ZnCytc system because the results were interpreted in terms of a specific pathway between three partially unfolded states.[20]

The time-resolved fluorescence spectrum of ZnCytc exhibits a conventional shift to the red with excitation in the Q absorption band. This shift occurs as vibrational

energy is transferred from the porphyrin to the protein. As the protein acquires increased vibrational energy, it begins to unfold. The time scale of IVR is thought to be long enough for partial unfolding to occur. By changing the excitation wavenumber, the amount of vibronic energy transferred to the protein can be varied. IVE of the protein structure results in at least three partially unfolded states along a specific pathway. Along this pathway, three main transitions are observed in both ZnCytc and fbCytc. There is an initial red shift, then a blue shift, and a shift back to the red, though the net shift is blue.[25]

The transitions of the IVE profile (Figure 1.6A), which appear to mark activation enthalpies for displacements of the native structure to partially unfolded states, occur at roughly the same position as the transitions of the F_{0-1} / F_{0-0} plot (Figure 1.6B) and also those of the Soret band. Figure 1.6C shows that there is overall narrowing of the 0-0 peak, but the change is small, less than 5%, while local melting would be expected to broaden the line width as excitation shifted blue.[25]

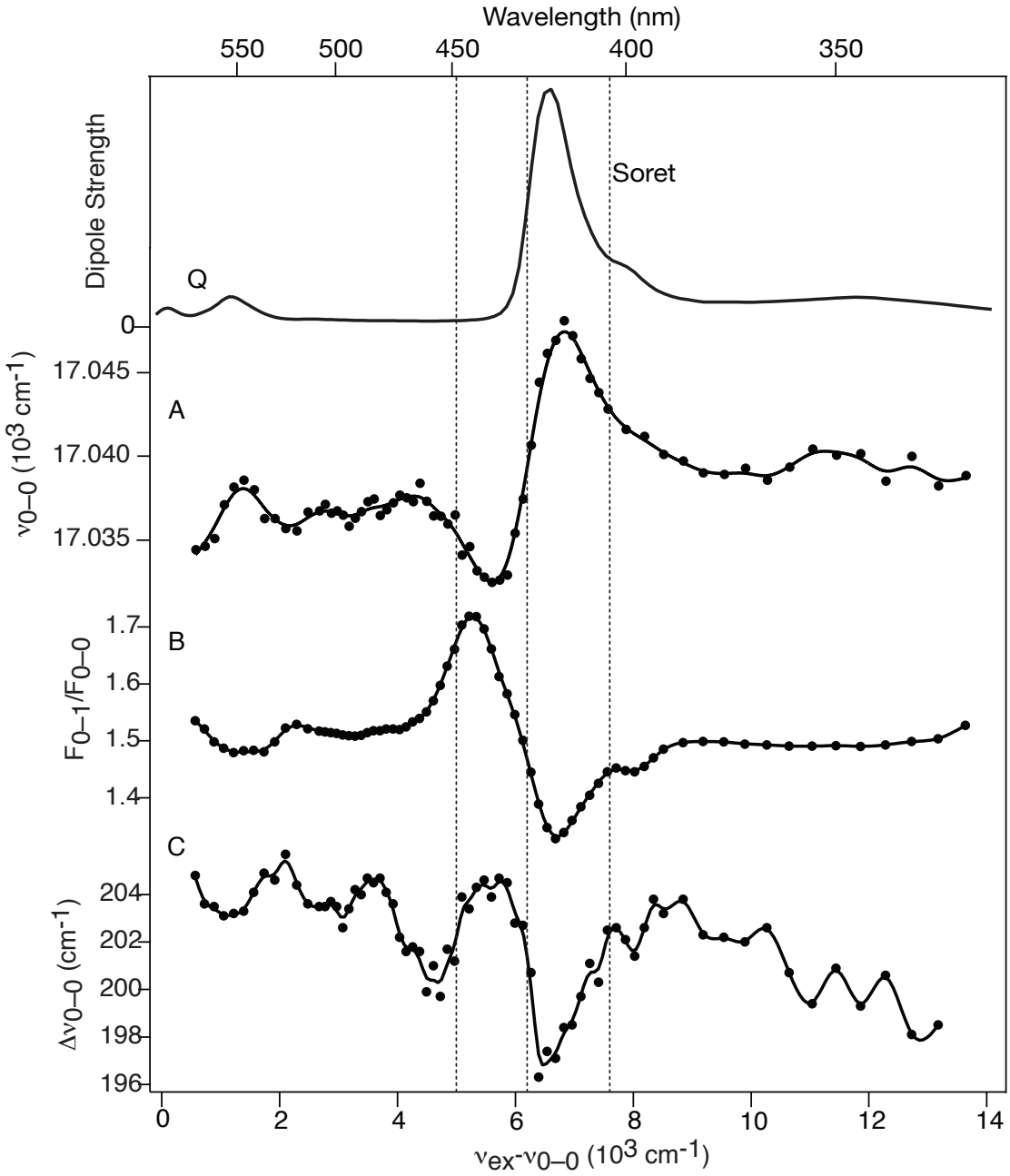

Figure 1.6. Dependence of the fluorescence spectrum from ZnCytc at 22°C on the intramolecular vibrational excitation: (A) the integrated Stokes shift, as determined by the wavenumber of the 0-0 peak maximum, ν_{0-0}; (B) ratio of the dipole strengths of the 0-1 and 0-0 peaks, F_{0-1} / F_{0-0}; and (C) the half-width at half-maximum of the 0-0 peak, $\Delta\nu_{0-0}$. The plotted abscissa is the intramolecular vibrational excitation, the difference between the excitation wavenumber and that of the 0-0 vibronic transition. At the top of the figure, the absorption dipole strength spectrum is plotted with respect to the same abscissa scale. The vertical dashed lines mark the excitation energies corresponding to apparent activation enthalpies for three protein-unfolding transitions. Reprinted with permission from Barns *et al.*, 2008, American Chemical Society.[25]

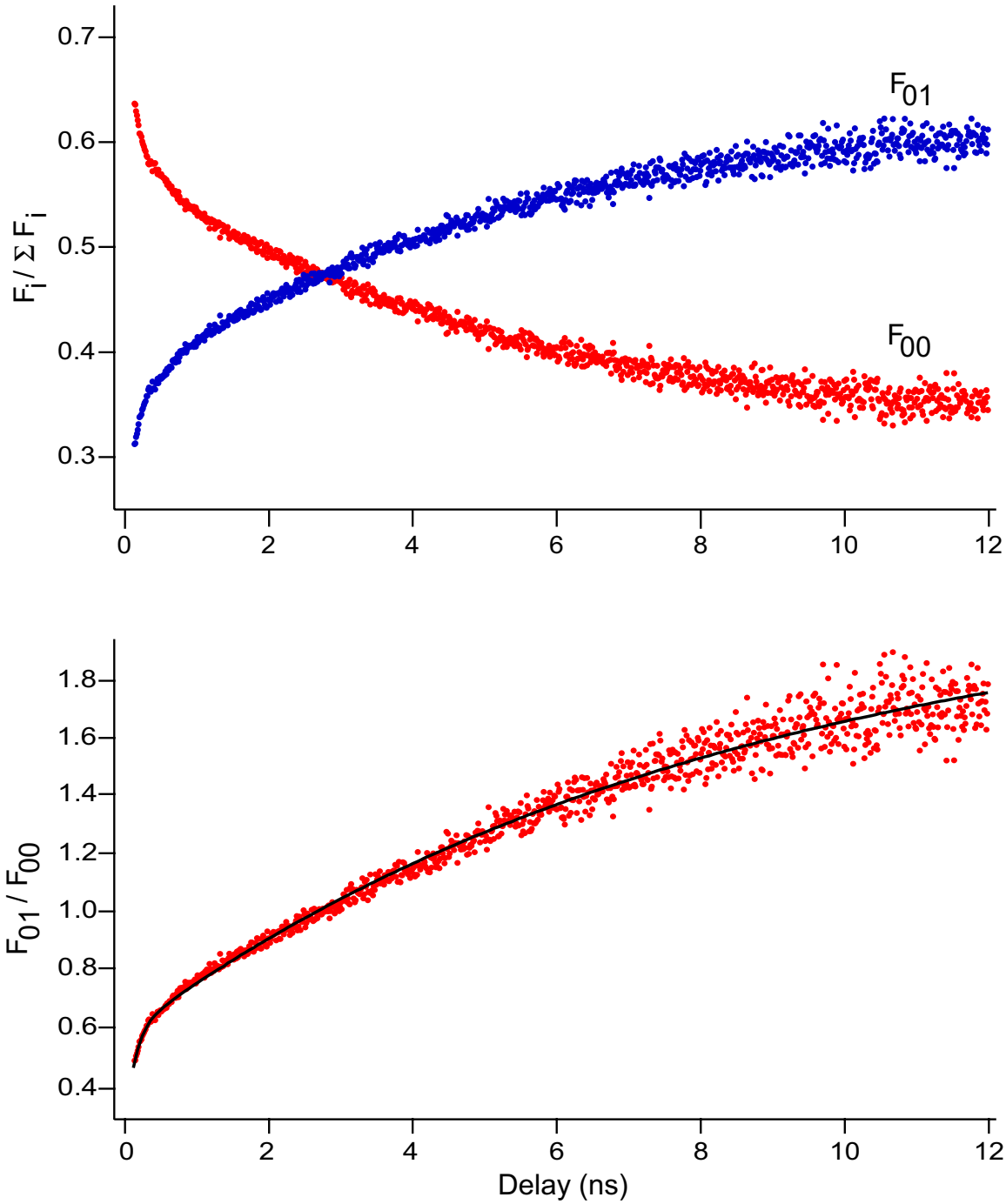

Figure 1.7. Time evolution of the dipole strengths for the 0-1 and 0-0 vibronic transitions obtained from time-resolved fluorescence spectra from ZnCytc in water (22 °C). Reprinted with permission from Lampa-Pastirk *et al*, 2004, American Chemical Society.[10] *Top:* Peak intensity normalized by total dipole strength. *Bottom:* Ratio of peak intensities.

As the solvent environment around the porphyrin is exposed to more aqueous solvent, it will exhibit an increase in polarity resulting in the initial red shift. In fbCytc, there are no metal-protein axial interactions as found in ZnCytc, so a relatively lower barrier height is expected. The absence of metal at the center of the porphyrin in fbCytc leads to an unstable molecule.[25] Similarly, the six-coordinate interaction with zinc is strained relative to native ferric cytochrome *c* (FeCytc), and therefore less stable than the native protein. The strained interaction in ZnCytc results in an early dissociation of Met80, on a time scale of about 100 ps.[10] The ratio of F_{0-1} to F_{0-0} is a measure of axial ligand coordination. Earlier work showed that the intensity of the F_{0-0} and F_{0-1} peaks change with respect to time (see Figure 1.7).[10] The rapid change in F_{0-1} / F_{0-0} occurs when there is a dramatic increase in His18 dissociation. The dissociation rate is limited by nonpolar reorganization of solvent molecules. The second structural transition is a blue shift, which accompanies a decrease in polarity surrounding the porphyrin. Blue shifts are generally associated with transitions from native states to molten-globule or acid-denatured states. This transition is comparable to thermal unfolding. As this reorganization occurs, different ligands may bind axially to the porphyrin. The third structural transition is another red shift, which again indicates an increased exposure of the porphyrin to the polar solvent. The third transition is likely to be a ligand-exchange in ZnCytc.[25]

The detection of a sequence of activation barriers demonstrates steps along an unfolding pathway.[25] The results were inconsistent with a Maxwell-Boltzmann distribution, which would predict a distribution over all states on the

protein-folding potential energy surface.[5] Instead, partially unfolded states appear in a sequential manner and eventually refold.[25]

1.2.4 Relevance to Dynamics in LH and RC Proteins in Photosynthesis

While the previous discussion of protein dynamics, folding, and vibrational energy dissipation is relevant to proteins in general, it is also particularly relevant to proteins involved in photosynthesis where energy absorbed by chlorophyll molecules is stored in terms of charge-transfer reactions across membranes. In the work described here, ZnCytc is treated as a model for a one-chlorophyll-binding protein and shares a mode of binding to the chromophores in the photosynthetic reaction center (RC).

It allows insight into light harvesting and how excess light energy may be dissipated from the chromophore to the surroundings.

Photosynthetic organisms use light-harvesting proteins[26] that contain chlorophyll and carotenoid chromophores to convert solar energy to chemical energy.[27] Each kind of chromophore is able to collect energy in a specific range of wavelengths by absorbing a photon that initiates a π to π* transition. The excitation energy is eventually transferred to a photosynthetic reaction center (RC)[28,29] where it drives electron-transfer reactions and generates a transmembrane redox potential gradient.[27] The potential gradient drives phosphorylation of adenosine diphosphate to yield adenosine triphosphate.[30]

Over the last four decades, X-ray crystal structures have been determined for many photosynthetic light-harvesting and reaction center proteins giving an

accurate picture of the location and relative arrangement of the chromophores.[31-39] An important example of a light harvesting protein is LHCII, the major light-harvesting complex associated with photosystem II in higher plants. LHCII consists of a trimeric assembly of protein subunits with C_3-symmetry. Each subunit contains its own chromophores, including chlorophylls (8 Chl *a* and 6 Chl *b*) and carotenoids (Lut 1, Lut 2, Neo, and Vio with Lut:Neo:Vio=2:1:0.5).[40,41] The arrangement of the chromophores optimizes energy transfer from chlorophyll *b* (Chl *b*) to chlorophyll *a* (Chl a).[42] Chl *a* molecules act as the terminal emitters that mediate energy transfer to the reaction center.[43] Energy transfer between the chromophores found in light harvesting proteins can proceed by one of two mechanisms. Excitation delocalization is a process that allows coherent energy transfer and involves strong coupling between molecules that are have small spatial separation and aligned dipole moments.[42] Förster resonance energy transfer (FRET) occurs when there is weak coupling between the transition dipole moments of two chromophores.[44] Carotenoids function as accessory light harvesting chromophores that allow absorption of wavelengths that cannot be absorbed by chlorophyll molecules[41] and also provide protection against photodamage by trapping triplet excited states.[45] LHCII arranges the chromophores to collect solar energy of many wavelengths and optimize energy transfer to the RC.[29,46] The arrangement of chromophores within LHCII avoids non-radiative quenching of excitation, though it is unclear how this is accomplished. Under high-light conditions when excess excitation cannot be transferred to the reaction center and could cause cellular damage, the system initiates non-photochemical quenching (NPQ) which

harmlessly dissipates excess excitation energy. NPQ could be mediated by small changes in protein conformation that change the distances and orientations of the chromophores in relation to one another.[47]

In addition to optimizing light harvesting and energy transfer, LHCII may serve as a dynamic solvent medium for the chromophores rather than a rigid scaffold. Protein dynamics may play an important role in reorganizing chromophores. The Beck group is interested in understanding how motion of a protein structure responds to the formation and decay of excited states resulting in an optimization of energy transfer or energy storage.[9,48] The main focus of recent studies has been on dynamic solvation, which is defined as the reorganization of solvent molecules in response to a change in electronic state or charge state of a solute chromophore.[49] In the case of chromoproteins, it describes the impact of conformational changes and structural fluctuations of a surrounding protein on intrinsic chromophores and their energy levels.[9,20,25,48] For intrinsic chromophores, the protein and associated liquid solvent molecules act together as the solvent.[48] When a solute such as a chlorophyll molecule absorbs visible light, a π to π^* transition occurs which changes the dipole moment of the chromophore. A change in the dipole moment is likely to affect the protein structure as the protein and surrounding solvent shift to the minimum of the new potential energy surface and relax into a new equilibrium state.[10,50] These changes are expected to occur for all excited solute/solvent pairs including those where a protein acts as the solvent. LHCII is only one example of a protein that may rearrange in response to chromophore excitation.[51] To avoid complications in data analysis for many chromophore systems, it is desirable to

study protein dynamics in a simple system that will give a more basic understanding of the chromophore/protein interactions upon excitation.

The Beck Lab has studied the model-system Zn^{II}-substituted cytochrome *c* (ZnCytc) in the past. ZnCytc is a good model system because it contains a single fluorescent intrinsic chromophore. This avoids the complications of a many-chromophore system. The main questions addressed in the ZnCytc work pertain to the timescales and character of the protein and solvent motion that occur in response to the formation of the Zn^{II} porphyrin excited state.[9,20] When an intrinsic chromophore within a protein is excited, it introduces perturbations to the surrounding protein. Those perturbations are thought to disturb the native fold of the protein as energy is dissipated and ultimately transferred to surrounding water molecules.[9,20,48] Since these motions may include structural transitions from the native structure to partially unfolded structures, the results may also contribute to understanding how cytochrome *c* unfolds and refolds.[9,20,25] Current understanding of protein folding can be described by a series of conformational changes along a funnel-shaped potential energy surface. The funnel-shaped potential energy surface leads to the lowest-energy state, known as the native state.[3] The native state of a protein is the arrangement of the primary structure into secondary and tertiary structures, primarily driven by hydrophobic and hydrophilic interactions of the amino acid side chains.[52,53] Along the potential energy surface, there are a series of activation-energy barriers.[1,24,52] As a protein folds, it moves from local minimum to local minimum by climbing over activation-energy barriers that are thermally accessible.[53,54] As a protein is unfolded from the native state, it would be expected

to follow a reverse set of trajectories. Instead, the results suggest that the protein transitions into a discrete set of conformations rather than randomly sampling the protein-folding funnel.[9,25] Understanding the response of a protein to excitation of a chromophore could result in a more accurate picture of the ways photosynthetic proteins are able to efficiently transfer energy in some circumstances and divert energy away from the reaction center in others. The way a protein dissipates vibrational energy as the excitation is transferred between chromophores toward the reaction center may play a central role in its function.

CHAPTER 2

Light-driven Partial Unfolding of Zn^{II}-substituted Cytochrome *c*

Summary

The nature of the partially unfolded structures that are generated in Zn^{II}-substituted cytochrome *c* (ZnCytc) upon optical excitation above the vibronic origin of the Q ($S_0 \rightarrow S_1$, $\pi \rightarrow \pi^*$ transition) band was investigated using continuous-wave fluorescence spectroscopy. The excess vibrational energy prepared in the S_1 state is transferred by intramolecular vibrational redistribution on the <2 ps timescale to the protein surroundings. This excitation of the protein results in structural transitions that change the environment of the Zn^{II} porphyrin and shift the fluorescence spectrum. Step-like transitions of the fluorescence spectrum's Stokes shift correspond to the activation threshold for changes in structure from the native state to a partially unfolded state associated with the Ω loop formed by residues 20–35, which is adjacent to the Cys14 and Cys17 thioether linkages from the porphyrin to the polypeptide backbone. This structural assignment is based on studies of the excitation-wavelength dependence of the fluorescence Stokes shift as a function of temperature and/or the presence of guanidinium ions (Gdm^+), either of which allows a distinction between the responses of the native and globally unfolded states. The excitation energy for optical formation of the unfolded state is consistent with the previous

determination by Englander and coworkers using hydrogen-exchange NMR spectroscopy in ferricytochrome *c* in the presence of Gdm^+.

2.1 Introduction

The energy landscape/protein-folding funnel hypothesis suggests that a partially unfolded structure can descend to the native state along a range of distinct trajectories rather than a discrete pathway of intermediate states.[1-4,24,52,55,56] Beck and coworkers suggested that this picture could be tested by following the propagation of partially unfolded structures after *optical* excitation from the native state.[48] In Zn^{II}-substituted cytochrome *c* (ZnCytc), it was demonstrated that at least three partially unfolded structures were obtained after excitation of the intrinsic Zn^{II} porphyrin (see Figure 2.1) well above the S_1 (Q band) 0–0 transition (Figure 2.2); the excess vibrational energy provides the activation energy for unfolding reactions from the native state.[25] This approach was termed *intramolecular vibrational excitation* (IVE). By scanning the wavelength of the light source, the vibrational excitation provided to the protein by radiationless decay and intramolecular vibrational redistribution (IVR) could be continuously tuned. After the vibrational energy transfer process is completed, the fluorescence emission of the vibrationally cooled S_1-state Zn^{II} porphyrin could then be used as a probe of the protein-refolding process.

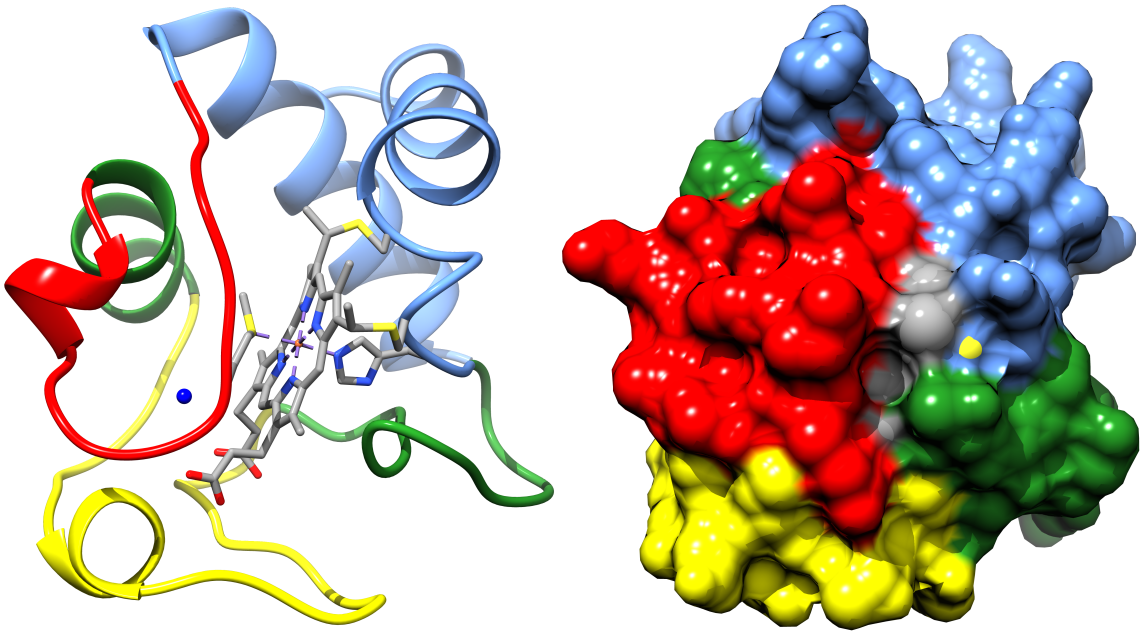

Figure 2.1. Ribbon (left) and solvent-excluded surface (right) renderings of the X-ray crystal structure of horse-heart ferricytochrome *c* (1hrc.pdb).[11] The porphyrin and associated structures (axial ligands: His18 and Met80 and thioether linkages: Cys14 and Cys17) are shown as stick structures in the ribbon picture. The protein structure is color coded from red to blue in order of relative folding stability following the scheme of Englander and coworkers:[57] residues 70–85 (red), residues 36–61 (yellow), residues 20–35 and the α helix over residues 60–70 (green), and the N- and C-terminal α helices (blue). Based on a comparison of 2D NMR spectra, ZnCytc is isostructural with the native, Fe^{II}-containing protein in solution.[58,59]

The nature of the partially unfolded structures produced in ZnCytc by the IVE process was left indeterminate.[25] The fluorescence spectrum from the Zn^{II} porphyrin exhibits step transitions of the integrated Stokes shift and vibronic structure when the excitation is tuned above the threshold that generates an unfolded state. The integrated Stokes shift provides information on changes in the protein and solvent structure that surrounds the Zn^{II} porphyrin, whereas the vibronic structure provides information on the presence or absence of protein or solvent-derived axial ligands to the Zn^{II} ion. Because the fluorescence lifetime in ZnCytc is ~4 ns, the changes in structure that are detected in terms of the Stokes

shift and vibronic structure of the fluorescence spectrum are likely to be short ranged in character, but it is not clear from the previous work whether local or global structural rearrangements are involved. Because the excitation wavelengths that yield unfolded structures are near to the onset of the Soret ($S_0 \rightarrow S_n$) absorption band, however, there is additionally the question of whether photochemical processes involving the axial ligands of the Zn^{II} porphyrin[48] are precursors to the unfolding reaction.

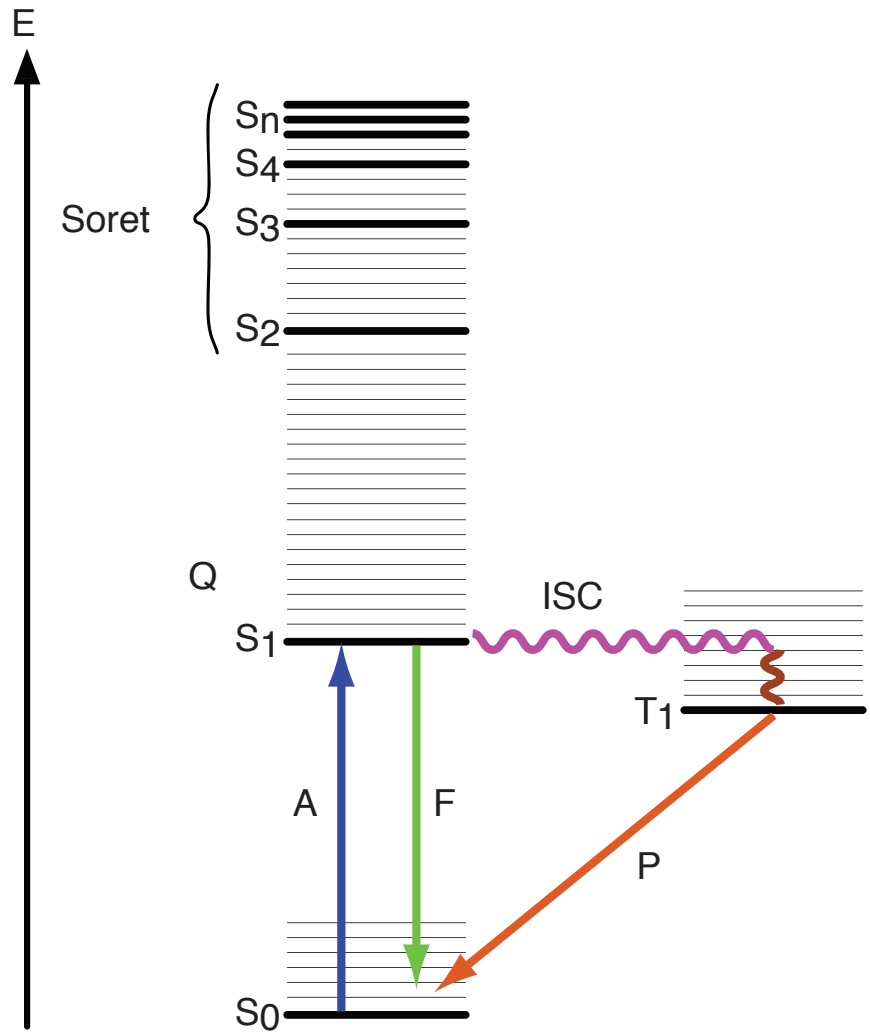

Figure 2.2. Jablonski energy-level diagram describing photophysical processes in ZnCytc. Vibronic energy levels are represented by horizontal lines. Absorption of a photon is represented by the vertical blue arrow. Nonradiative relaxation (NR) and intersystem crossing (ISC) are indicated by wavy arrows. Ground-state recovery via fluorescence (F) and phosphorescence (P) is indicated by the green and red arrows, respectively; additional nonradiative recovery processes to the ground state are not shown.

In this chapter, these questions are addressed by new experiments in which the IVE response sensed by the fluorescence spectrum of ZnCytc is characterized as a function of temperature and in the presence of guanidinium ions (Gdm^+). If the structural changes in ZnCytc are driven by vibrational excitations, an increase in the

temperature of the medium surrounding the protein would be expected to result in a lowering of the activation threshold for an unfolding reaction. The optical energy required to drive the native state to the unfolded state would be decreased as the temperature increases because the vibrational energy arising from the Maxwell-Boltzmann distribution would be added to the vibrational energy obtained by IVR from the absorbed photon. If the IVE response involves just the local environment of the Zn^{II} porphyrin, it would be completely transformed by denaturing the protein at high temperatures or in the presence of Gdm^{+}.

The results strongly suggest that the unfolding reactions driven by IVE in ZnCytc involve changes in conformation of the local polypeptide region adjacent to the thioether linkages to the Zn^{II} porphyrin. This conclusion is supported by the observation that the denatured protein exhibits an even larger IVE-induced response than the native protein and by a determination of the heat capacity of the affected protein region. The likely origin of the IVE response is shown to be a conformational change in the omega loop identified by the hydrogen-exchange NMR experiment by Englander and coworkers[57] as the highest energy protein folding unit (foldon) along the cytochrome *c* unfolding pathway.

2.2 Experimental Section

2.2.1 Sample Preparation. ZnCytc was prepared from horse-heart ferricytochrome *c* (Sigma) using the procedure described by Vanderkooi.[50] Liquid anhydrous hydrogen fluoride (Linde) was used as the demetalating agent. The reaction was run on a home-built gas-handling system in Teflon reaction vessels.

The metal-free or free-base protein (fbCytc) was isolated using strong cation ion-exchange chromatography on a Whatman CM-52 column. Reconstitution with Zn^{II} was performed at 50 °C in the presence of a 10-fold molar excess of zinc acetate (Sigma 379786-5G, 99.999%). Completion of the demetallation and metal-reconstitution reactions were determined spectrophotometrically by observing differences in the number and position of bands in the Q band region of the absorption spectrum.

The ZnCytc product solution was further prepared using methods described by Winkler and coworkers[60] and by Kostić and coworkers.[61] The protein solution was desalted and the protein was isolated by cation-exchange chromatography on a clean Whatman CM-52 column. Fractions containing ZnCytc were equilibrated with 25 mM sodium phosphate buffer at pH 7.0 by repeated concentration over an Amicon YM-10 ultrafiltration membrane (Millipore) and subsequent dilution with the buffer solution. The final product was concentrated, aliquoted, flash-frozen, and stored at –80 °C prior to use.

For use in fluorescence experiments, ZnCytc samples were thawed and diluted in 25mM pH 7.0 sodium phosphate buffer solution to obtain an absorbance of 0.15–0.17 for the Q band maximum. For Gdm^+ experiments, the dilution solution was prepared to contain the desired concentration of Gdm^+ and 25 mM sodium phosphate buffer at pH 7.0 when a sample was diluted to 3.0 mL. The absorption spectrum was recorded after dilution of each sample in a 1 cm quartz cuvette using an Ocean Optics USB2000 spectrometer (2 nm bandpass) and a Mikrotechnic DH-2000 fiber-optic light source.

2.2.2 Continuous-wave Absorption and Fluorescence Spectroscopy.

Absorption spectra were acquired with a Hitachi U-4001 spectrophotometer (2 nm bandpass). Fluorescence spectra were obtained using a home-built fluorescence spectrometer consisting of a Jobin-Yvon AH10 100 W tungsten-halogen light source, a Jobin-Yvon H10 excitation monochromator (4 nm bandpass), an Acton Research SP-150 emission spectrograph (2 nm bandpass), and a Jobin-Yvon Symphony CCD detector. The CCD detector employs a liquid nitrogen cooled, back-illuminated, 2000 × 800 pixel silicon detector chip (EEV corporation). A 300 groove/mm diffraction grating (500 nm blaze wavelength) was mounted in the emission spectrograph, resulting in a 270 nm spectral range imaged over 2000 vertically binned channels on the CCD detector chip. As presented as a function of wavenumber, the fluorescence intensities are multiplied by the square of the wavelength in order to compensate for the fixed (in wavelength units) spectral bandpass of the emission spectrograph. The absorption and fluorescence instruments are controlled by LabVIEW (National Instruments) programs.

For IVE experiments, the temperature of the sample cuvette was maintained by a Quantum Northwest TLC50F Peltier effect temperature controller at temperatures ranging from 5 °C to 90 °C. The wavelength of the excitation light source was calibrated over the entire scan range for an IVE experiment and daily at the 584 nm wavelength of the 0–0 peak of the ZnCytc absorption spectrum by measuring the spectrum at the sample position with an Ocean Optics USB2000 spectrometer. The Ocean Optics spectrometer was calibrated using a mercury emission spectrum. The spatially integrated power of the excitation beam, as estimated using a Coherent

Fieldmaster power meter and associated silicon photodiode detector, was 10 μW at 522.9 nm. Fluorescence emission spectra were acquired as the average of typically twenty 60-second exposures of the CCD detector.

2.3 Results

2.3.1 Dependence of Fluorescence Spectra on Vibrational Excitations. As reported in previous work, the fluorescence spectrum from ZnCytc shifts as the excitation light source is tuned above the wavenumber of the 0–0 vibronic transition owing to structural transitions of the surrounding protein. At low excitation wavenumbers, the fluorescence spectrum shown in Figure 2.3 is observed; the intensity of the spectrum scales with the relative absorption as the excitation wavenumber is scanned, but the shape and the position of the spectrum are unchanged. The excitation wavenumber chosen for this spectrum, 19120 cm^{-1} (522.9 nm), is 2,000 cm^{-1} above that for the 0–0 vibronic transition, where the absorption and fluorescence spectra cross. The shift to the red of the 0–0 peak of the fluorescence spectrum from that of the absorption spectrum provides an estimate of 57 cm^{-1} for the solvation reorganization energy, λ,

$$\lambda = \left(\nu_{0\text{-}0,A} - \nu_{0\text{-}0,F}\right)/2 \qquad (2.1)$$

This shift corresponds to the time integral of the dynamic fluorescence Stokes shift, the time-dependent stabilization of the excited state that occurs following optical excitation of the Zn^{II} porphyrin arising from polar and nonpolar reorganizational motions of the surrounding protein and solvent.[9,10] In the absence of a net

vibrational excitation, the protein and solvent response is triggered only by the ground-to-excited state changes in permanent dipole moment and size of the Zn^{II} porphyrin.

At significantly higher net vibrational excitations, >4,000 cm^{-1}, the fluorescence Stokes shift and the vibronic structure of the fluorescence spectrum exhibit changes that arise from discrete transitions of the protein structure (see Figures 2.4 and 2.5). The absorption dipole strength is continuously non-zero at excitation wavelengths below 600 nm (see Figure 2.3), so the net vibrational excitation provided to the protein by IVR from the Zn^{II} porphyrin can be varied at least to 10,000 cm^{-1} by scanning the excitation light source. (At excitation wavelengths above 450 nm, a range of excited singlet states S_n, $n \geq 2$, are excited; nonradiative decay to the S_1 state occurs on the <50 fs timescale in Zn^{II} porphyrins.[62]) Analysis of the set of spectra shown in Figure 2.4 illustrate the changes that evidence transitions in protein structure. The fluorescence Stokes shift exhibits an oscillatory response; the entire fluorescence spectrum shifts first to the red, then to the blue, and finally back to the red as the excitation wavenumber is scanned over the 4,000–10,000 cm^{-1} range. The magnitudes of these red and blue shifts are less than the solvation reorganization energy, so they are small relative to the wavenumber range shown in the set of spectra in Figure 2.4, but a first-derivative peak-maximum determination[25] for the 0–0 peak over a larger set of spectra obtains the profile shown in Figure 2.5a. Representative derivative functions were shown in previous work by the Beck group.[25] Synchronous with these shifts is an oscillation in the relative intensities of the 0–0 and 0–1 fluorescence peaks (see Figure 2.4 and 2.5b).

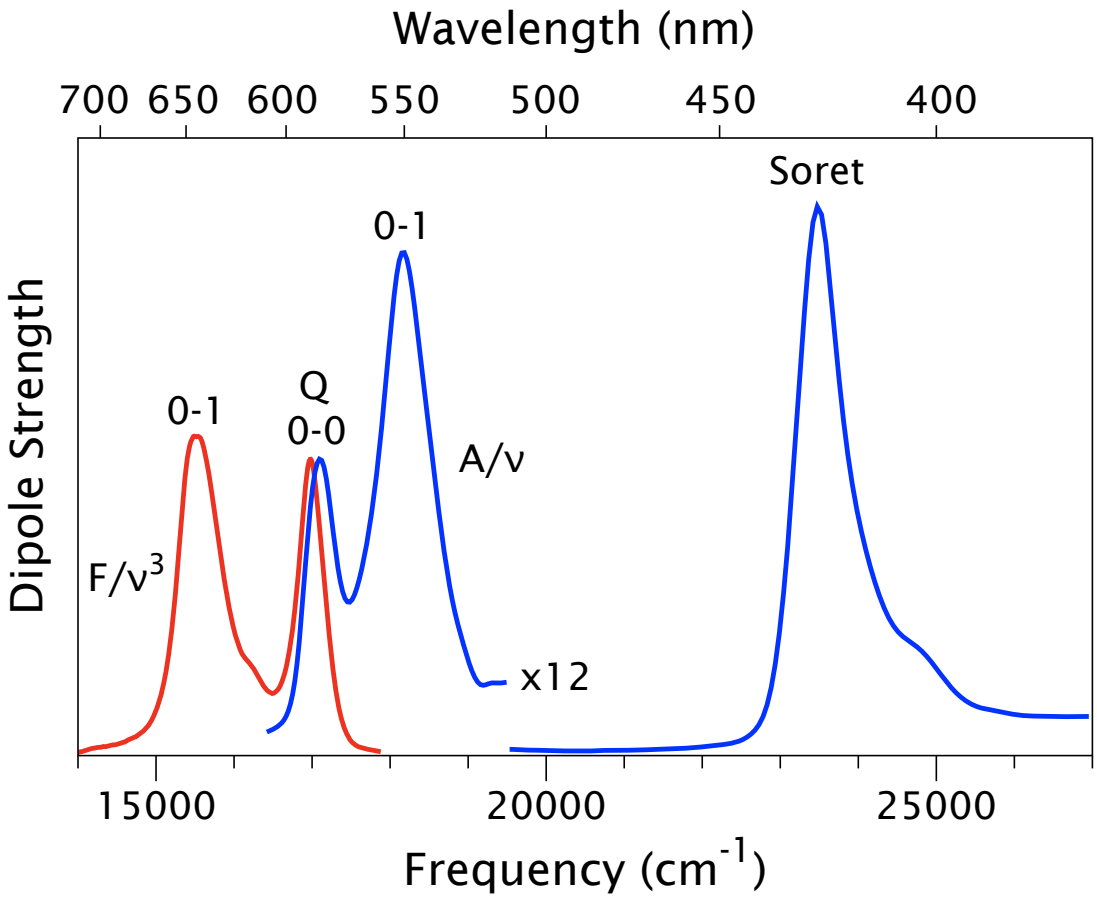

Figure 2.3. Continuous wave absorption (blue) and fluorescence (red) dipole-strength spectra from ZnCytc at 20 °C and pH 7.0, $A(\nu)/\nu$ and $F(\nu)/\nu^3$, respectively. The absorbance and fluorescence spectra were normalized to the amplitude of the 0–0 peak. The fluorescence spectrum was excited at 523 nm (19120 cm^{-1}). The $S_0 \rightarrow S_1$ vibronic transition is located where the two spectra cross, at 587.2 nm (17030 cm^{-1}).

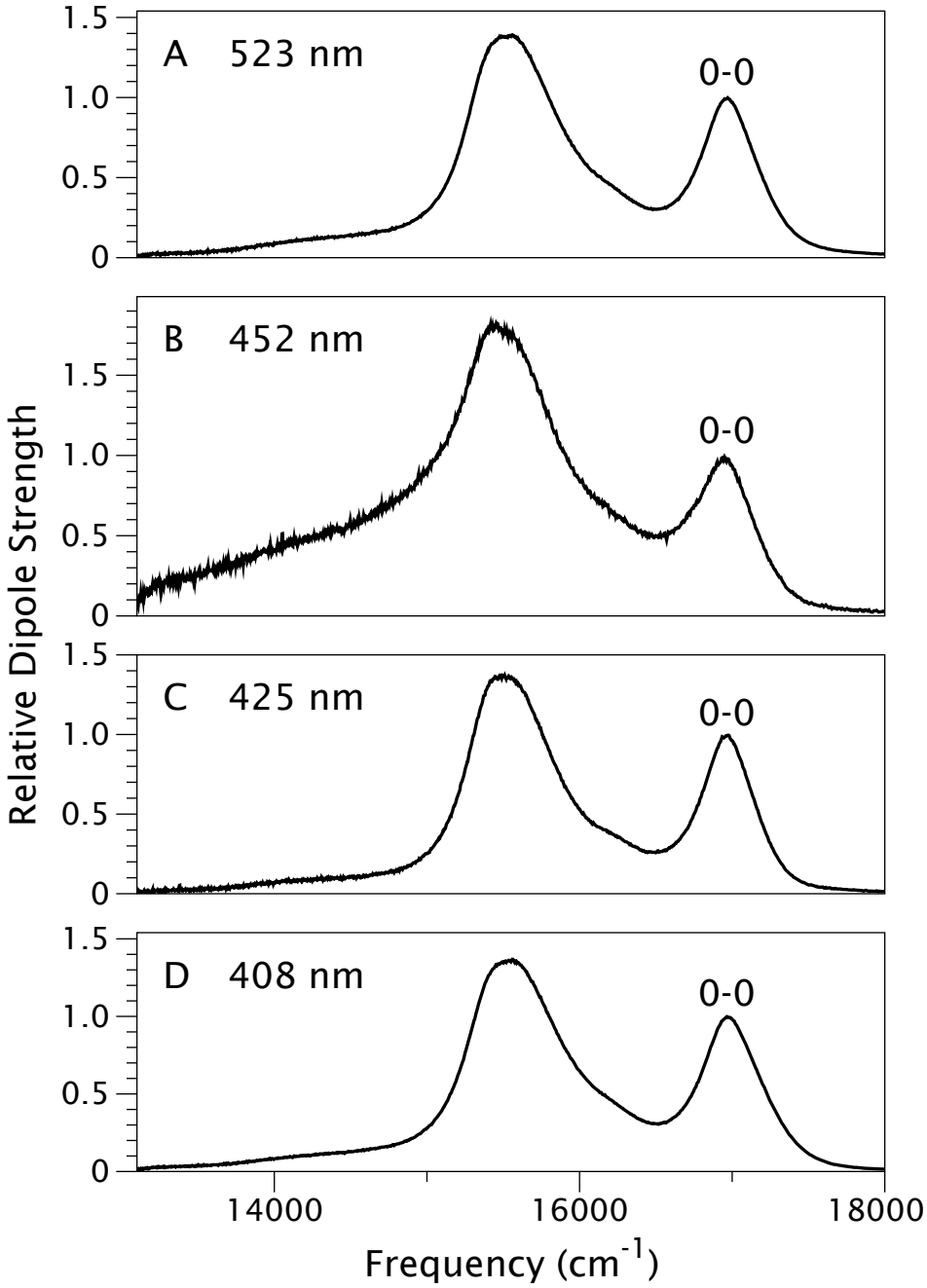

Figure 2.4. Fluorescence dipole-strength spectra from ZnCytc at 30 °C with excitation at (a) 523 nm ($\nu_{IVE} = 2000\,cm^{-1}$), (b) 452 nm ($\nu_{IVE} = 5000\,cm^{-1}$), (c) 425 nm ($\nu_{IVE} = 6350\,cm^{-1}$), and (d) 408 nm ($\nu_{IVE} = 7350\,cm^{-1}$). The same integration time was used in each; the spectra are plotted with normalization to the amplitude of the 0–0 peak. The spectrum shown in (a) is the same spectrum shown in Figure 2.3.

In the following narrative, we will call the dependence of the wavenumber of the peak maximum of the 0–0 peak in the ZnCytc fluorescence spectrum (as in Figure 2.5a) an *IVE profile*. The corresponding plot of the ratio of the intensities of the 0–1 and 0–0 peaks, $F_{0\text{-}1} / F_{0\text{-}0}$, will be called an *FR profile* (Figure 2.5b). Both profiles are expressed with respect to ν_{IVE}, the net vibrational excitation above the 0–0 transition,

$$\nu_{\mathrm{IVE}} = \nu_{\mathrm{ex}} - \nu_{0\text{-}0} \tag{2.2}$$

As shown in Figure 2.5, there are three step transitions observed in the FR and IVE profiles over the 4,000–10,000 cm^{-1} range. These transitions (I, II, and III) can be described by sigmoidal functions of the form

$$F\left(x\right) = y_0 + \frac{A}{2}\left(\left(\frac{\mathrm{erf}\left(x - x_0\right)}{\sqrt{2\sigma}}\right) + 1\right) \tag{2.3}$$

which are integrals of Gaussian distributions with width σ and center wavenumber x_0; the other parameters are introduced in the inset to Figure 2.5a. The first transition (I) accompanies a shift of the fluorescence spectrum to the red; transitions II and III are associated with blue shifts. A smoothing spline was used to describe nonparametrically the final region of the IVE profile (IV), which accompanies a shift of the fluorescence spectrum to the red, because the character of this part of the IVE and FR profiles varies with experimental conditions and is not well described by a single transition.

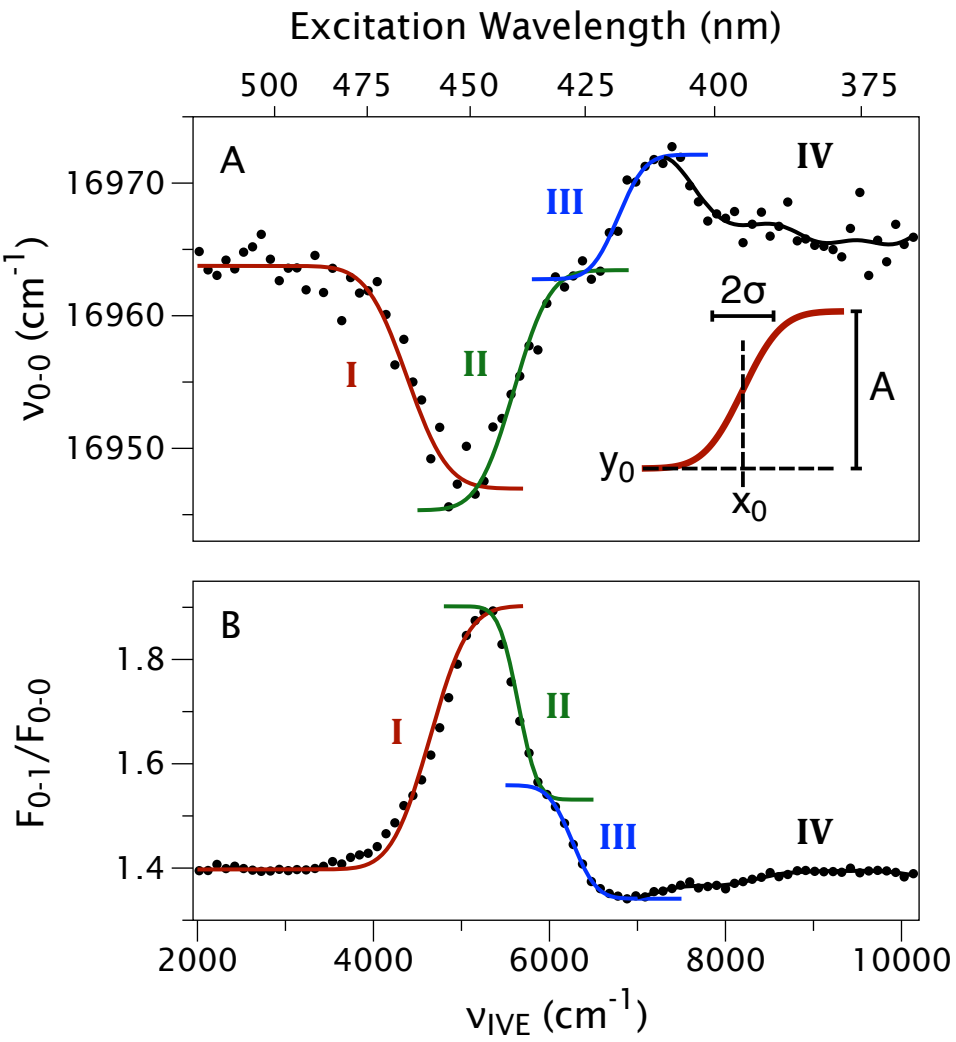

Figure 2.5. Evolution of the continuous-wave fluorescence spectrum from ZnCytc at 30 °C as a function of ν_{IVE}, the excitation energy above the wavenumber of the S_1 state vibronic origin: (a) wavenumber of the peak dipole strength in the 0–0 peak and (b) intensity ratio for the 0–1 and 0–0 peaks, $F_{0\text{-}1}/F_{0\text{-}0}$. The data is divided into four sections including transitions I, II, and III, which were superimposed with models described by Equation 2.3, and section IV, which has a smoothed curve drawn through the data. (*Inset*) Parameters for the sigmoidal functions (Equation 2.3) used to describe step transitions in the peak wavenumber and fluorescence ratio profiles: x_0, the center wavenumber of the transition; y_0, the value of the function prior to the transition; A, the amplitude of the transition; and σ, the width of the transition.

The structural nature of the shifts of the fluorescence spectrum of ZnCytc that accompany the transitions in the IVE profile is not clear just from a consideration of

the magnitudes of the shifts. The shifts to the red (transition I, 20 cm^{-1}) and blue (transitions II and III, 28 cm^{-1} total) are half as large as the solvent reorganization energy, so one might conclude that the transitions in the IVE response are associated with small reorganizations of protein and solvent around the Zn^{II} porphyrin. It should be noted, however, that the fluorescence spectrum shifts comparably to the blue when ZnCytc is denatured thermally or in the presence of Gdm^+; a shift of 20 cm^{-1} is observed as the temperature increases over the 70–90 °C range, and a shift of 52 cm^{-1} is observed in the presence of 4 M Gdm^+. Because the ground-to-excited-state change in permanent dipole moment and molecular size are small, the Zn^{II} porphyrin is a relatively insensitive probe of protein and structural dynamics. As shown below, however, we can use the temperature and Gdm^+ dependence of the IVE and FR profiles to structurally define the IVE transitions.

The FR profiles provide information on protein-limited rates of change of the Zn^{II} porphyrin's conformation following photodissociation of its axial ligands.[25] The relative dipole strength of the 0–0 and 0–1 peaks in the fluorescence spectra of Zn^{II} porphyrins reports changes in the conformation of the porphyrin that arise from binding of axial ligands.[63-66] Based on resonance Raman spectral evidence, Kostić and coworkers[61] conclude that the Zn^{II} porphyrin in ZnCytc assumes a five-coordinate configuration like that preferred by Zn^{II} porphyrins in solution[64,65,67,68], as opposed to the six-coordinate structure found in crystals of native ferricytochrome *c* (see Figure 2.1).[11] If correct, this assignment suggests that the methionine, Met80, does not make a significant interaction with the Zn^{II} ion. Owing to packing forces in molecular crystals, however, a number of strained

six-coordinate Zn^{II} porphyrins have been observed in X-ray diffraction studies.[69-71] Owing to the evidence from Zn^{II}/Fe^{II}-substituted cytochrome *c* co-crystals[72] and from 2D NMR spectroscopy[58,59] that ZnCytc assumes a structure that is isomorphous with that of FeCytc, it is known that the Met80 and His18 side chains attack the Zn^{II} ion in ZnCytc in ligand-binding configurations. We suggest at this point that the Zn^{II} porphyrin in ZnCytc adopts a strained six-coordinate structure with a weaker interaction with the Met80 side chain (2.30 Å from metal center) than with the His18 side chain (2.16 Å from metal center)[11]. Both of these axial ligands photodissociate in the S_1 state, yielding a time profile for the $F_{0\text{-}1}/F_{0\text{-}0}$ ratio that increases at rates that are associated with reorganization of the protein around the expanded cavity required by the Zn^{II} porphyrin.[10] Thus, as the $F_{0\text{-}1}/F_{0\text{-}0}$ ratio determined from the continuous-wave fluorescence spectrum rises (transition I), the *rate* of the protein response to release of the axial ligands increases compared to the fluorescence timescale. A decrease in the $F_{0\text{-}1}/F_{0\text{-}0}$ ratio (transitions II and III) indicates that ligands are rebinding to the Zn^{II} ion. This portion of the FR profile was previously assigned to rebinding of a different histidine side chain or a water molecule, accounting for a decrease in the $F_{0\text{-}1}/F_{0\text{-}0}$ ratio during transitions II and III in an FR profile.[20,25] It should be noted that the shape of the FR profile observed in the previous work is significantly different than that shown in Figure 2.5b; the $F_{0\text{-}1}/F_{0\text{-}0}$ ratio exhibits a much smaller increase in transition IV in the present work.

In the following, we report how the IVE and FR profiles depend on the sample temperature and Gdm^+ concentration in an effort to determine whether the step

transitions we observe correspond to local or global structural transitions and to determine their mechanism of formation. A key observation is that the denatured state exhibits IVE and FR profiles that are similar in shape to those observed in the native state but that the magnitude of the IVE shifts are much larger in the denatured state.

2.3.2 Temperature Dependence of the IVE and FR Profiles. Figure 2.6 compares the IVE profiles of ZnCytc solutions over the 5–90 °C temperature range. Each profile is represented in the figure by sigmoidal transitions (Equation 2.3) or a smoothing spline (for transition IV) fit to the measured values of the peak wavenumber of the 0–0 peak as a function of ν_{IVE}. The supporting materials include separate plots like Figure 2.5 for each temperature showing the measured data points and the fitted curves. As the temperature increases, the fluorescence spectrum observed with low ν_{IVE} shifts initially to the red over a 26 cm^{-1} range, but above 70 °C the spectrum shifts to the blue over a 18 cm^{-1} range. This reversal marks the thermal denaturation of the protein.[73] The shape of the IVE profiles observed above and below 70 °C are comparable, but the total range of the shift from red to blue over transitions I–III increases markedly in the denatured state.

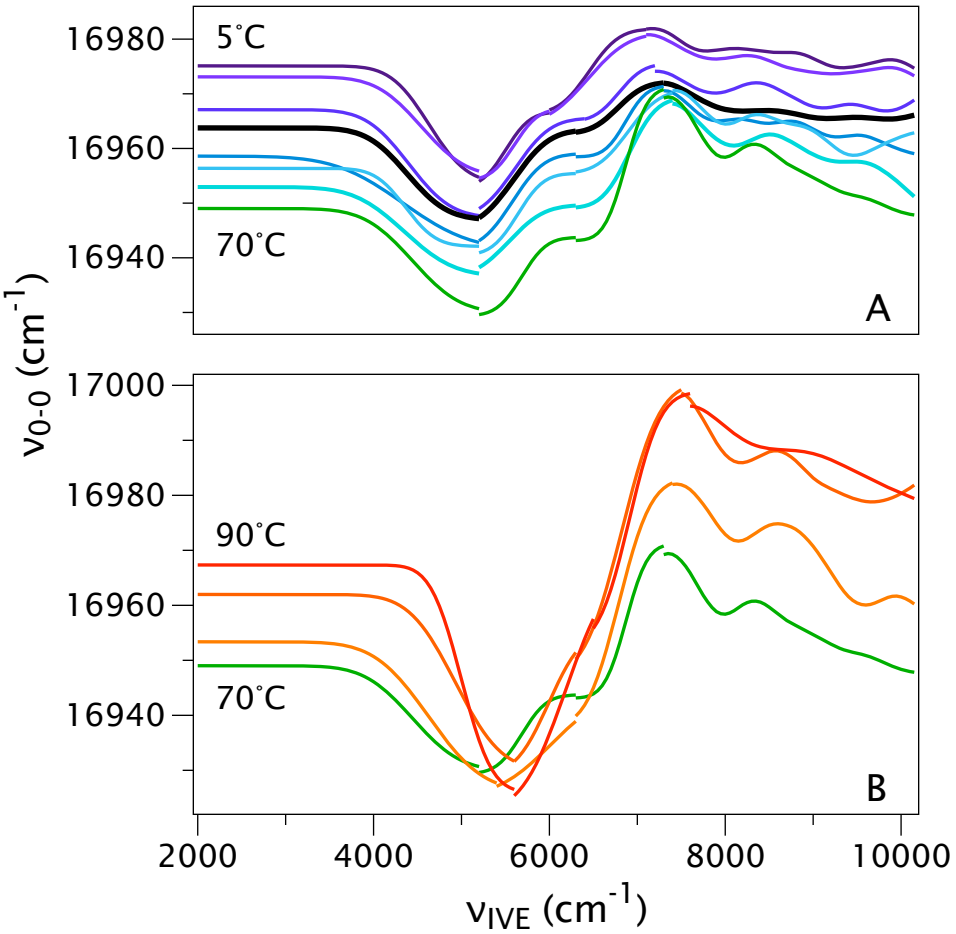

Figure 2.6. IVE profiles for ZnCytc as a function of temperature. Curves at each temperature were obtained by fitting the experimental peak wavenumbers (Equation 2.3). The integrated Stokes shift, as determined by the wavenumber of the 0–0 peak maximum, $\nu_{0\text{-}0}$. Peak maxima are plotted as points. The trendline includes a fit using Equation 2.3 to describe each of the first three apparent transitions in the data and a smoothed curve to describe the data after the peak. (a) The integrated Stokes shift at eight temperatures (5 °C, 10 °C, 20 °C, 30 °C, 40 °C, 50 °C, 60 °C, and 70 °C) demonstrating the change in the profile as temperature increases to the denaturation point of the protein. (b) The integrated Stokes shift at four temperatures (70 °C, 80 °C, 85 °C, and 90 °C), demonstrating the change in the profile as temperature increases above the denaturation point of the protein.

Figure 2.7 shows the corresponding FR profiles over the same range of sample temperatures. The midpoint of transition I does not vary significantly with temperature; the precision of the midpoint determinations here and in the IVE profiles is ±50 cm^{-1}. The same is true for transitions II and III below 70 °C, but at

higher temperatures a modest blue shift is observed. The average value of the $F_{0\text{-}1} / F_{0\text{-}0}$ ratio decreases as the temperature increases, but note that the amplitude of transitions I–III gets larger as the temperature increases. These results suggest that the reorganizational response to the photodissociation of the Zn^{II} porphyrin's axial ligands generally slows as the temperature increases but that the rate increases markedly over the ν_{IVE} range associated with transitions I–III. The latter observation reflects our conclusion that transitions I–III involve excited-state exchange of axial ligands;[25] transition I is associated with a release of ligands whereas transitions II and III are associated with rebinding of ligands.

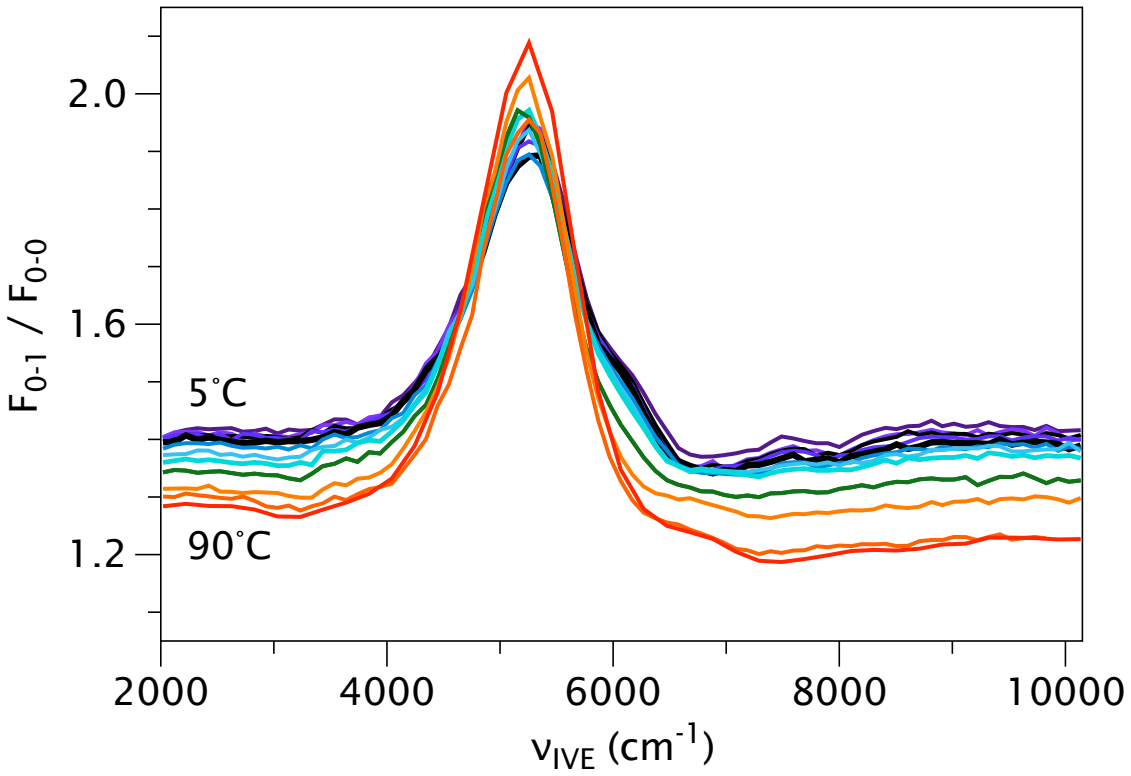

Figure 2.7. Dependence of the fluorescence peak ratio on intramolecular vibrational excitation at multiple temperatures. A line graph for each temperature shows the actual data points obtained after smoothing the fluorescence curve and using a peak-finding routine to identify the peak position and intensity.

Figure 2.8 compares the temperature dependences of the midpoints, $x_{0,i}$, of the transitions in the IVE and FR profiles. For transitions I and II (Figure 2.8a and 8b, respectively), the data points in the native and denatured states are described by separate linear trendlines. The intersection of the trendlines provides an estimate for the denaturation temperature, 65 °C. Transitions I and II exhibit a small initial red shift followed by a sharp blue shift once the protein denatures. Transition III (Figure 2.8c), in contrast, exhibits an initial blue shift and reaches a constant value above 30 °C. The midpoints of the FR profile transitions are essentially independent of temperature below the denaturation temperature.

The negative slopes of the plots shown in Figure 2.8 for the IVE profile midpoints for transitions I and II suggest an interpretation as heat capacities for the portion of the system that is undergoing a transformation during the IVE transitions:

$$-\frac{\mathrm{d}x_0}{\mathrm{d}T} \cong \frac{\mathrm{d}\varepsilon}{\mathrm{d}T} = C_v \qquad (2.4)$$

The rate of change of the midpoint of a transition, $x_{0,i}$, with respect to temperature, T, is equated to the rate of change of the average energy of the system, ε, which is formally equal to the heat capacity at constant volume.[74] This equation is suggested by the hypothesis[25] that the vibrational energy obtained via IVR of the excess excitation energy above the S_1 state provides the activation enthalpy required for a change in structure of the protein. As the sample temperature increases, the mean internal energy of the system increases according to the Maxwell-Boltzmann distribution, so the extra energy from the photon that is required to reach the

activation threshold for a protein structural transition should exhibit a weak negative temperature dependence. The behavior shown in Figures 2.8a and 2.8b for transitions I and II is generally consistent with this expectation. The magnitude of the slopes (3.4 cm^{-1} K^{-1}= 9.7 cal mol^{-1} K^{-1} and 1.5 cm^{-1} K^{-1}= 4.3 cal mol^{-1} K^{-1}) are very small compared to the overall heat capacity (4192 cal mol^{-1} K^{-1} .[75]) This finding raises the suggestion that the activation thresholds are not constant with respect to temperature, but it seems clear that the structural transitions are local to the protein region connected to the Zn^{II} porphyrin rather than involving the whole protein.

Above the thermal denaturation temperature, the IVE profile midpoints for transitions I and II exhibit positive slopes. These results suggest that the residual structure in the denatured state evolves with temperature. The comparable positive slope associated with transition III at low temperatures in Figure 2.8c reports that the affected region of the protein obtains a structure similar to that in the denatured state.

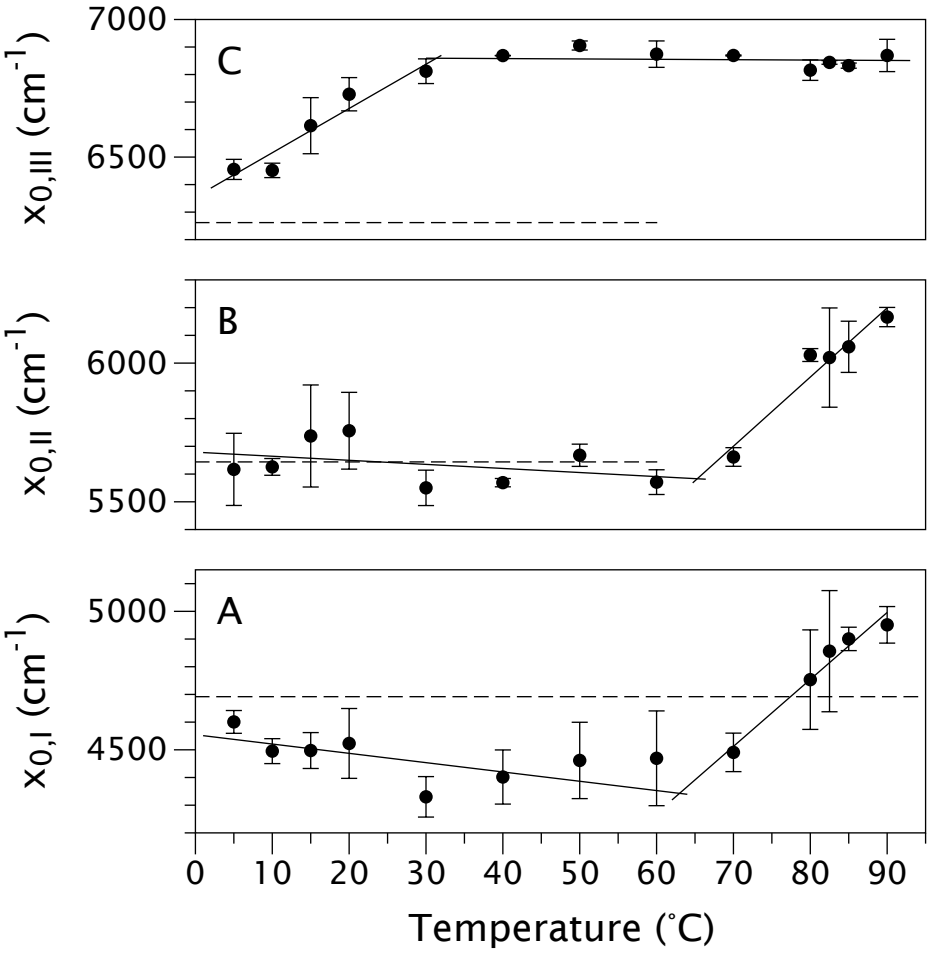

Figure 2.8. Temperature dependences of the midpoints, $x_{0,i}$, for the IVE and FR profiles from ZnCytc: (a) Transition I; (b) Transition II; (c) Transition III. For (a) and (b), the trendlines shown at low temperatures includes data points ranging from 5°C to 50°C; the trendlines shown at higher temperatures includes data points from 70°C to 90°C. For (c), the trendline shown at low temperatures includes data points ranging from 5°C to 30°C; the trendline at higher temperatures includes data points from 30°C to 90°C.

Figure 2.9 compares the temperature dependences of the amplitudes, A_i, of the transitions in the IVE and FR profiles. These plots report the change in the environment of the Zn^{II} porphyrin that accompanies the red and blue shifts of the fluorescence spectrum. Below the denaturation temperature, the red shift associated with transition I (Figure 2.9a) and the sum of the blue shifts associated with transitions II and III (Figure 2.9b) are essentially constant. Above the

denaturation temperature, the red and blue shifts increase significantly as the temperature increases. These results make it clear that the structural change associated with the IVE transitions is a change in the conformation of the part of the protein that packs around the Zn^{II} porphyrin in the native state and in the denatured state. Further, the affected portion of the protein makes a larger structural change when excited by IVE in the denatured state than in the native state.

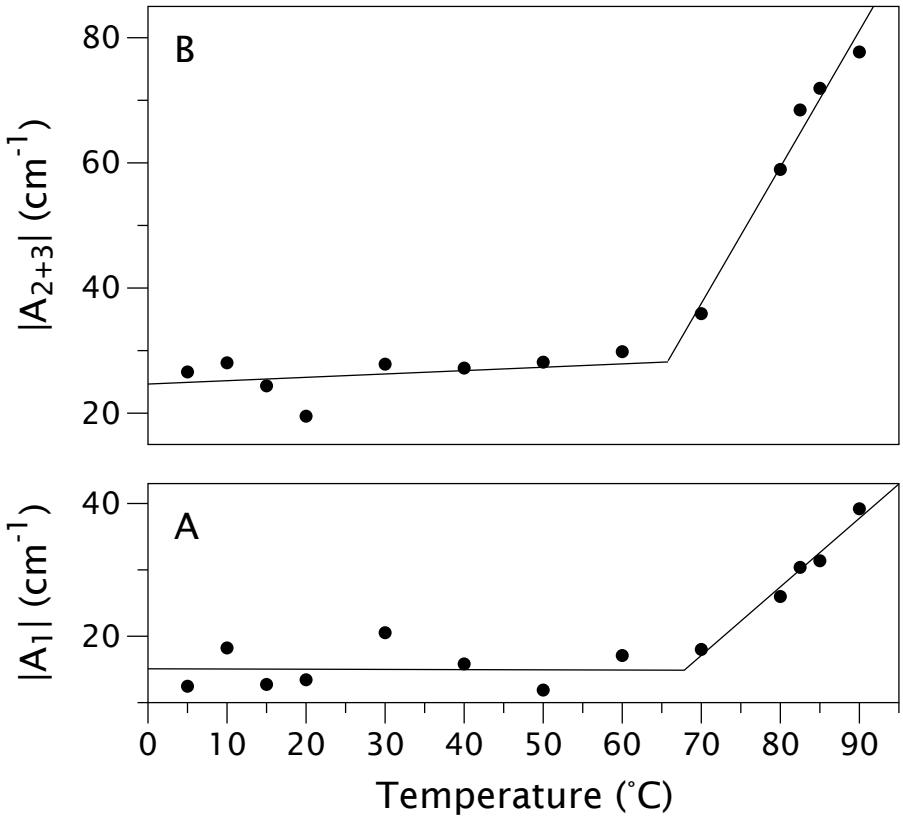

Figure 2.9. Absolute value of the amplitudes of the first red shift, A_1, and the blue shift, A_{2+3}, of the IVE profile as a function of temperature. For (a) and (b), the trendlines shown at low temperatures includes data points ranging from 5°C to 70°C (slope: 0.003 cm^{-1}/°C and 0.054 cm^{-1}/°C, respectively), below the protein's transition to a denatured state. The trendlines shown at higher temperatures includes data points from 70°C to 90°C (slope: 1.03 cm^{-1}/°C and 2.18 cm^{-1}/°C, respectively), after the protein is denatured.

2.3.3 Gdm^+ Dependence of the IVE Profile. Figure 2.10 shows the variation of the IVE profile of ZnCytc as Gdm^+ is added to the solution. Sigmoidal transitions (Equation 2.3) or a smoothing spline (for transition IV) represent the trends in each profile (see the supporting materials for the data points and fitted curves). At low ν_{IVE}, the fluorescence spectrum shifts to the blue according to a two-state denaturation transition with a midpoint at 1.75 M Gdm^+ ($\Delta G_{Fold} = -10.74$ kJ mol^{-1}, $m = 6.16$ kJ mol^{-1}; Jagnya Tripathy, manuscript in preparation). The IVE transitions substantially increase in amplitude as the denaturation transition occurs (1-3 M Gdm^+) just as observed for the thermal denaturation of the protein. Even at low Gdm^+ concentrations, however, the midpoints of the transitions progressively shift to higher ν_{IVE} as Gdm^+ is added.

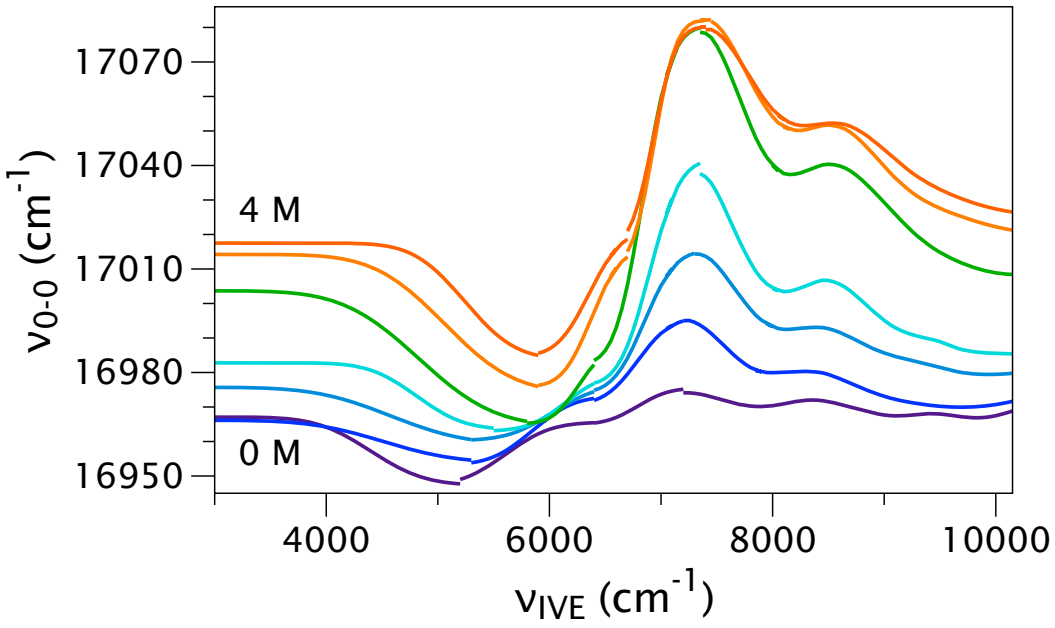

Figure 2.10. Dependence of the IVE profile of ZnCytc as a function of ν_{IVE} on Gdm^+ concentration. The integrated Stokes shift at seven concentrations of guanidinium ion (0.0 M, 1.0 M, 1.5 M, 2.0 M, 2.5 M, 3.0 M, and 4.0 M), demonstrating the change in the profile as denaturant concentration increases until the protein is fully denatured.

Figures 2.11 and 2.12 plot the Gdm^+ dependences of the midpoints, $x_{0,i}$, and amplitudes, A_i, of the IVE profile transitions. Unlike the temperature dependence (Figure 2.9), the midpoints of the IVE transitions (Figure 2.11) do not exhibit a clean break between the native and denatured states as Gdm^+ is added (estimated uncertainty in data points is approximately 100 cm^{-1}). Instead, the profiles exhibit roughly linear responses, indicating that the activation thresholds for the IVE transitions substantially increase as Gdm^+ binds to exterior sites on the part of the protein. In contrast, the amplitudes (Figure 2.12) show distinct regions for the native and denatured states as the Gdm^+ concentration is varied. The largest amplitudes for transition I (Figure 2.12a) and for the sum of the blue shifts in transition II and III (Figure 2.12b) are observed at the end of the unfolding transition (2.5 M). This behavior is comparable to that observed in the thermal denaturation of the protein; the change in the Zn^{II} porphyrin's environment that accompanies the IVE transitions is much larger in the denatured state. The region of the protein that is affected by the IVE transitions is apparently more constrained in the native state than in the denatured state. The decrease in the amplitudes shown in Figure 2.12 above the denaturation concentration may involve binding of Gdm^+ to regions of the protein that were protected in the native state.

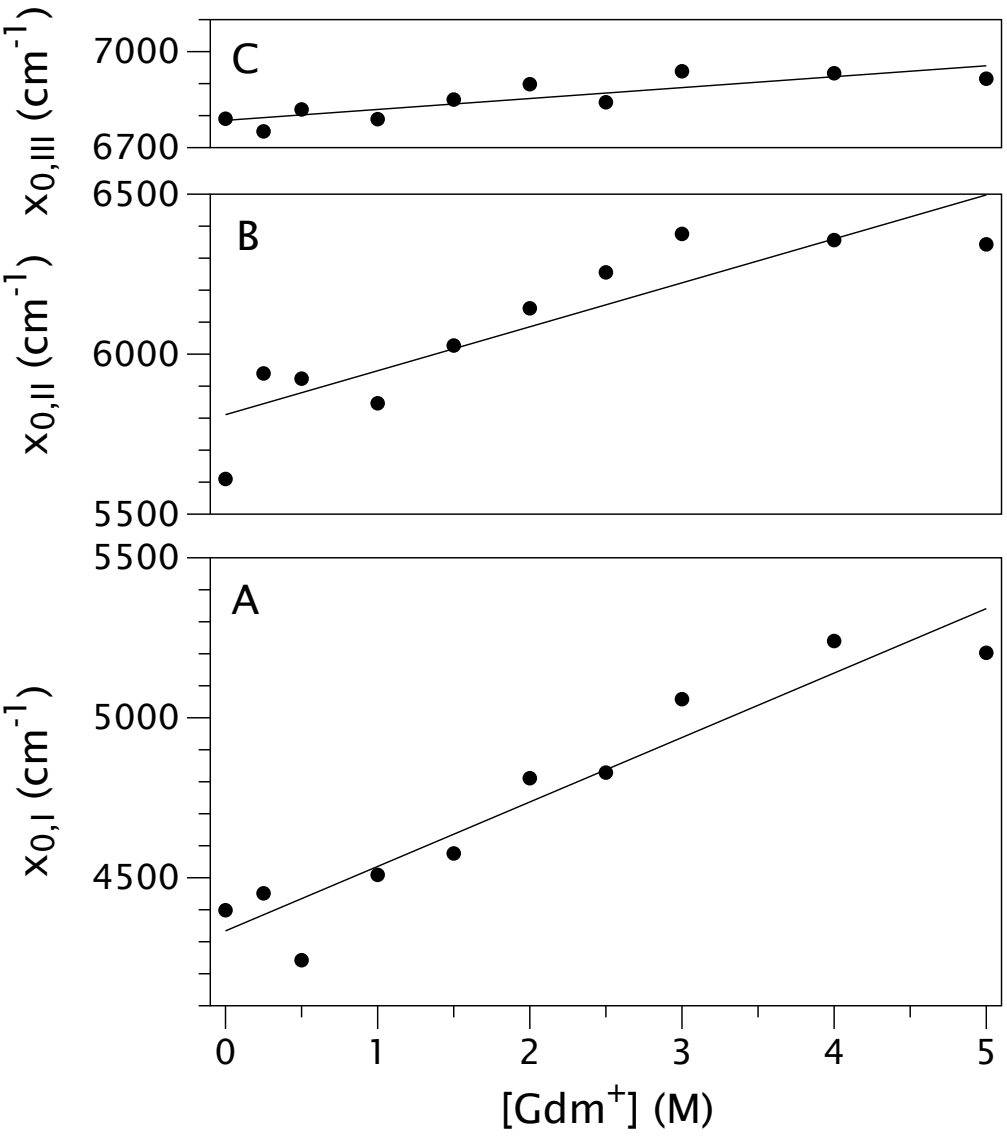

Figure 2.11. The excess excitation wavenumber midpoint, x_0, of each transition as a function of guanidinium concentration, (a) $x_{0,\mathrm{I}}$, (slope: 201 cm^{-1}/M) (b) $x_{0,\mathrm{II}}$, (slope: 137 cm^{-1}/M) (c) $x_{0,\mathrm{III}}$, (slope: 34 cm^{-1}/M).

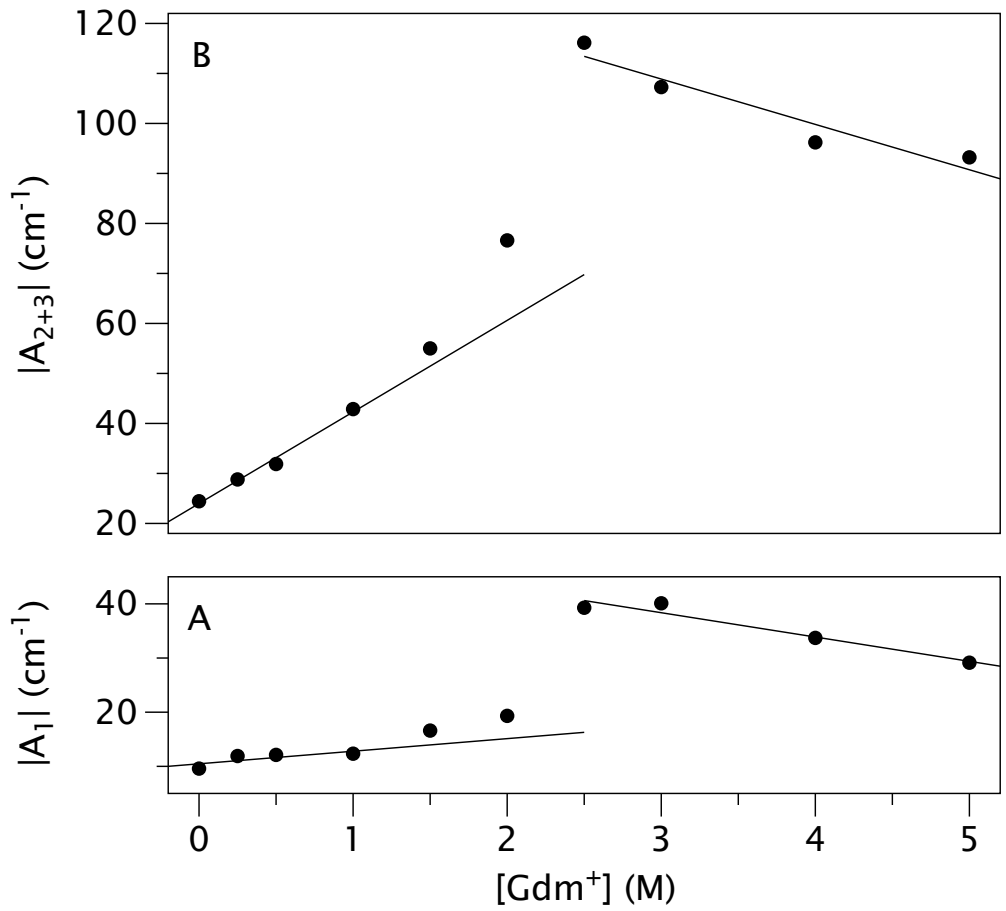

Figure 2.12. Absolute value of the amplitude of the red shift of the ZnCytc fluorescence spectrum in transition I, A_1, and the sum of the amplitudes for the blue shift, $A_2 + A_3$, in the IVE profile as a function of guanidinium ion concentration. For both (a) and (b), the trendlines shown at low Gdm^+ concentration include data points ranging from 0.0 M to 1.0 M (slope: 2.3 $cm^{-1}/°C$ and 18.3 $cm^{-1}/°C$, respectively), below the protein's transition to a denatured state. The trendlines shown at higher Gdm^+ concentration includes data points from 2.5 M to 5.0 M (slope: –4.5 $cm^{-1}/°C$ and –9.1 $cm^{-1}/°C$, respectively), after the protein is denatured.

2.4 Discussion

The experiments described in this paper provide an improved picture for the nature of the structural changes that accompany excitation of the intrinsic Zn^{II} porphyrin in ZnCytc above its 0–0 transition to the S_1 state. The main conclusion is that a small section of the protein undergoes a conformational change owing to

being excited by the excess vibrational energy it obtains via IVR from the Zn^{II} porphyrin. This conclusion is required because the IVE profile exhibits a characteristic red–blue–red shape in the native state and in the denatured states produced thermally or by addition of Gdm^+. The vibrational nature of the excitation is confirmed by the lowering of the activation threshold for transitions I and II as the temperature is raised. Further, the portion of the IVE profile associated with a blue shift of the fluorescence spectrum (transitions II and III) is the part of the profile that yields an unfolded character.

Because the IVE transitions are driven by IVR-mediated transfer of energy from the Zn^{II} porphyrin to the polypeptide backbone in ZnCytc, the regions of the protein that are involved in IVE-driven conformational changes are nearby to the Cys14 and Cys17 thioether linkages (see Figure 2.13). The wavenumber regions associated with transitions I–III span the wavelength region between the Q and Soret bands, which are formally porphyrin-centered $\pi \rightarrow \pi^*$ transitions. The most efficient channels for IVR from the porphyrin to the protein are through covalent bonds, through the thioether linkages of Cys14 and Cys17. These two cysteines are on one end of the amino-terminal blue region (residues 1 through 19), adjacent to the green loop (residues 20 through 35) in the Englander color scheme (see Figures 2.1 and 2.13).[57]

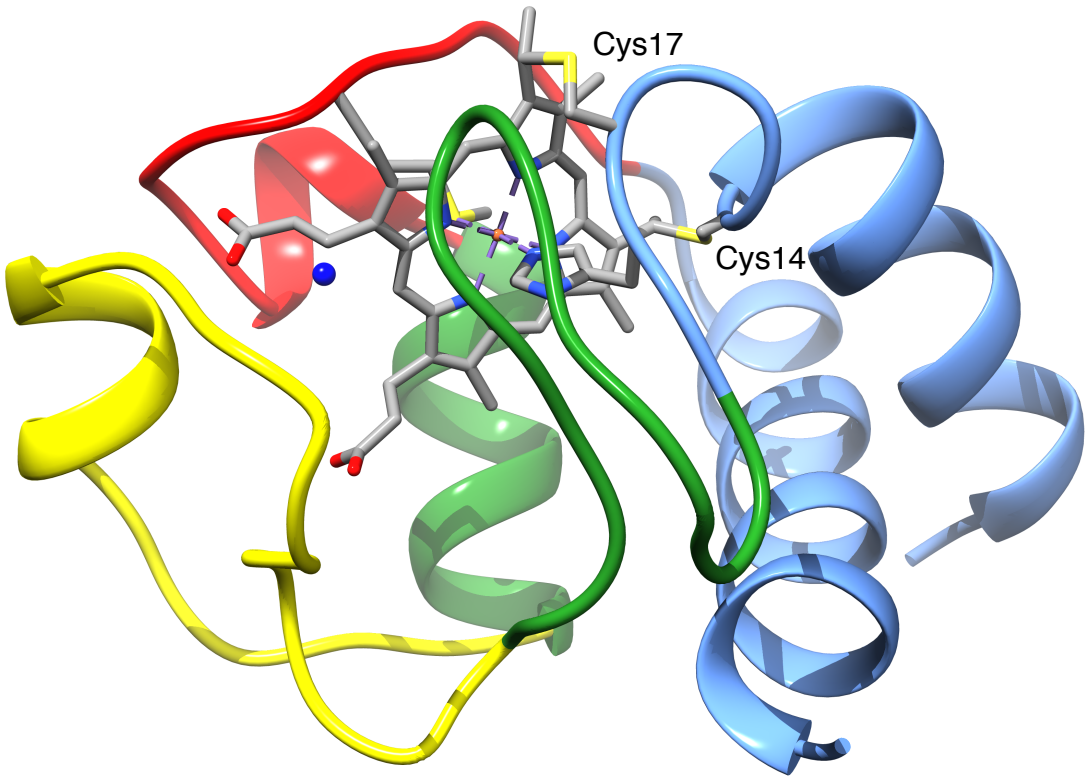

Figure 2.13. Another view of the X-ray crystal structure of horse-heart ferricytochrome *c* (1hrc.pdb)[11] following the scheme of Englander and coworkers.[57] The figure has been rotated when compared to Figure 2.1 to allow a view of the two thioether linkages, Cys14 and Cys17. Also note the blue dot representing an intrinsic water molecule adjacent to the porphyrin.

A reasonable assignment for the regions of the ZnCytc protein that undergo partial unfolding during transitions II and III can be obtained from a comparison of the activation thresholds determined from the IVE transitions and the Gibbs reaction energies for activation of the cooperative protein-folding groups identified by Englander and coworkers.[57] Equilibrium hydrogen-exchange NMR (HX-NMR) experiments with FeCytc in the presence of Gdm^+ determined the Gibbs energies of reaction for the opening of different parts of the protein so that exchange of protons with the surrounding aqueous solvent is accelerated. These cooperative units[57] or foldons[76-78] are shown in Figure 2.1; the two most stable regions of the protein are

associated with the regions colored blue and green (at 30 °C, $\Delta G = 53.6$ kJ/mol and 41.8 kJ/mol, respectively). The IVE experiment effectively results in a *vertical* excitation of the affected regions of the protein; the excitation occurs on a short timescale compared to protein and solvent motion, so the associated change in structure is instantaneously small ($\Delta S \approx 0$).[25] Thus, the ΔH associated with the IVE event at constant temperature can be approximately equated to a Gibbs energy of activation, $\Delta G^{\ddagger}$:

$$\Delta G^{\ddagger} = \Delta H^{\ddagger} - T\left(\Delta S^{\ddagger} \approx 0\right) \cong \Delta H^{\ddagger} \tag{2.5}$$

Using this relationship, the midpoint of transition I corresponds to $\Delta G^{\ddagger} = 51.8$ kJ/mol at 30 °C (see Figure 2.8, $x_{0,\mathrm{I}} = 4330\ \mathrm{cm}^{-1}$). This value is not greater than that reported by Englander and co-workers for the process that promotes exchange of protons in the blue region. The reaction profile for an endoergic ($\Delta G > 0$) change in structure would be expected to consist of a non-negligible excess Gibbs energy between the transition and product states that corresponds to $\Delta G^{\ddagger}$ for the reverse reaction. The difference in Gibbs energy between $\Delta G^{\ddagger}$ and ΔG is significant for the green loop, 10.0 kJ/mol, so it remains a candidate for assignment to transition I. Because transition I corresponds to a red shift of the fluorescence spectrum, however, it is assigned to a conformational change of the native state that is not unfolding in character, so it may be that the HX–NMR experiments would not detect it. In contrast, $\Delta G^{\ddagger}$ at 30 °C for transitions II and III are 66.4 kJ/mol ($x_{0,\mathrm{II}} = 5550\ \mathrm{cm}^{-1}$) and 81.5 kJ/mol ($x_{0,\mathrm{III}} = 6812\ \mathrm{cm}^{-1}$),

respectively. These activation energies are compatible with structural assignments for unfolding processes to the blue region or the green region that would be expected to result in deprotected regions of the protein and promote hydrogen exchange.

The thermodynamic analysis given above is supported by the structural criterion that the affected protein regions must be sequence-adjacent to the Cys14 and Cys17 thioether linkages in order to be efficiently excited by IVR. A second requirement is that the affected regions must be adjacent to the Zn^{II} porphyrin in the native structure so that shifts of the fluorescence spectrum might be expected when an IVE transition occurs. These requirements favor assignment of transitions II and III to the green loop. The green loop begins three amino acids after Cys17 and provides most of the native state environment to the His18-face of the Zn^{II} porphyrin, where the π electrons would sense changes in environment that shift the fluorescence spectrum. The blue region leading from Cys14 to the N-terminus is distant from the Zn^{II} porphyrin in the native fold. The short loop between Cys14 and Cys17 is unlikely to be flexible owing to its restriction by the thioether linkages to the porphyrin macrocycle, so conformational changes of that region are unlikely to contribute to the IVE transitions.

2.5 Conclusions

We have characterized the step transitions exhibited in the integrated fluorescence Stokes shift of ZnCytc that occur in IVE profiles, the dependence of the fluorescence Stokes shift on the excitation wavenumber above the 0–0 transition of

the S_1 state. These transitions evidence conformational (transition I) and partial unfolding (transitions II and III) reactions. A comparison of the activation thresholds for transitions II and III with the Gibbs energy of unfolding for the cooperative units detected by Englander and coworkers with HX–NMR spectroscopy suggests a structural assignment to the green omega loop adjacent to Cys17 in the amino-acid sequence. The through-bond flow of vibrational energy from the Zn^{II} porphyrin to the polypeptide backbone by IVR processes promotes the unfolding reactions in the IVE experiment.

These findings are significant because they support the idea that a range of partially unfolded structures are microscopically populated during spontaneous protein folding. The vertical excitation resulting from IVE provides the means to drive a protein from the native state to a range of partially unfolded states provided that an electronic chromophore can provide sufficient activation energy. The present results suggest propagation of vibrational energy through the polypeptide backbone is limited in travel by the rate at which vibrational energy is dissipated to contacting regions of the protein or to the surrounding solvent. It is possible that the dissipation of vibrational energy that accompanies downhill excitation energy transfer in photosynthetic light-harvesting proteins is associated with the IVE-driven conformational transitions that affect the energy-transfer yield in nonphotochemical quenching and other photoregulatory responses.

CHAPTER 3

Solvation Dynamics of the Hydration Shell of Zn^{II}-Substituted Cytochrome *c*[1]

Summary

The hydration shell of Zn^{II}-substituted cytochrome *c* (ZnCytc) was probed using the indolecyanine dye Cy5 using femtosecond pump–continuum-probe spectroscopy. Cy5 was attached to a surface lysine residue by a flexible linker; the distance between the surface of the protein and the chromophore was approximately 10 Å. Because Cy5's lowest energy $\pi \rightarrow \pi^*$ transition does not result in a change in permanent dipole moment, the solvation response measured by the rate at which the stimulated emission or excited-state absorption features in the pump–probe spectrum shift to the red or blue, respectively, can be treated approximately using the viscoelastic continuum theory described previously by Berg and coworkers.[79] Further, the damping of excited-state wavepacket motions along out-of-plane coordinates provides an additional measurement of the solvent viscosity. The main conclusion of this work is that the hydration shell is as much as 160 times more viscous than bulk water. A simple structural interpretation of this finding is that the hydration shell of ZnCytc is polarized by surface charges and by interruption of the long-range hydrogen bonding network by the folded protein

[1] This work was done in collaboration with Michael Bishop and Jerome D. Roscioli.

solute so that longer or more persistent chains of hydrogen-bonded water molecules are present than in the bulk.

3.1 Introduction

The hydration shell of a protein constitutes a domain of "biological water"[80-83] that contributes to the stability of the native folded structure[84-87] and to its biological function, especially in charge transfer or redox catalysis,[88] as a result of its distinct dynamical properties compared to the bulk.[89-92] Gruebele and coworkers used tetrahertz spectroscopy to probe the dynamics of the hydration shell by varying the concentration of a protein solution; they determined that the hydration shell has distinct properties that extend at least 1.0 nm from the protein surface.[93] Zewail and coworkers[81,82,94] used femtosecond time-resolved fluorescence measurements with probe chromophores on or tethered to a protein's surface to show that the diffusive (or random reorganizational) part of the polar solvation response observed using the dynamic fluorescence Stokes shift (FSS) is slowed at least to the 10–100 ps timescale from the sub-ps regime that is characteristic of bulk water.[95] Reorientational dynamics slow comparably in water near interfaces,[96,97] but the solvation response detected by intrinsic or protein-bound probes reaches well into the nanosecond regime.[6,48,98-103]

Considering that changes in the observed timescale follow the protein-folding state, the nanosecond part of the solvation response in proteins can be primarily attributed to protein-derived motions.[9] The contribution of the hydration shell to the detected solvation response, however, is not easily distinguished from that of

the protein.[19,88,104,105] In fact, molecular dynamics simulations by Matyushov and coworkers suggest that the motions of water molecules in the hydration shell on the nanosecond timescale arise from electrostatic interactions with surface charges and mechanical coupling (or "slaving"[54,106]) to conformational motions of the solvated protein.[88,107-110]

The long polar solvation timescales observed in the hydration shell were modeled phenomenologically by Bagchi and coworkers using a dynamic exchange of water molecules between the hydration shell and binding sites on the protein surface.[82,83] The Bagchi model holds that the structure of the hydration shell is equivalent to that of bulk water; the slow timescales arise from long residence times on the protein surface. Halle[91] has pointed out that the solvation dynamics results and Bagchi's exchange model are in conflict with the results of ^{17}O NMR relaxation dispersion (MRD) experiments and of molecular dynamics simulations of the dielectric response of a protein and its surrounding solvent, which suggest that the motions of water molecules in the hydration shell are only somewhat slowed compared to those in the bulk.[19] Halle and Davidovic[90,91] suggested that the apparent disagreement between the FSS and MRD experiments might be resolved if the viscosity of the hydration shell is larger than that of bulk water. Because the viscosity is a long-range or collective property of medium, Halle's picture requires that the water molecules in the hydration shell be organized differently than in the bulk.

One approach to test these hypotheses involves measuring the viscosity of the hydration shell of a protein using a nonpolar electronic probe. The change in a

probe's electronic structure that accompanies optical excitation usually results in a change in permanent dipole moment and a change in molecular cavity size. These changes elicit the polar and nonpolar parts of the dynamic solvation response, respectively.[79,111-117] There are a small set of probe molecules that do not exhibit a change in permanent dipole moment, however, and these molecules can be exploited to characterize the nonpolar solvation response separately.

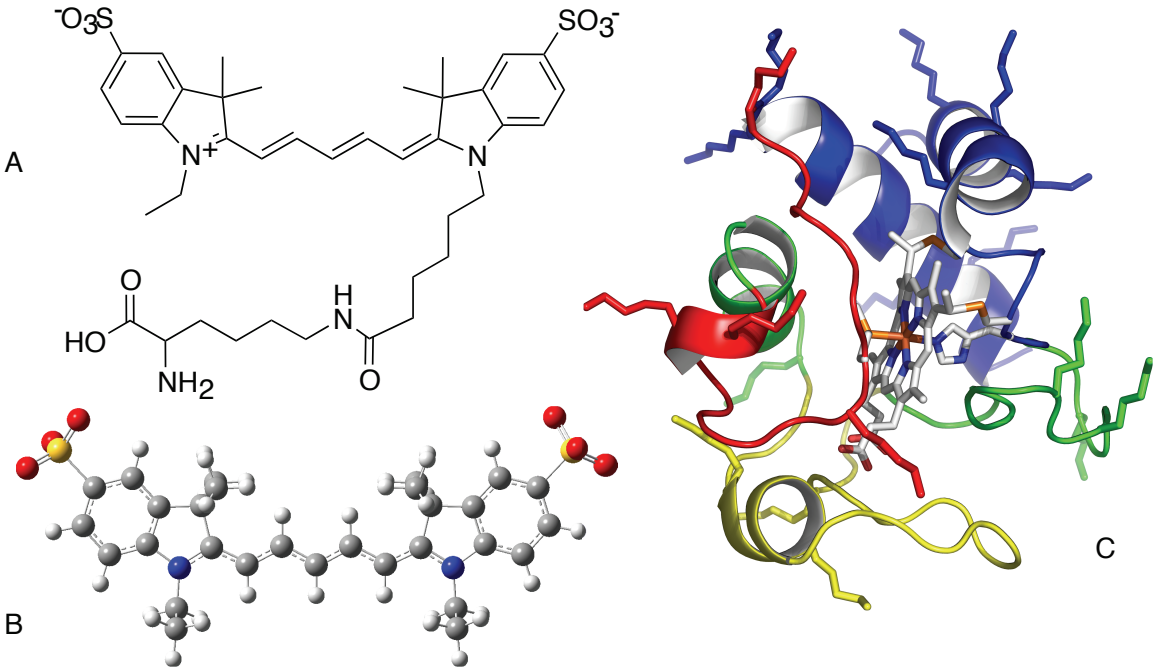

Figure 3.1 Structures of (a) Cy5–lysine adduct; (b) B3LYP/6-31G(d) structure for the ground-state Cy5 chromophore; (c) horse-heart ferricytochrome *c* (1HRC.pdb).[11] The protein is shown in a ribbon representation; the heme, amino acid residues Met80, His18, Cys14, Cys17, and the side chains of the lysine residues are shown in a stick representation. The polypeptide is color coded from red to blue following the scheme of Englander and coworkers:[57] residues 70–85 (red), residues 36–61 (yellow), residues 20–35 and 60–70 (green), and the N- and C-terminal α helices (blue).

The class of carbocyanine dyes that includes the probe called Cy5 are nonpolar solvation probes. The electronic structure of the Cy5 chromophore is comparable to

that of the structurally related dyes IR125 and HDITCP, which have been discussed by Jonas and co-workers.[118] Two resonance structures like the one shown in Figure 3.1a, each with a formal positive charge on one of the indole nitrogen atoms at the end of the conjugated polymethine chain and a mirror image of the other, contribute equally to the average structure of Cy5. The π-electron density and charge are extensively delocalized over the full length of the conjugated region; the $\pi \rightarrow \pi^*$ transition results in a symmetrical change in electron density with respect to the mirror plane, so the change in dipole moment is negligible. Thus, the time-integrated shift to the red of the continuous-wave fluorescence spectrum with respect to the absorption spectrum arises in Cy5 primarily from a nonpolar mechanism.

In the following, we describe a series of femtosecond pump–continuum-probe experiments employing Cy5 as a probe of the hydration shell of ZnCytc. Cy5 was obtained with a ~10 Å tether terminated with a succinimidyl ester group (NHS-ester) to allow conjugation with surface lysine residues. Using the continuum viscoelastic theory advanced by Berg,[79] the shift is treated in terms of the change in solute size or shape that accompanies the optical excitation and the phonon-induced and structural responses of the surrounding solvent cavity. The results show explicitly that the hydration shell is more viscous than is bulk water owing to the observation of much slower dynamic solvation and slower out-of-plane vibrational dynamics.

3.2 Experimental Section

3.2.1 Sample Preparation. Cy5 solutions in water were prepared using the amine monoreactive NHS ester of Cy5 (GE Healthcare, PA25001, see Figure 3.1a) in a 25 mM sodium phosphate buffer solution at pH 7.0; the NHS ester hydrolyzes to yield a carboxylate at the end of the tether after prolonged exposure in aqueous solution.

Zn^{II}-substituted cytochrome *c* (ZnCytc) was prepared from horse-heart ferricytochrome *c* using the procedure described in Chapter 2. The Cy5–ZnCytc complex was prepared by reacting a thawed sample of ZnCytc with amine monoreactive N-hydroxysuccinimidyl (NHS) ester of Cy5 to prepare nonspecifically a singly labeled, lysine adduct according to the vendor's protocol. Figure 3.1c shows the lysine side chains of ZnCytc to which the dye could bind. The reaction was conducted at a protein concentration of ~3 mg/mL at room temperature in a 100 mM sodium bicarbonate sample buffer solution at pH 9.3 with enough Cy5 dye to obtain at best a 1:1 stoichiometry; the low protein concentration favors a lower adduct yield. Repeated ultrafiltration cycles with additions of 25 mM sodium phosphate buffer solution at pH 7.0 over YM10 membranes (Millipore/Amicon) were used to separate unreacted and weakly bound Cy5 from the protein adducts. The adducts were concentrated further to obtain solutions for storage. The final concentrated product was stored at −80 °C in 25 mM sodium phosphate buffer solution at pH 7.0.

For use in the femtosecond pump–probe experiments, a solution of Cy5 or Cy5-ZnCytc were prepared by diluting concentrated solutions immediately prior to

the experiment to obtain an absorbance of 0.3 for a path length of 1.0 mm at the center of the laser spectrum at 665 nm. The samples were held in the femtosecond pump–probe spectrometer at room temperature (23 °C) in a stirred fused-silica cuvette (1.0 mm path length). The sample's absorption spectrum was monitored for changes arising from photochemistry or permanent photobleaching.

3.2.2 Mass Spectrometry. For use in mass spectrometric analyses, Cy5–ZnCytc and ZnCytc were treated with trypsin to obtain peptide fragments. After incubation overnight, the samples were analyzed using a Shimadzu Axima CFR Plus matrix–assisted laser desorption/ionization time-of-flight mass spectrometer (MALDI-TOF MS). The samples were prepared by placing 1 μL of sample (33.2 μM ZnCytc or 29.5 μM Cy5–ZnCytc in 1 mM phosphate buffer) on a MALDI plate with 3 μL of the matrix α-cyano-4-hydroxycinnamic acid in 3:1 acetonitrile:0.1% trifluoroacetic acid. The samples were allowed to dry before being placed into the mass spectrometer. For mass calibration, the YAGFLR peptide (726.4 Da), bradykinin (1059.6 Da), and angiotensin I (1297.5 Da) were used as standards. Peaks were processed using the mass list display in the Shimadzu Biotech MALDI-MS program.

3.2.3 Continuous-wave Absorption and Fluorescence Spectroscopy. Absorption spectra were acquired with a Hitachi U-4001 spectrophotometer (2 nm bandpass). Fluorescence spectra were obtained using a home-built fluorescence spectrometer consisting of a Jobin-Yvon AH10 100 W tungsten-halogen light source, a Jobin-Yvon H10 excitation monochromator (4 nm bandpass), an Acton Research SP-150 emission spectrograph (2 nm bandpass), and a Jobin-Yvon Symphony CCD

detector. The spatially integrated power of the excitation beam, as estimated using a Coherent Fieldmaster power meter and associated silicon photodiode detector, was 10 μW at 522.9 nm. Fluorescence emission spectra were acquired as the average of twenty 60-second exposures of the CCD detector. The CCD detector employs a liquid nitrogen cooled, back-illuminated, 2000 × 800 pixel silicon detector chip (EEV corporation). A 300 groove/mm diffraction grating (500 nm blaze wavelength) was mounted in the emission spectrograph, resulting in a 270 nm spectral range imaged over 2000 vertically-binned channels on the CCD detector chip. As presented as a function of wavenumber, the fluorescence intensities are multiplied by the square of the wavelength in order to compensate for the fixed (in wavelength units) spectral bandpass of the emission spectrograph. The absorption instrument is controlled by Hitachi UV Solutions. The fluorescence instrument is controlled by LabVIEW (National Instruments) programs.

3.2.4 Femtosecond Spectroscopy. Femtosecond pump–continuum-probe experiments were conducted with pump pulses from an optical parametric amplifier (OPA, Coherent OPA 9450), which was driven by a 250-kHz regeneratively amplified Ti:sapphire laser (Coherent RegA 9050 amplifier and Coherent Mira-Seed oscillator). The oscillator group-delay and amplifier were pumped continuously by Coherent Verdi V5 and V10 Nd:YVO_4 lasers. The signal-beam output of the OPA was compensated for group-delay dispersion by an SF10 Brewster prism pair and variably delayed by a retroreflector on an optical delay line driven by a Melles-Griot Nanomover actuator. The pump–pulse duration was measured to be 45 fs at 665 nm by a zero-background autocorrelator using a 100-μm KDP crystal; the spectrum was

determined to be 18 nm in width (fwhm) centered at 665 nm by an Ocean Optics U2000 spectrometer (0.5 nm bandpass).

Probe pulses were obtained from a chirp-compensated, single-filament femtosecond continuum, which was generated as the seed pulses for the first gain pass in the OPA. The chirp on the probe beam was compensated over the 500-780 nm range using a pump-delay program controlled by a third-order polynomial with respect to the probe wavelength. The chirp program was determined using optically heterodyne-detected optical Kerr-effect measurements of the probe arrival delay at the sample position as a function of probe wavelength. The rise time (10% to 90%) for the pump–probe signal was typically 75 fs for a 4 nm probe bandpass.

For pump–probe measurements, the planes of linear polarization of the pump and probe beams were set to be 54.7° apart as incident on the sample using calcite polarizers and $\lambda/2$-retarding wave plates. The probe intensity was detected by a Thorlabs PDA-55 amplified photodiode after it passed through the sample and a double-subtractive monochromator (Spectral Products CM112) with a 4 nm bandpass. The pump–probe signal was obtained as the normalized pump-induced change in probe transmission ($\Delta T / T$) signal using a SRS SR-830 lock-in amplifier referenced to the sum frequency of the pump and probe modulation frequencies (4.1 kHz for ΔT, Palo Alto Research model 300 chopper) and a SRS SR-850 lock-in amplifier referenced to the probe modulation frequency (2.5 kHz, for T).

3.2.5 Computational Chemistry. The optimized structure for the Cy5 chromophore shown in Figure 3.1b was obtained with Gaussian 03[119] using the

B3LYP density functional and the 6-31G(d) level of theory. The length of the flexible tether between the tagged lysine residue's α carbon and the N atom in the indole moiety at the other end of the tether was estimated with structures optimized using the UFF molecular mechanics force field.

3.3 Results

3.3.1 Mass Spectrometry.[2] In order to assign the position of the Cy5 molecule on the surface of ZnCytc, enzymatic digestion of the protein was followed by MALDI-TOF mass spectrometry. The results indicated that the fragment containing peptides 81-87 had the highest probability of having Cy5 conjugation, which indicates conjugation to either Lys86 or Lys87. The fragment containing Lys22 was the next most likely candidate, followed by the fragment containing Lys72. According to Gibson and coworkers,[120] the six most reactive lysines of the 18 lysines in cytochrome *c* are residues 86, 25, 72, 13, 87, and 22, in order of decreasing reactivity. With our results, this indicates that Lys86 is the most probable point of conjugation. While our results clearly indicated conjugation to three peptide fragments (four possible lysines), we cannot rule out the possibility that conjugation to other lysine residues occurs on occasion.

3.3.2 Continuous-wave Absorption and Fluorescence Spectroscopy. Figure 3.2 shows the room temperature absorbance and fluorescence spectra of each Cy5 in water with the femtosecond pump spectrum overlaid. The spectra

[2] The mass spectrometry work was performed by Jerome D. Roscioli of the Beck Group.

exhibit a main band (0–0 transition) flanked to higher and lower wavelengths, respectively, by a vibronic satellite. The spacing between the main band and the satellite in each spectrum is around 1100–1200 cm^{-1}, so the excited state structure is displaced mostly likely along a C-C or C-N bond-stretching coordinate. The breadth of the main band very likely conceals unresolved vibronic structure along lower-frequency vibrational modes. The approximate mirror symmetry for the absorption and fluorescence spectra provides strong evidence for a bound excited state that does not cross to a product state. In the related cyanine, 1,1-diethyl-4,4-cyanine (1144-C), which has a single carbon linker between the terminal ring structures, a barrierless ($E_a < k_B T$) *cis–trans* isomerization is thought to occur on the excited state potential over the 0.3 to 2 ps timescale.[121,122] Fluorescence emission during the crossing of the barrier between the *cis* and *trans* configurations gives rise to a pronounced red band, making the absorption and fluorescence spectra distinctly asymmetric. The mirror symmetry and vibronic progression observed for Cy5 indicate that the excited-state structure is displaced along in-plane and possibly out-of-plane vibrational coordinates, but it is unlikely that a significant fraction of the excited-state population executes a change in configuration.

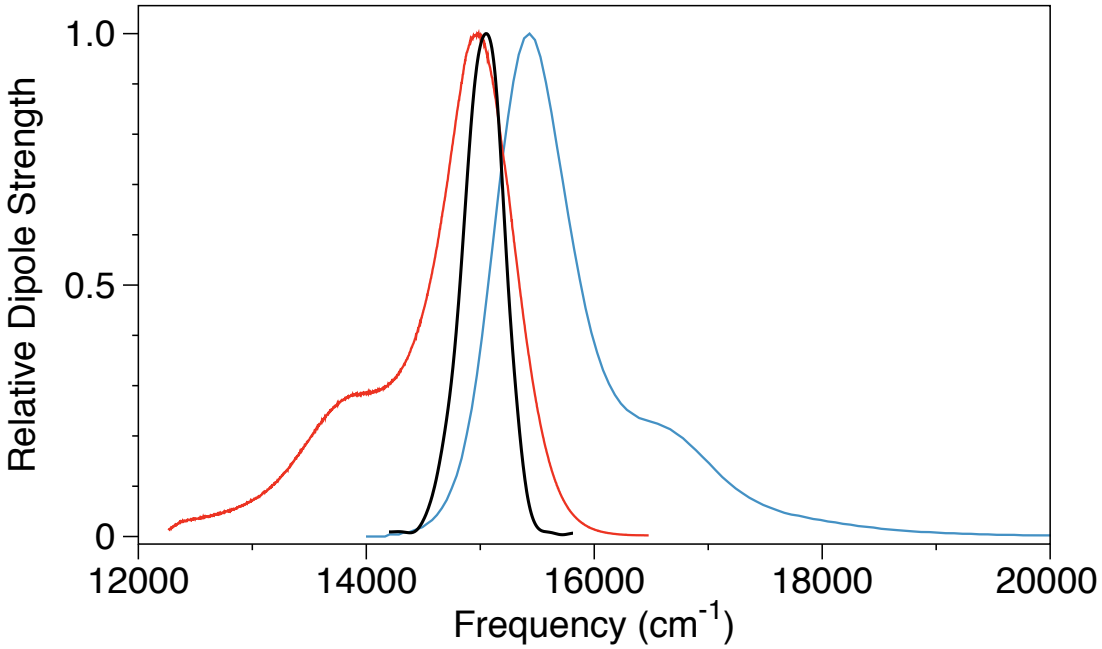

Figure 3.2 Continuous-wave absorption (blue) and fluorescence (red) spectra of Cy5 in water overlaid with the laser spectrum (black) and normalized to maximum peak intensity.

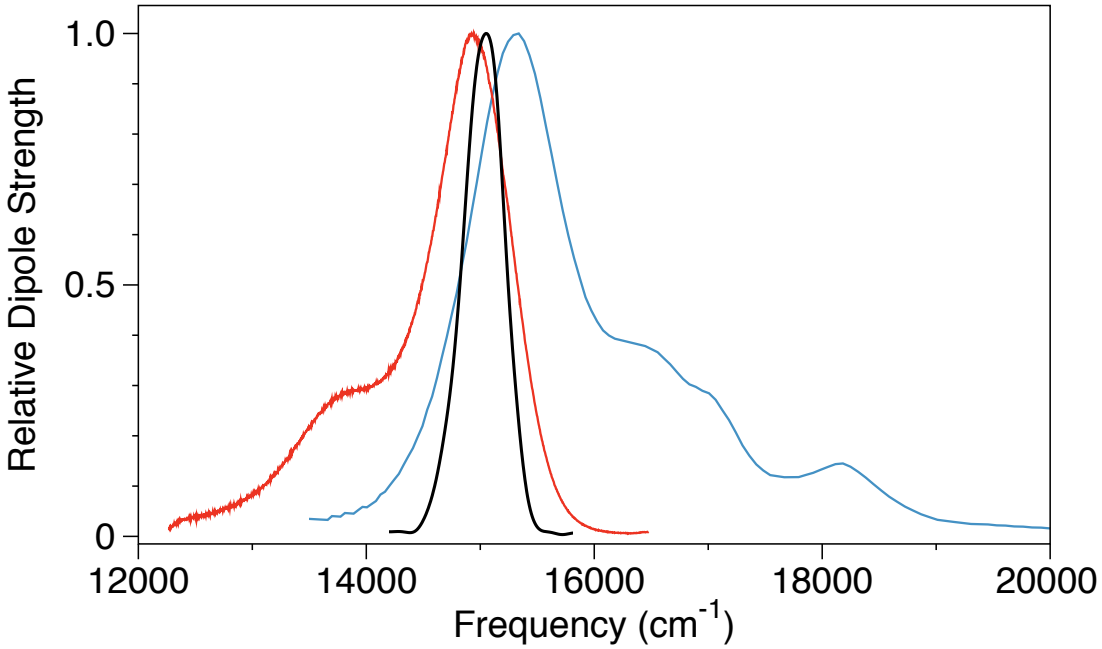

Figure 3.3 Continuous-wave absorption (blue) and fluorescence (red) spectra of Cy5–ZnCytc overlaid with the pump spectrum (black) and normalized to maximum peak intensity.

The absorption spectrum for the Cy5–ZnCytc adduct (Figure 3.3) exhibits the same features observed in the spectrum from Cy5 in water in addition to absorption features from the Q-band of the Zn^{II} porphyrin. The absorbance peak is red shifted by about 100 cm^{-1} relative to the absorbance peak of Cy5 in water, which indicates an increased polarizability or density in the hydration shell compared to bulk water. The peak of the fluorescence spectrum of Cy5–ZnCytc is red shifted 40 cm^{-1} relative to the peak of the Cy5 fluorescence spectrum, which is an indicator of the reorganization dynamics for fluorescence reporting slower dynamic solvation in the hydration shell. In spite of the contribution of ZnCytc to the absorbance spectrum of the Cy5–ZnCytc adduct and the shift relative to the spectra of Cy5 in water, excitation by the laser spectrum is expected to excite only Cy5, not the Zn^{II} porphyrin, so the resulting fluorescence spectrum is expected to be a result of Cy5 fluorescence, not ZnCytc fluorescence. Observed changes in the Cy5 fluorescence spectrum can, therefore, be assigned to differences in the immediate environment of the chromophore which will be further elucidated by the time-resolved spectroscopy.

The solvation reorganization energy observed is 225 cm^{-1} for Cy5 in water and 195 cm^{-1} for Cy5–ZnCytc. Jonas and co-workers[118] found the solvation reorganization energy for HDITCP and IR125 to be 270 cm^{-1} and 259 cm^{-1}, respectively. These dyes were found to have no change in solvent reorganization energy as the polarity of the solvent was varied. The conjugated polyene is shorter in Cy5 than IR125 or HDITCP by one single/double bond segment but is otherwise

isostructural, so a similar independence for the solvation reorganization energy with respect to solvent polarity is expected.

3.3.3 Pump–Continuum Probe Spectroscopy. Figure 3.4 shows time-resolved pump-probe spectra for Cy5 in water with probe delays from −20 fs to 54 ps. The change in transmittance over the intensity of the probe at that wavelength is reported as $\Delta T / T$. Each spectrum shown is the sum of photobleaching (PB) and stimulated emission (SE) signals, which are positively signed reflecting an increase in transmittance, and an excited-state absorption (ESA) signal, which is negatively signed reflecting a decrease in transmittance. The early-time spectra show PB+SE character well outside of the hole-burning PB region (Figure 3.4 top panels), suggesting that the homogeneous line width is broader than the laser spectrum's bandwidth. The earliest-time spectrum (Figure 3.4, –20 fs) shows a relatively mirror-symmetric signal around the 0–0 vibronic position that is comparable to the sum of the absorption and fluorescence dipole-strength spectra. By 0 fs the blue shoulder is decreasing due to the onset of an ESA signal which builds and blue-shifts. This evolution of the ESA feature is mostly complete by 500 fs. During this same time period, the red shoulder of the main peak grows to a maximum at about 50 fs owing to photobleaching of the ground state and red-shifting SE due to solvation. This blue shifting ESA and red-shifting SE during this time period is also consistent with excited-state twisting, similar to what Mathies, Shank, and coworkers observed during the photoisomerization of rhodopsin[123] and bacteriorhodopsin.[124] The Cy5 molecule, however, does not appear to form an isomerization product as evidenced by the lack of a red tail in the fluorescence

spectra, as mentioned above, but it likely experiences excited-state motion along torsional coordinates due to the loss of π-bonding character in the first excited state. After about 500 fs, most of the dynamic character of the spectra is complete, and the spectra decay as the ground state is repopulated. These results indicate contributions from excited-state motion and nonpolar solvation.

Figure 3.5 shows a similar set of time-resolved pump-probe spectra for Cy5-ZnCytc. The time evolution of the spectra is comparable to that for Cy5 in water, but there is more line broadening and the spectra change much more slowly with time.

In both sets of spectra, the pump-probe spectrum evolves over time as the excited Cy5 molecule moves toward the minimum of the excited state potential energy surface. In the ground state, electron density is distributed across the terminal ring structures of Cy5 and conjugated polyene connecting them. The conjugation is disrupted as one electron is excited from the ground state, allowing the molecule to twist as it moves along the potential energy surface. As the molecule moves in the excited state and the probe pulse arrives, SE or ESA evolve and eventually decay as the ground state is repopulated.

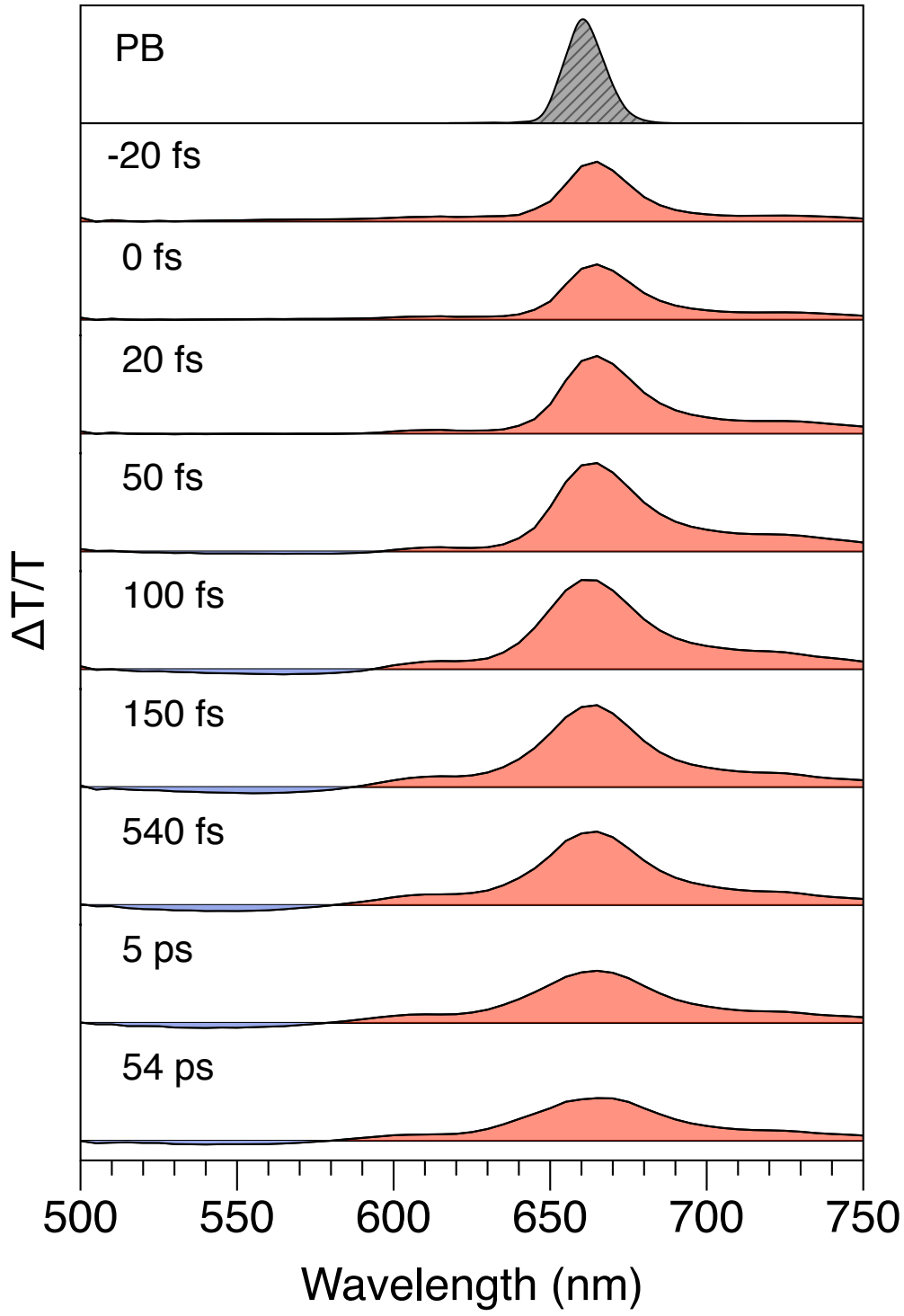

Figure 3.4. Time-resolved pump-probe spectra for Cy5 in water with probe delays from −20 fs to 54 ps.

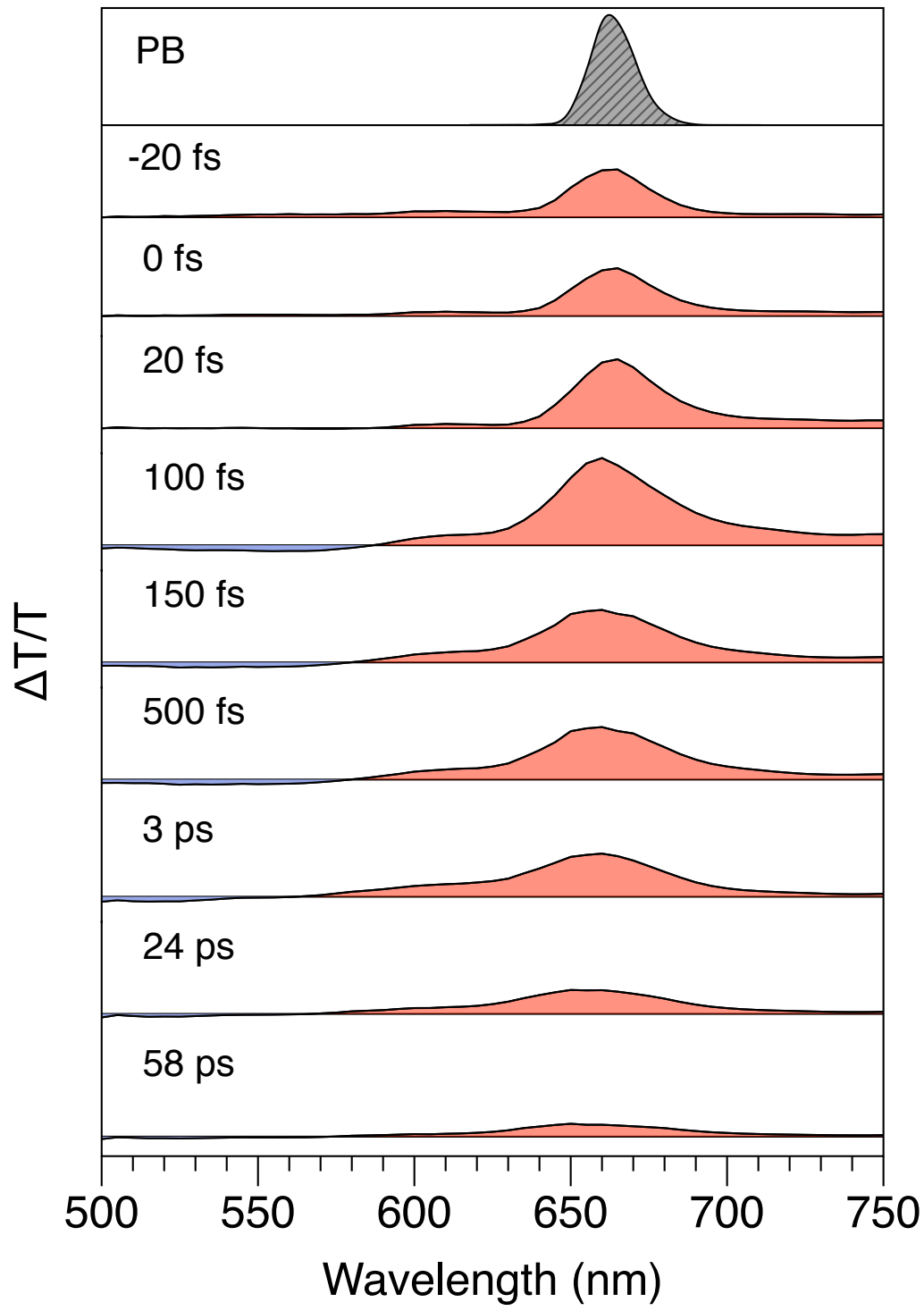

Figure 3.5. Time-resolved pump-probe spectra for Cy5–ZnCytc with probe delays from –20 fs to 58 ps.

Figures 3.6 and 3.7 show two time scales of an analysis of Cy5 in water obtained by calculating the mean frequency after isolating the peaks of the spectra which were shown in Figure 3.4. The data was fit to the equation:

$$f(t) = A_1 e^{-t/\gamma} \cos(\omega t - \phi) + A_2 e^{-t/\tau 2} + A_3 e^{-t/\tau 3} + A_4 e^{-t/\tau 4} + A_5 e^{-t/\tau 5} \qquad (3.1)$$

The parameters of the fit are shown in Table 3.1. The model equation is used to describe the signal in order to compare the response observed in bulk water and the hydration shell. The plot in Figure 3.6 shows an initial rapid red shift, followed by a blue shift, and subsequent oscillation of the spectrum, which can also be seen at longer delays in Figure 3.7. As observed in Figure 3.4, the most significant changes are complete by 500 fs, which is related to the shift of ESA. The oscillatory response comes from a combination of the oscillatory motions of the SE and ESA parts of the signal given that the window over which the mean frequency was calculated spans only the central PB-SE peak.

$$\langle \nu(t) \rangle = \frac{\int_{\nu_1}^{\nu_2} d\nu \, \nu I(\nu, t)}{\int_{\nu_1}^{\nu_2} d\nu \, I(\nu, t)} \qquad (3.2)$$

Figures 3.8 and 3.9 show similar mean frequency analysis for Cy5–ZnCytc on the same time scales shown in Figures 3.6 and 3.7. Note that the overall shift of the mean frequency is greater for Cy5–ZnCytc. The initial rapid red shift is comparable in magnitude to that observed for Cy5 in water. It is followed by a blue shift approximately double that seen in Cy5 in water, oscillation that is not as pronounced, and a final, slow blue shift. This data also confirms the previous results that the ESA shift is complete by 500 fs.

Table 3.1. Fit parameters for the mean frequency model of Cy5 in water and Cy5-ZnCytc, as shown in Figures 3.6-3.9. The parameters correspond to Equation 3.1.

	A_1	γ	ω	A_2	τ_2	A_3	τ_3	A_4	τ_4	A_5	τ_5
Cy5-Water	**0.40**	**58 fs**	**136 cm^{-1}**	**0.17**	**438 fs**	**-0.30**	**758 fs**	**0.13**	**1.38 ps**	**---**	**---**
Cy5-ZnCytc	**0.46**	**77fs**	**133 cm^{-1}**	**-0.17**	**287 fs**	**-0.01**	**801 fs**	**-0.13**	**4.01 ps**	**-0.22**	**216 ps**

Table 3.2. Fit parameters for the 720 nm transients modeled to fit the data obtained from Cy5 in water and Cy5-ZnCytc, as shown in Figures 3.10-3.13. The parameters correspond to Equation 3.3.

	A_1	τ_1	A_2	τ_2	A_3	τ_3	A_4	τ_4	A_5	τ_5
Cy5-Water	**0.45**	**23 fs**	**0.25**	**1.00 ps**	**-0.02**	**3.85 ps**	**0.28**	**637 ps**	**---**	**---**
Cy5-ZnCytc	**0.70**	**13 fs**	**0.13**	**181 fs**	**0.06**	**2.20 ps**	**0.03**	**28.1 ps**	**0.08**	**890 ps**

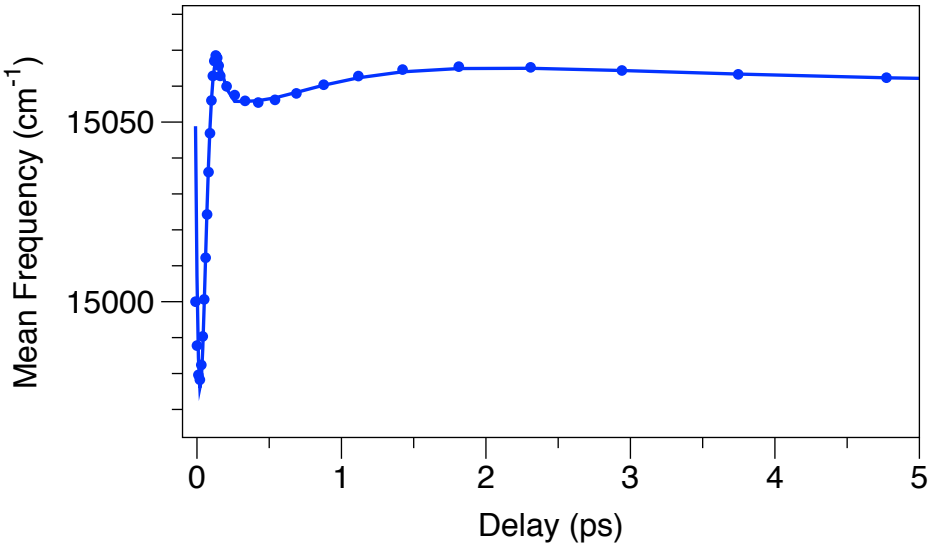

Figure 3.6. Time evolution of the mean frequency of the pump-probe spectrum of Cy5 in water at short delay times. The data points are overlaid with a fit to Equation 3.1, and the fit parameters are listed in Table. 3.1.

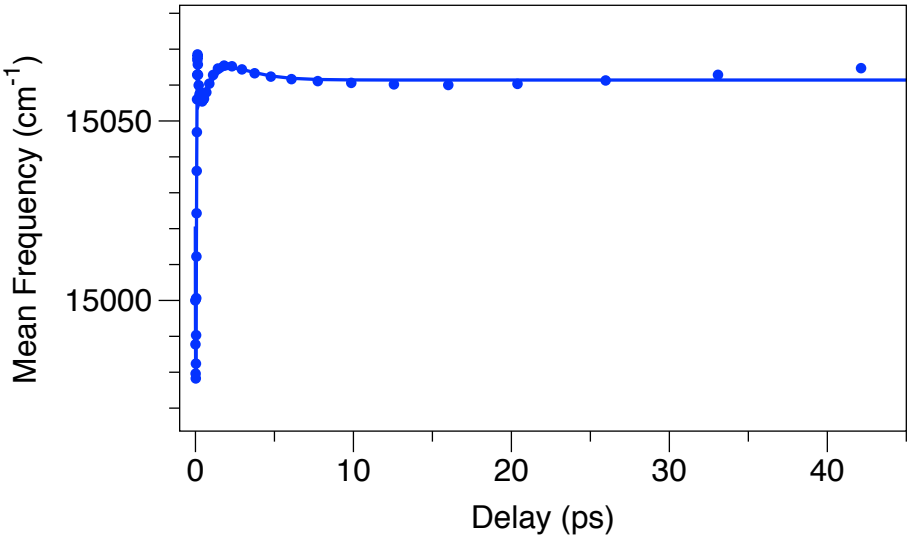

Figure 3.7. Time evolution of the mean frequency of the pump-probe spectrum of Cy5 in water. The data points are overlaid with a fit to Equation 3.1, and the fit parameters are listed in Table. 3.1.

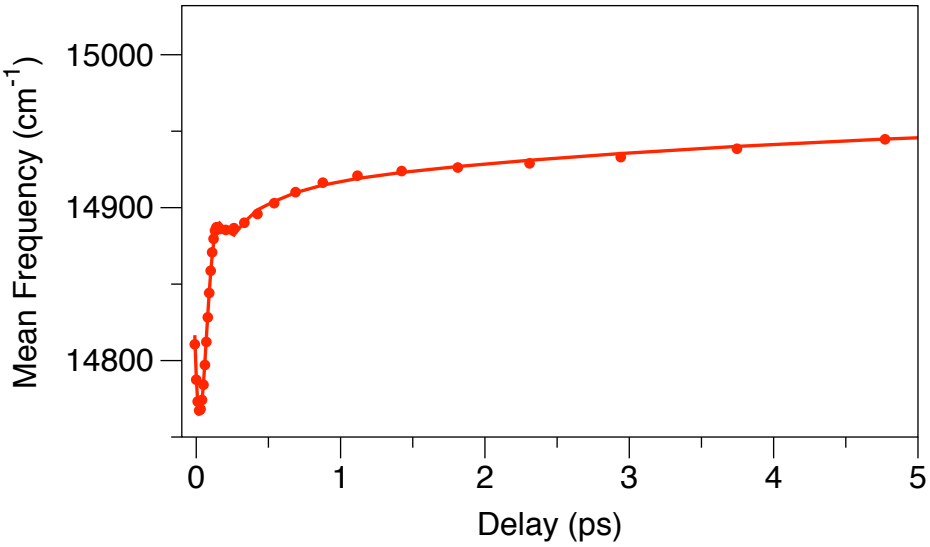

Figure 3.8. Time evolution of the mean frequency of the pump-probe spectrum of Cy5–ZnCytc at short delay times. The data points are overlaid with a fit to Equation 3.1, and the fit parameters are listed in Table. 3.1.

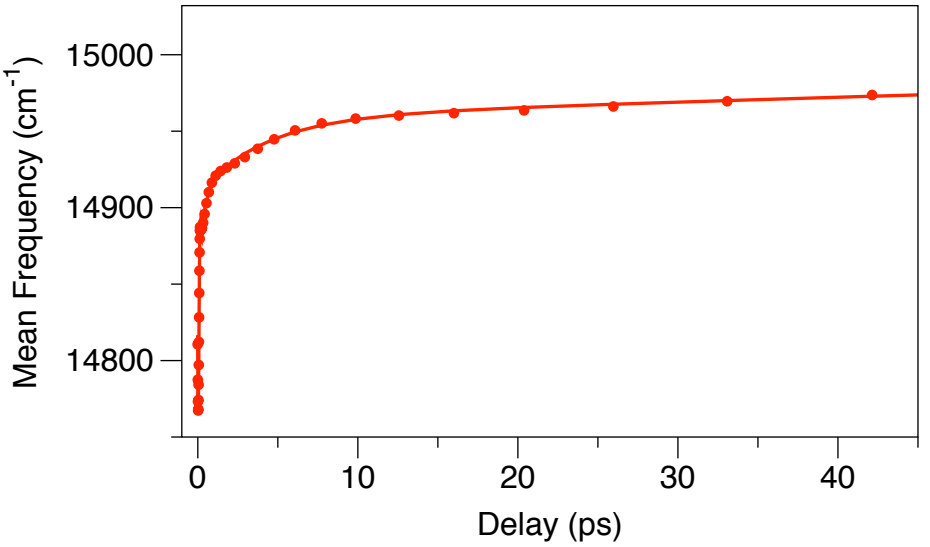

Figure 3.9. Time evolution of the mean frequency of the pump-probe spectrum of Cy5–ZnCytc. The data points are overlaid with a fit to Equation 3.1, and the fit parameters are listed in Table. 3.1.

The 720 nm transient in Figures 3.10 and 3.11 shows the time evolution of the pure SE region, fully resolved from the PB (absorption) spectrum. The data shown includes a data set at short times, up to 1 ps, and a data set out to a delay of 150 ps. The transients for each Cy5 in water and Cy5–ZnCytc are modeled by a sum of exponentials convoluted with an instrument response function:

$$f\left(x\right) = A_1 e^{-t/\tau 1} + A_2 e^{-t/\tau 2} + A_3 e^{-t/\tau 3} + A_4 e^{-t/\tau 4} + A_5 e^{-t/\tau 5} \qquad (3.3)$$

The signal for Cy5 in water shows an instrument-response limited rise, reporting exclusively stimulated emission from the excited state, followed by a multiexponential decay with timescales of 23 fs and 1 ps (see Table 3.2). Two subsequent timescales of 3.9 and 637 ps were measured on the same sample on a 150 ps time axis (Figure 3.11). Rapidly damped oscillations arising from vibrational coherence are clearly visible on the pump-probe transient at short times for both Cy5 in water and Cy5–ZnCytc (Figures 3.10 and 3.12). The timescales observed in Cy5–ZnCytc were 13 fs, 181 fs, 2.2 ps, 28 ps, and 890 ps. The vibrational coherence is not visible in Figures 3.11 and 3.12 due to the 1 ps step size used for this transient. Figures 3.12 and 3.13 show the oscillatory components of the residuals (signal-model) from Figures 3.10 and 3.11. The residuals were for Cy5 in water and Cy5–ZnCytc were plotted in Figures 3.14 and 3.15, respectively.

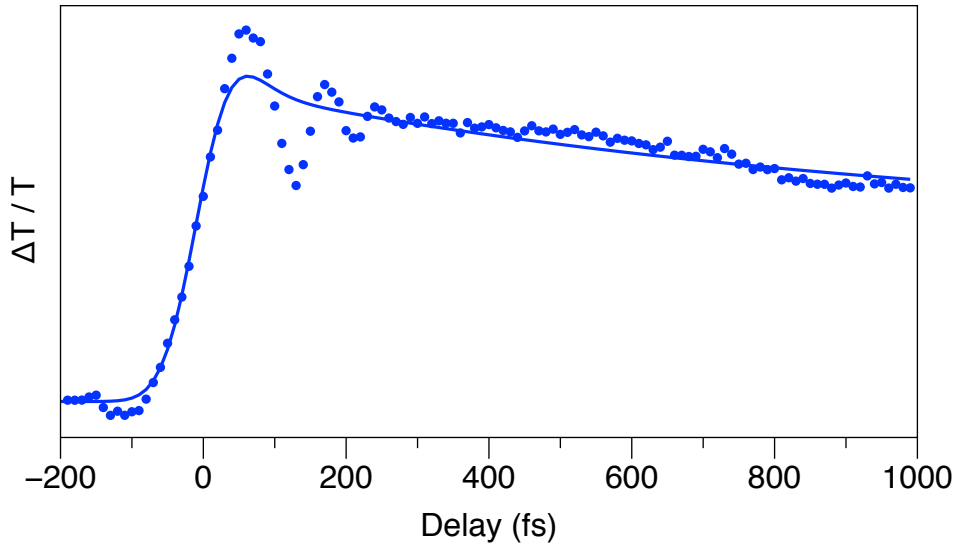

Figure 3.10. Pump-probe transient of Cy5 in water with the probe wavelength at 720 nm. The data points are overlaid with a fit to Equation 3.3; the fit parameters are listed in Table 3.2. The delay spacing in this experiment shows vibrational coherence not observed with greater step-size.

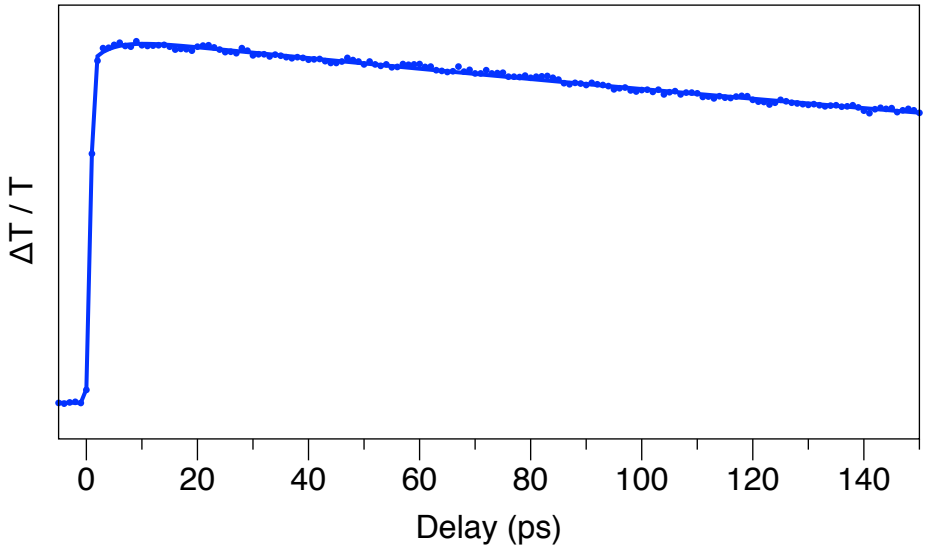

Figure 3.11. Pump-probe transient of Cy5 in water with the probe wavelength at 720 nm. The data points are overlaid with a fit to Equation 3.3; the fit parameters are listed in Table 3.2.

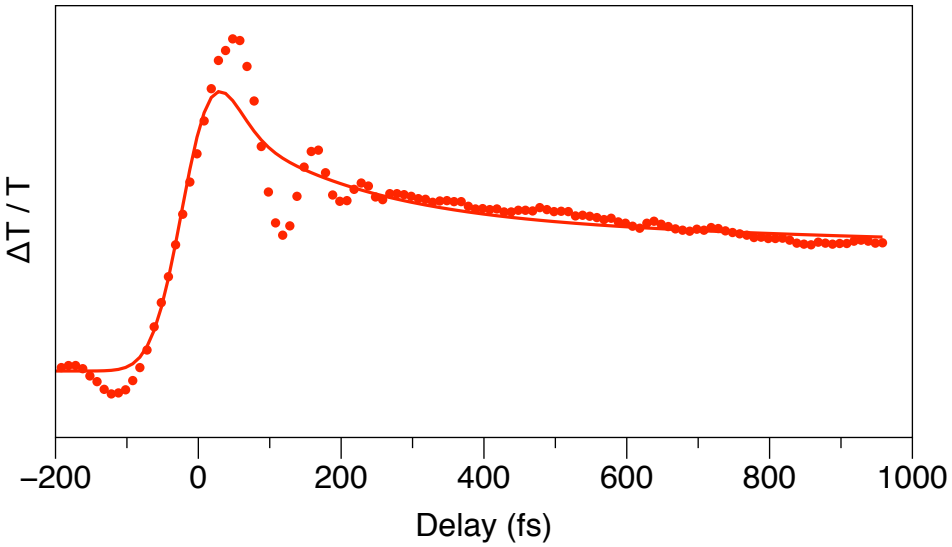

Figure 3.12. Pump-probe transient of Cy5–ZnCytc with the probe wavelength at 720 nm. The data points are overlaid with a fit to Equation 3.3; the fit parameters are listed in Table 3.2. The delay spacing in this experiment shows vibrational coherence not observed with greater step-size.

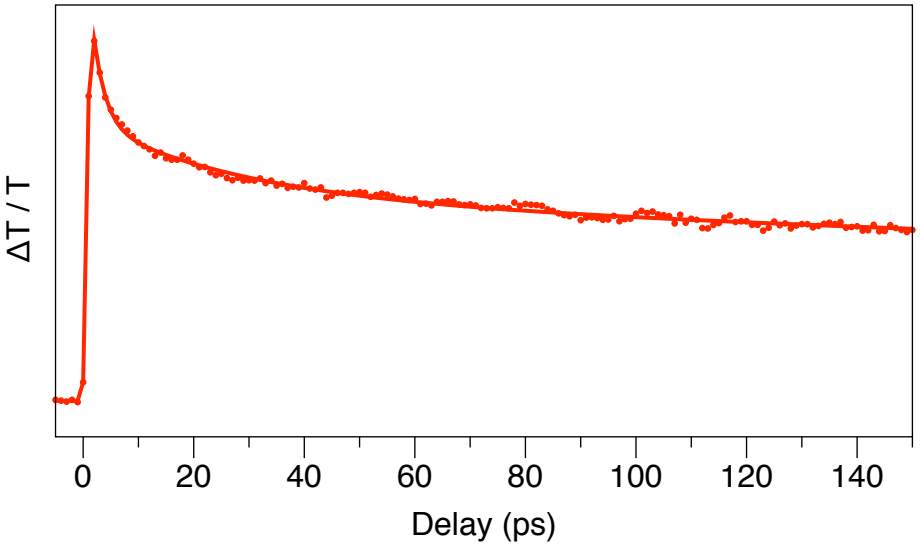

Figure 3.13. Pump-probe transient of Cy5–ZnCytc with the probe wavelength at 720 nm. The data points are overlaid with a fit to Equation 3.3; the fit parameters are listed in Table 3.2.

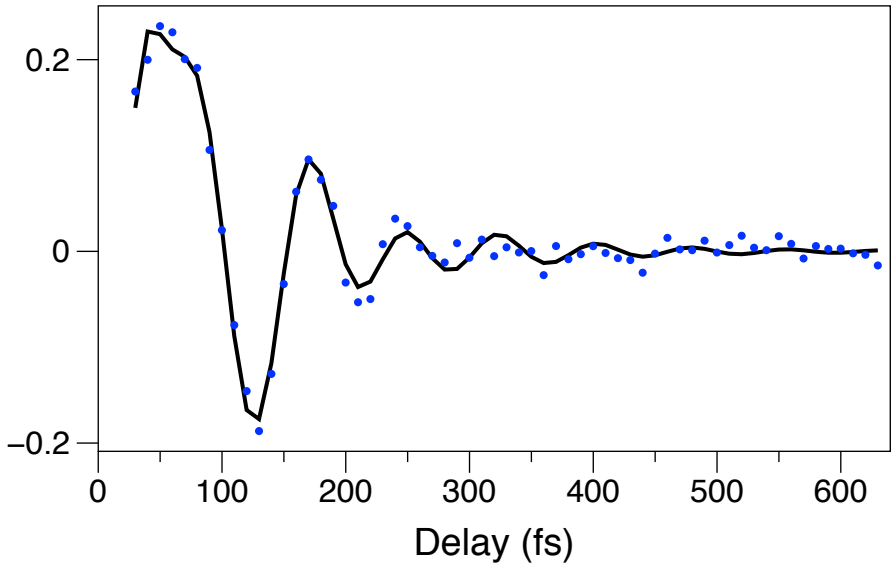

Figure 3.14. Oscillatory residuals (data − fit) from the pump-probe transient of Cy5 in water with the probe wavelength at 720 nm. The data points are fit to a set of damped cosinusoids using a LP-SVD program. The spectral density obtained from the fit is shown in Figure 3.16.

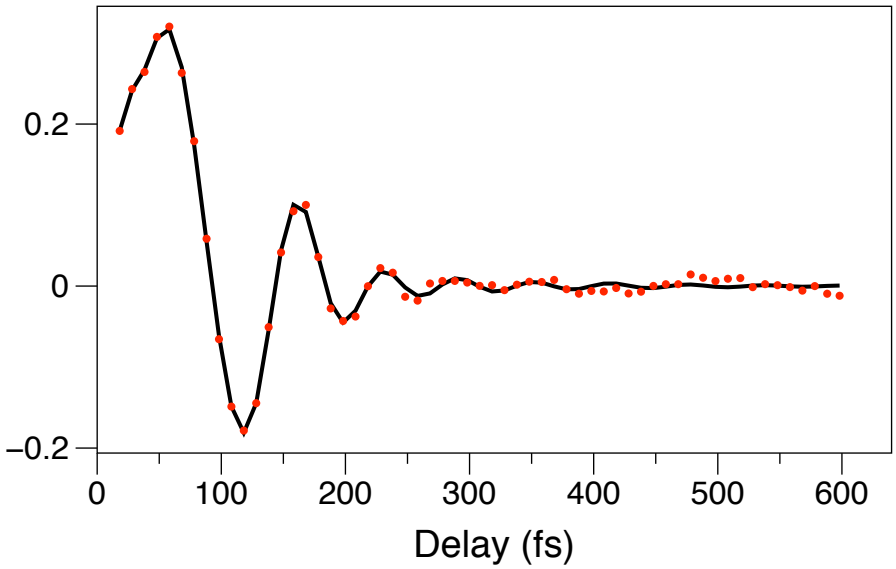

Figure 3.15. Oscillatory residuals (data − fit) from the pump-probe transient of Cy5–ZnCytc with the probe wavelength at 720 nm. The data points are fit to a set of damped cosinusoids using a LP-SVD program. The spectral density obtained from the fit is shown in Figure 3.17.

Figures 3.16 and 3.17 show the data modeled by a set of damped cosinusoids with a linear prediction, singular-value-decomposition (LP–SVD) program.[125,126] The model includes two components at 297 cm^{-1} and 431 cm^{-1} for Cy5 in water, with respective normalized amplitudes of 0.2 and 0.8. The corresponding model for the Cy5–ZnCytc transient (Figure 3.17) includes modulation components at 286 cm^{-1}, 420 cm^{-1}, and 538 cm^{-1} with respective normalized amplitudes of 0.6, 0.36, and 0.04. The components correspond most likely to out-of-plane normal modes of vibration for the Cy5 chromophore. These vibrations are rapidly damped because they result in twisting or bending of the conjugate polyene and accordingly effect large-amplitude motions of the indolium end moieties against the surrounding solvent cavity.

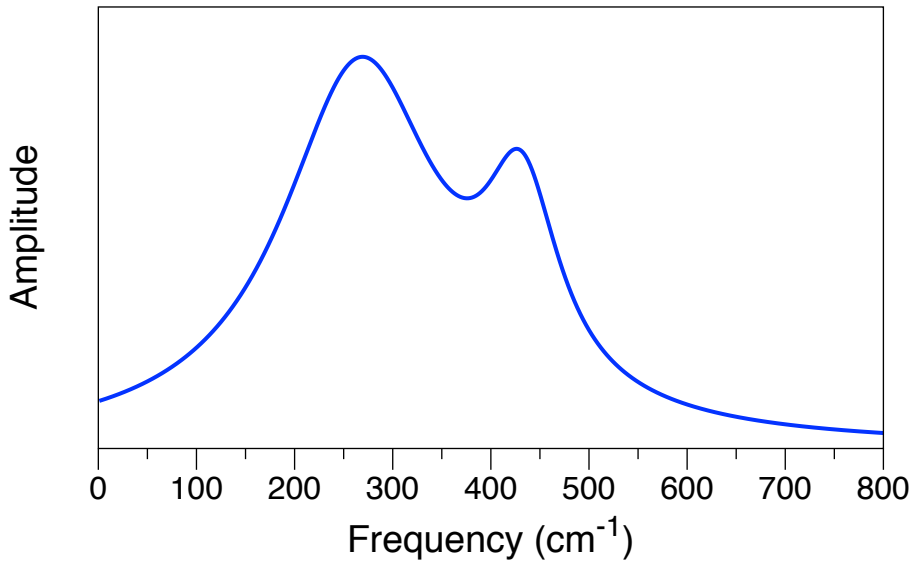

Figure 3.16. Spectral density obtained from the LP-SVD fit of the oscillatory part of the pump-probe transient of Cy5 in water with the probe wavelength at 720 nm (see Figure 3.14).

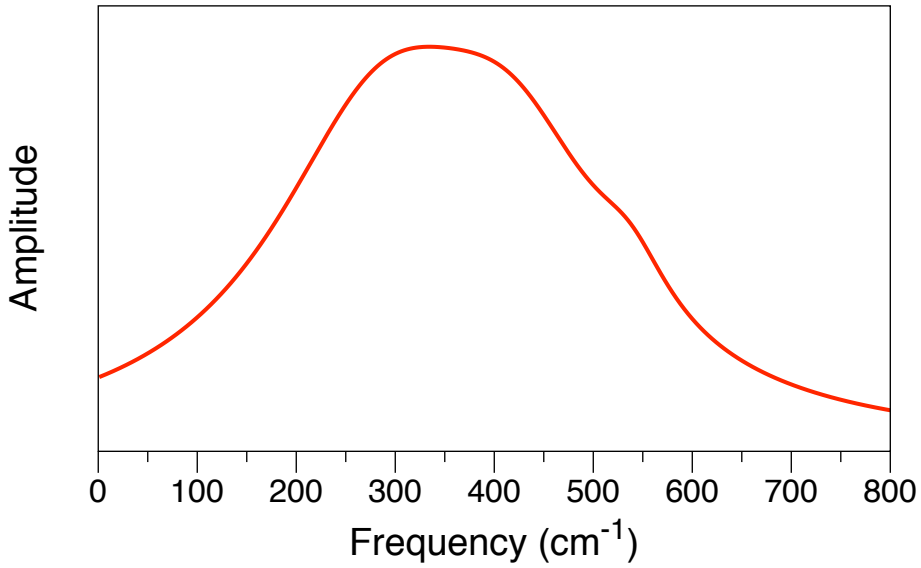

Figure 3.17. Spectral density obtained from the LP-SVD fit of the oscillatory part of the pump-probe transient of Cy5–ZnCytc with the probe wavelength at 720 nm (see Figure 3.15). Three frequency components at 286 cm^{-1}, 420 cm^{-1}, and 538 cm^{-1} were found for Cy5–ZnCytc.

3.4 Discussion

The design of this study helps to answer the question of whether water in the hydration shell is more viscous than bulk water. The absorbance and fluorescence spectra demonstrate displacement of the Cy5 excited state structure, but not transition to a product state. The pump-probe data elucidates the mechanical motion of Cy5. The mean frequency plot for each Cy5–ZnCytc and Cy5 in water shows damped oscillation due to the diffusive out-of-plane motion towards the excited state potential minimum, in which the molecule is in a twisted conformation. The SE vibrational coherence is damped at the same rate in bulk water and in the hydration shell, which indicates in-plane modes of vibration. The overall shift to the blue of the mean frequency is a result of the ESA shifting to the blue. This is a direct measure of dynamic nonpolar solvation and can be used to compare the relative

timescales in bulk water and the hydration shell, which was confirmed by transient grating and photon echo experiments.

The mirror-symmetry and vibronic progression of the fluorescence and absorbance spectra give strong evidence that the excited state structure is displaced, but does not cross to a product state. The mirror symmetry of the absorbance and fluorescence spectra showed that even as the excited state molecule exhibits damped oscillation of a twisting motion, Cy5 does not undergo a *trans* to *cis* isomerization. In addition, since the excited Cy5 molecule has two symmetric resonance structures that contribute equally to the structure, we conclude that the dipole moment doesn't change. Structural changes, therefore, whether in-plane or out-of-plane vibrations, are the primary result of optical excitation.

The pump-probe signals give information on the mechanical motion of the chromophore as limited by the surrounding solvent, whether in the bulk or in the hydration shell. The time evolution of the pump-probe signals, both in Cy5 in water and Cy5–ZnCytc show an initial evolution consisting of predominantly a small red shift of the stimulated emission portion, which should overlap with the fluorescence and with the motion of the excited state absorption. We can identify if this occurs by observing the time evolution of the series of spectra. At early time, the excited state absorption spectrum overlies most of the PB spectral region. At longer time, the ESA spectrum shifts to the blue. As it shifts, it causes the region of the PB spectrum to act like it's rising due to the fact that the ESA has moved to the blue so that the ESA signal is no longer subtracted from the positive signal. The spectrum also involves red-shifting of the stimulated emission. PB is stationary by definition, except for

some line broadening, which is due to the IVR and spectral diffusion. The motion of the ESA describes twisting of the chromophore around the double bonds, between the two cyanine end chromophores.

One of the things we can measure with the pump-probe signals is how the hydration shell limits the reorganizational motions of that chromophore. One way we can measure that is to look at the mean frequency by integrating over the central peak. This primarily tells us how the ESA moves. Bulk water clearly exhibits faster dynamics than water in the hydration shell. The initial red shift is the rapid part of the nonpolar solvation dynamics.[79] In water, the red shift is followed very quickly by a blue shift on almost the same timescale, due to the fast part of the ESA motion to the blue. The mean frequency then oscillates on the picosecond timeframe, finishing with a red shift that ends around 10 ps and a final, very small blue shift that extends out to 50 ps. This describes a damped motion of the chromophore on the torsional coordinates. This is limited to some degree by the surrounding solvent. If you compare the mean frequency response of Cy5 in water to Cy5-ZnCytc, the oscillation of the response in the hydration shell of ZnCytc appears more damped, though the magnitude of the overall response is larger. In addition to this oscillation being more damped in the hydration shell, the damping time, γ, of the oscillation is longer in the hydration shell. This is one measure of the viscous damping of Cy5 out-of-plane motions. The magnitude of the initial red shift of Cy5 is comparable in both environments. The next blue shift is significantly larger in Cy5-ZnCytc and then the oscillatory behavior is damped, even on an absolute scale. Finally, there is a net shift of the signal to the blue for Cy5–ZnCytc. The red shift seen on the intermediate

timescale in bulk water is not apparent in the hydration shell. This shows, directly, that most of this signal response is due to the motion of the ESA and of the wavepacket that makes the stimulated emission move back and forth. When comparing the longest timescales, τ_4 of Cy5 in water and τ_5 of Cy5-ZnCytc, the latter is 160 times greater, indicating a significant increase in viscosity. The longest time constant in the Cy5–ZnCytc response (216 ps) demonstrates that the blue shift of the ESA dominates the results measured by mean frequency, which occurs as the system moves toward the excited state minimum on the potential energy surface, which is a twisted structure. While oscillations are damped for both Cy5 in water and Cy5–ZnCytc, on the long timescale, we can clearly see that the response on the hydration shell is much slower than that in the bulk water.

Some of the same information is obtained by looking at the stimulated emission directly in the 665nm pump–720nm probe (Figures 3.10-3.13). This probe wavelength primarily gives information related to stimulated emission. The fast part of this is the twisting motion along vibrational coordinates. In both bulk water and the hydration shell, the vibrational coherence damps by about 300 fs. These are long-range out-of-plane motions that are initially damped. The signal then responds, going to completion as judged by the mean frequency, and is mostly complete by a picosecond. The overall population decay occurs over a longer timescale in water, but that is due to solvation dynamics, not motion. In the protein case, the damping of the signal is very similar or perhaps a little faster damping than in bulk water, but then the blue shift, which influences the mean frequencies shifting to the blue gives rise to a decay in the SE, and that is much slower in hydration shell. From the

pump-probe data, we conclude that the slowest part of the response measured in the hydration shell is at least on the 30 ps timescale given the model. The long component is due to mechanical relaxation of the chromophore and this twisting and is a direct measure of viscosity. It appears that the timescale in the hydration shell is about 160 times slower for the bulk water. For comparison with other liquids, the increase in viscosity in the hydration shell of a protein indicates a viscosity is intermediate between the viscosity of ethylene glycol and glycerol. The viscosity of bulk water at room temperature is 1.0 cP. The value for ethylene glycol is 16 cP, and for glycerol is 1400 cP. With an approximately 160 times increase in viscosity compared to bulk water, we can estimate about 160 cP, which is ten fold that of ethylene glycol and about a tenth that of glycerol. This increased viscosity suggests that they hydration shell contains chains of water that are longer and/or more persistent than those found in bulk water. This occurs because the presence of a protein interrupts the long-range hydrogen bonding structure and because the surface of the protein is charged. The charges on the surface of the protein are expected to introduce order to the water molecules, whereby they assume a low-energy arrangement along the protein surface of an ordered hydrogen bonding network that can extend away from the interface and persist longer temporally. The lysine residues are primarily on the front side of the protein, where the overall charge is positive (see Figure 3.1c), which may impact how hydrogen bonding occurs in the hydration shell and, thereby, impact the viscosity. While this study is focused on the hydration shell of ZnCytc, it would be interesting to conduct a similar study using a protein with a surface containing fewer charged amino acids to

determine how the number of surface charges or whether proximity of like charges impact the viscosity of the hydration shell.

The pump-probe signals tell us mostly about mechanical motion that is frictionally limited. Our results show two significant pieces of information: the mechanical/frictional damping on the fast timescale is not much different in the hydration shell than bulk water, but is much slower in the hydration shell on the slow timescale.

CHAPTER 4

Conclusions

The experiments described in this work provide an improved picture for the nature of the structural changes in ZnCytc upon optical excitation and give further insight into differences between the behavior of water in the hydration shell as compared to the bulk. In Chapter 2, we set out to further elucidate the nature of the partially unfolded structures produced by the IVE process in ZnCytc. We found that a specific omega loop of the protein is most likely to be involved in changing the environment of the porphyrin. In Chapter 3, we set out to describe the behavior of water in the hydration layer by probing the region with a dye attached to the surface of the protein. We found that the viscosity of the hydration shell is much greater than the viscosity of water in the bulk because the water molecules are polarized by surface charges and probably form longer or more persistent hydrogen-bonded chains than in bulk water.

In Chapter 2, we reviewed the energy landscape/protein folding funnel hypothesis[1-4,24,52,55,56] which describes the potential energy surface of a protein as the protein folds. This hypothesis suggests that proteins fold (or unfold) through a range of trajectories rather than a single discrete pathway of intermediate states. The IVE experiment was initially designed as a method to unfold the protein, ZnCytc, using optical excitation.[25,48] This set of experiments helped elucidate how the protein is affected by an optically-excited intrinsic Zn^{II}-porphyrin. Our results indicate that an omega loop (the green loop in the Englander color scheme[57]) of the

protein undergoes a conformational change after IVR from the excited porphyrin. This region was identified to be adjacent to Cys14 and Cys17, which are connected to the porphyrin via thioether linkages. Of the areas adjacent to these bonds, the identified loop was chosen based on how its movement would affect the porphyrin. This result appears to be dependent upon the thioether linkages connecting the porphyrin to the protein, which means the result cannot be directly applied to LHCII. ZnCytc was originally chosen for two reasons: it contains an intrinsic chromophore and is a model for a single-chlorophyll containing system.

We concluded that a small section of the protein adjacent to the porphyrin and near the thioether linkages involving Cys14 and Cys17 undergoes a conformational change after excess vibrational energy is transferred via IVR from the Zn^{II} porphyrin. We reached this conclusion because the IVE profiles obtained at multiple temperatures and various concentrations of Gdm^{+} all show a red–blue–red shift. The origin of the transitions in the IVE profile are conformational changes (transition I) and partial unfolding (transitions II and III). Further, through-bond energy transfer is rapid relative to energy transfer by collision, so IVR is most likely to occur through the thioether linkages. This excess energy effects change, specifically the conformational changes and partial unfolding associated with the transitions described. Lastly, the loop of the protein adjacent to the face of the porphyrin is most likely to affect the π-electron density of the porphyrin, which will impact fluorescence. This is a significant result because, rather than a specific unfolding trajectory, it indicates that a range of partially unfolded structures are populated during spontaneous protein folding.

The time-integrated experiment presented in Chapter 2 would not be well-suited for use with a multi-chlorophyll system like LHCII. Due to the presence of many chromophores in LHCII, the position of the initial excitation would be ambiguous and downhill energy transfer would result in vibrational excitation in many positions in the protein for each optical excitation event that would occur. In addition, the chromophores in LHCII are not bound to the protein by thioether linkages, so energy transfer that occurs will not take place through bonds. Energy transfer that occurs by collision is expected to be slower than through-bond energy transfer. The vibrational energy is likely to be diffused more evenly around the chromophore than a system where energy is transferred through bonds.

In Chapter 3, we described previous work studying the hydration shell of proteins and the conclusion that water in the hydration shell behaves differently than in the bulk.[80-83,89-92] The stability of a native-fold protein is affected by the hydration shell immediately surrounding the protein,[84-87] to a distance at least 1.0 nm from the surface.[93] While there is an effect on water when it is in the presence of any interface,[96,97] the effect appears more pronounced in the hydration shell of a protein as the solvation response is even slower.[6,48,98-103] Since there is mechanical coupling of the protein and the hydration shell[54,106], this experiment was designed to separate the results shown in previous work from what would be observed by using a tethered chromophore in the hydration shell. The hydration shell had previously been modeled,[82,83] so we set out to test those results.

The experiment was designed to allow description of the hydration shell of a protein. The pump-probe experiment elucidated the mechanical motion of the

cyanine dye, Cy5. Specifically, the measured timescales in bulk water and the hydration shell differed significantly. The timescale observed in the hydration shell was a factor of 160 greater than the timescale observed for Cy5 in bulk water. The fluorescence and absorbance spectra exhibit mirror-symmetry and vibronic progression indicating that the excited state structure is displaced relative to the ground state, but does not cross to a product state. Even as the molecule experiences twisting, it does not undergo a *trans* to *cis* isomerization. Since the Cy5 molecule has two symmetric resonance structures in the excited state that contribute equally to the overall structure, it is clear that the dipole moment does not change when the molecule is excited. This indicates that optical excitation results in structural changes, whether they are in-plane or out-of-plane. The experiment allows a measurement of how the hydration shell limits reorganization of the chromophore molecule. The dynamics in the hydration shell are significantly slower than those seen in bulk water. In the hydration shell of Cy5–ZnCytc, the magnitude of the overall response is larger and more damped than that of Cy5 in bulk water. In addition to being more damped, the damping time is longer in the hydration shell. This is a result of the viscous damping of Cy5 out-of-plane motions. While there is damping in both Cy5 in bulk water and Cy5 in the hydration shell of ZnCytc, the response observed in the hydration shell is much slower than that in bulk water.

This dissertation contributes to understanding how energy of optical excitation is distributed by vibrational equilibration in chromoproteins, such as those involved in photosynthesis or in vision, prior to fluorescence emission and further elucidates

the behavior of water in the hydration shell of the ZnCytc system. This model system gives information that may be useful in future studies on LHCII and provides a building block for further research within the hydration shell of a protein. This could also be expanded by comparing the hydration shell of a protein to the activity near the surface of a membrane-bound protein.

APPENDIX

APPENDIX

The figures presented in Appendix A are a supplement to Chapter 2. Each figure is presented in the manner shown in Figure 2.5a representing data obtained under the solution conditions listed. Each point represents the 0–0 peak of the fluorescence spectrum obtained at 2,000–10,000 cm^{-1} above the 0–0 absorbance peak, (ν_{IVE}). Each plot represents the evolution of the continuous wave fluorescence spectrum as a function of ν_{IVE}, which has been referred to as an IVE profile. The data points of each plot are described by four transitions. Transitions I, II, and III are models described by Equation 2.3. Transition IV is represented by a smoothing spline. For simplicity, Figures 2.5 and 2.10 show a comparison of the transitions without the corresponding data points. Figures A1-A11 include all temperatures studied and have the same range to allow comparison between plots. Figures A12-A21 include all Gdm^+ concentrations studied. While the range shown for the Gdm^+ plots is different than that of the temperature plots, it is consistent for all ten Gdm^+ figures.

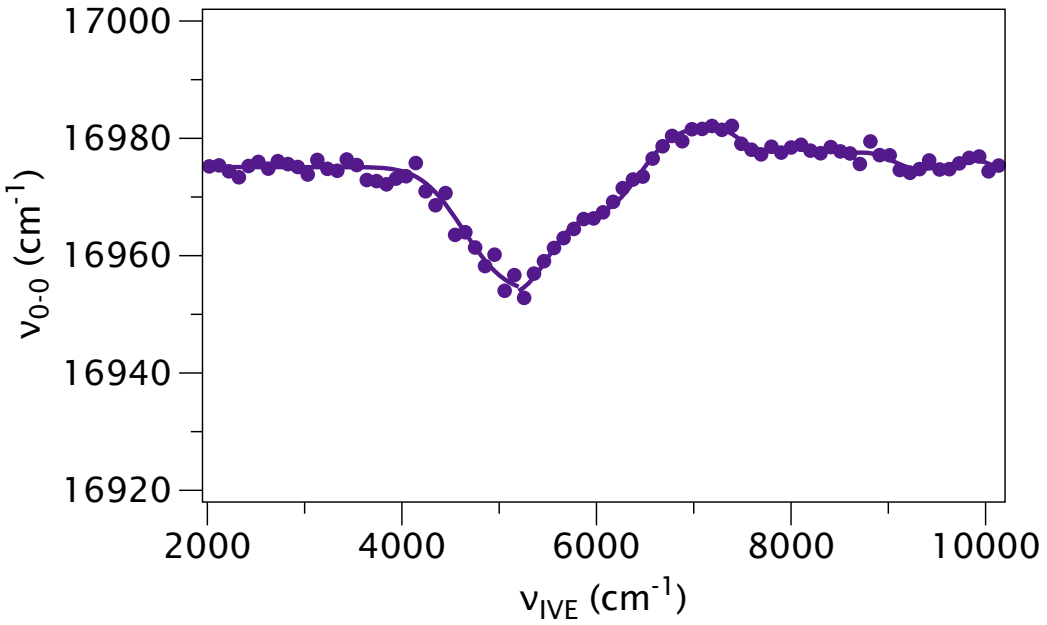

Figure A1. IVE profile of ZnCytc at 5 °C: Evolution of the wavenumber of the peak dipole strength in the 0–0 peak of the continuous-wave fluorescence spectrum from ZnCytc at 5 °C as a function of ν_{IVE}, the excitation energy above the wavenumber of the 0–0 absorption peak.

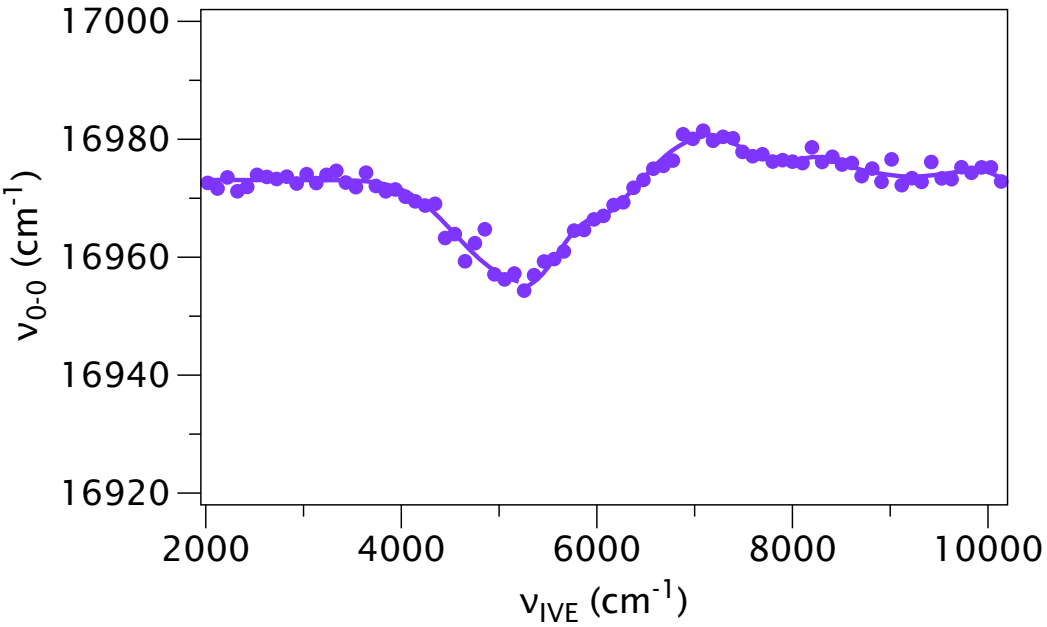

Figure A2. IVE profile of ZnCytc at 10 °C: Evolution of the wavenumber of the peak dipole strength in the 0–0 peak of the continuous-wave fluorescence spectrum from ZnCytc at 10 °C as a function of ν_{IVE}, the excitation energy above the wavenumber of the 0–0 absorption peak.

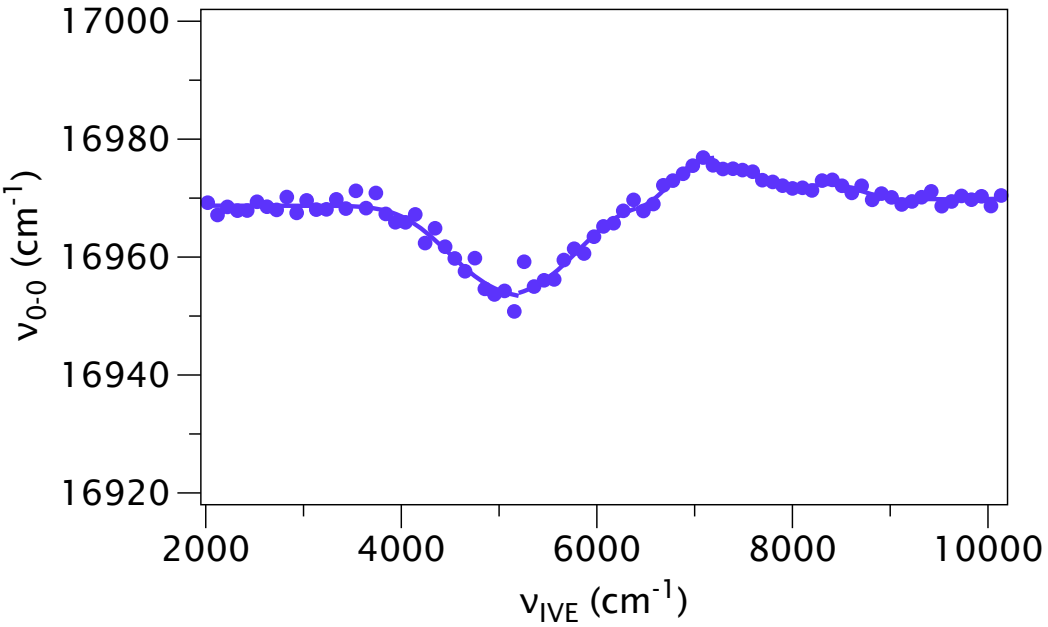

Figure A3. IVE profile of ZnCytc at 20 °C: Evolution of the wavenumber of the peak dipole strength in the 0–0 peak of the continuous-wave fluorescence spectrum from ZnCytc at 20 °C as a function of ν_{IVE}, the excitation energy above the wavenumber of the 0–0 absorption peak.

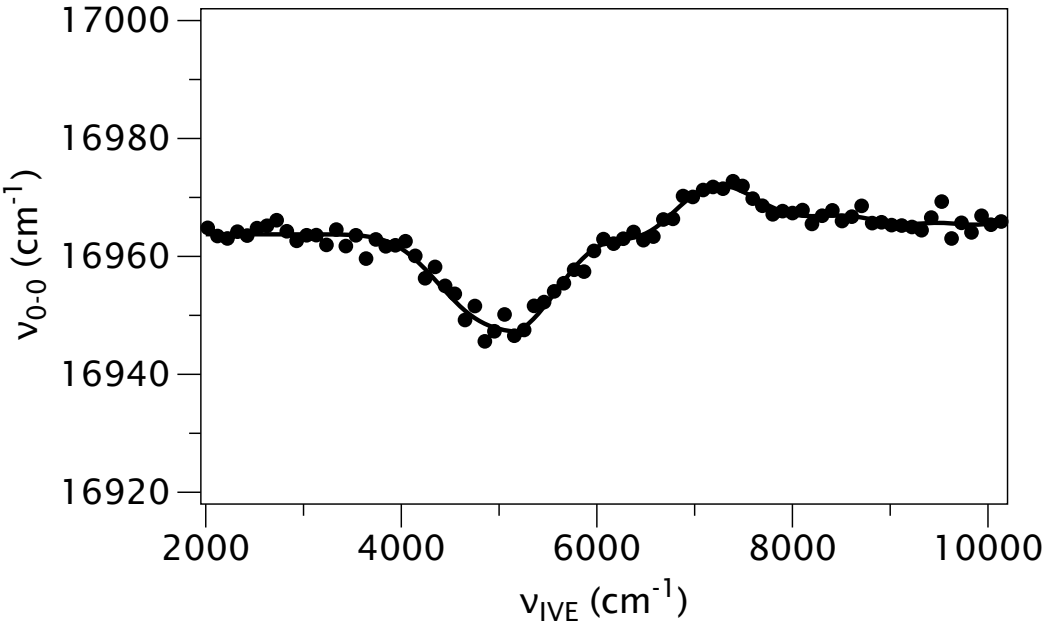

Figure A4. IVE profile of ZnCytc at 30 °C: Evolution of the wavenumber of the peak dipole strength in the 0–0 peak of the continuous-wave fluorescence spectrum from ZnCytc at 30 °C as a function of ν_{IVE}, the excitation energy above the wavenumber of the 0–0 absorption peak.

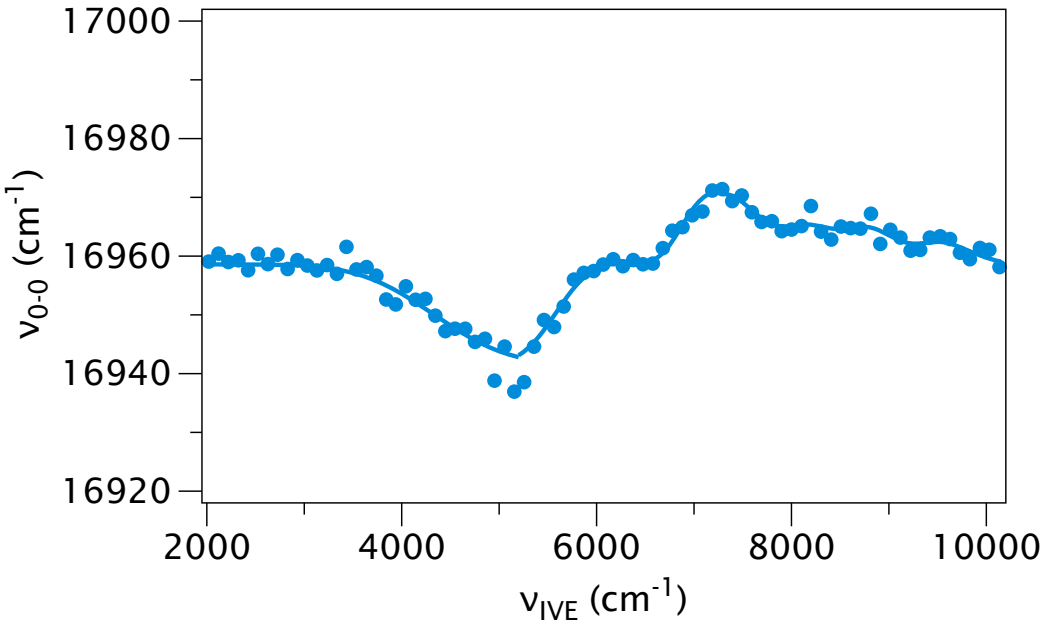

Figure A5. IVE profile of ZnCytc at 40 °C: Evolution of the wavenumber of the peak dipole strength in the 0–0 peak of the continuous-wave fluorescence spectrum from ZnCytc at 40 °C as a function of ν_{IVE}, the excitation energy above the wavenumber of the 0–0 absorption peak.

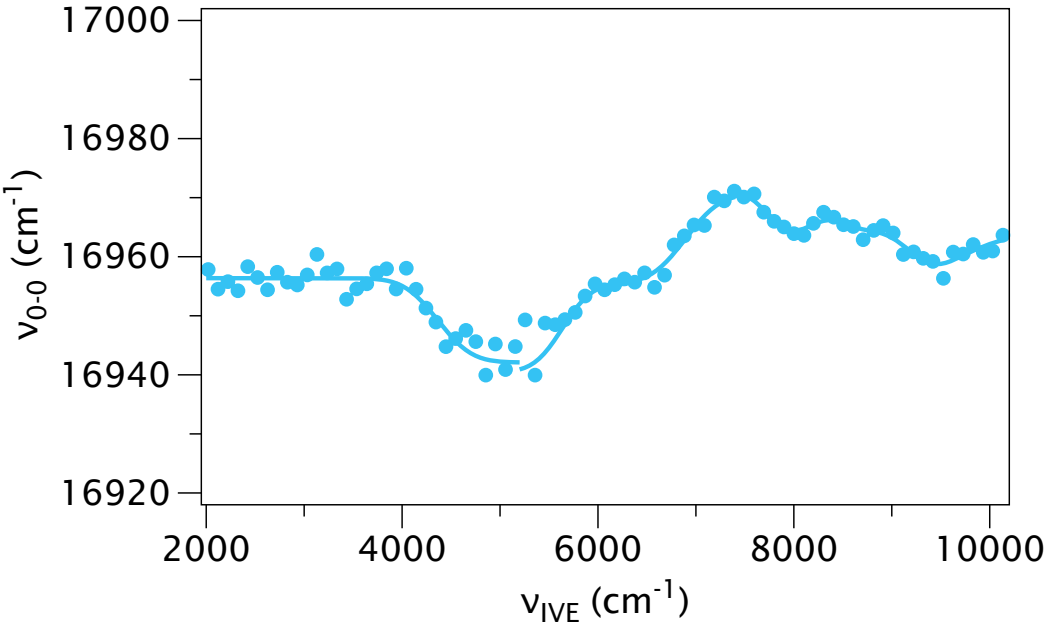

Figure A6. IVE profile of ZnCytc at 50 °C: Evolution of the wavenumber of the peak dipole strength in the 0–0 peak of the continuous-wave fluorescence spectrum from ZnCytc at 50 °C as a function of ν_{IVE}, the excitation energy above the wavenumber of the 0–0 absorption peak.

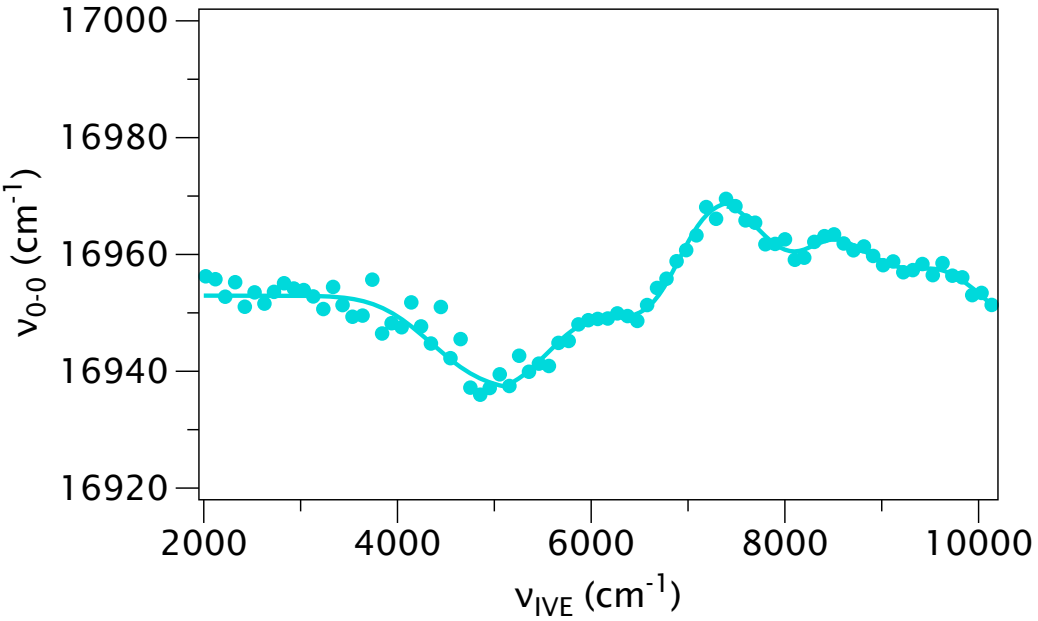

Figure A7. IVE profile of ZnCytc at 60 °C: Evolution of the wavenumber of the peak dipole strength in the 0–0 peak of the continuous-wave fluorescence spectrum from ZnCytc at 60 °C as a function of ν_{IVE}, the excitation energy above the wavenumber of the 0–0 absorption peak.

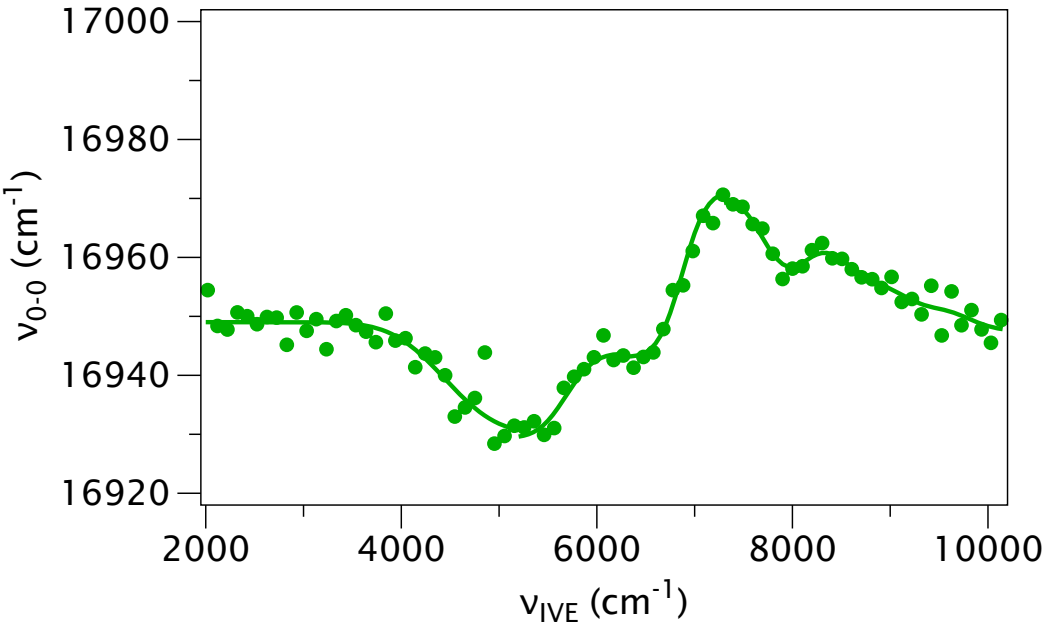

Figure A8. IVE profile of ZnCytc at 70 °C: Evolution of the wavenumber of the peak dipole strength in the 0–0 peak of the continuous-wave fluorescence spectrum from ZnCytc at 70 °C as a function of ν_{IVE}, the excitation energy above the wavenumber of the 0–0 absorption peak.

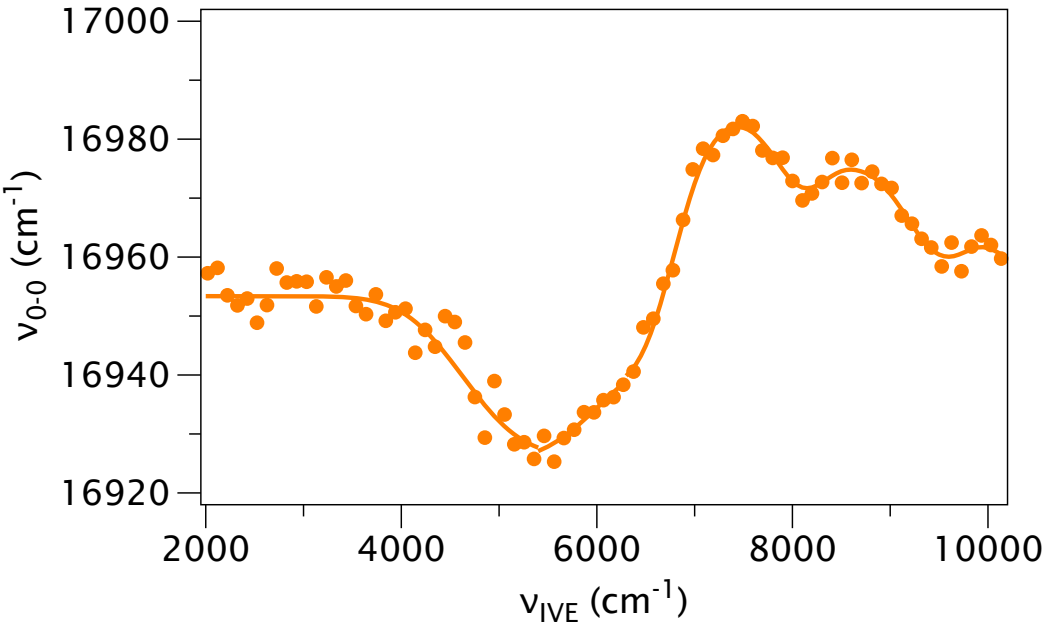

Figure A9. IVE profile of ZnCytc at 80 °C: Evolution of the wavenumber of the peak dipole strength in the 0–0 peak of the continuous-wave fluorescence spectrum from ZnCytc at 80 °C as a function of ν_{IVE}, the excitation energy above the wavenumber of the 0–0 absorption peak.

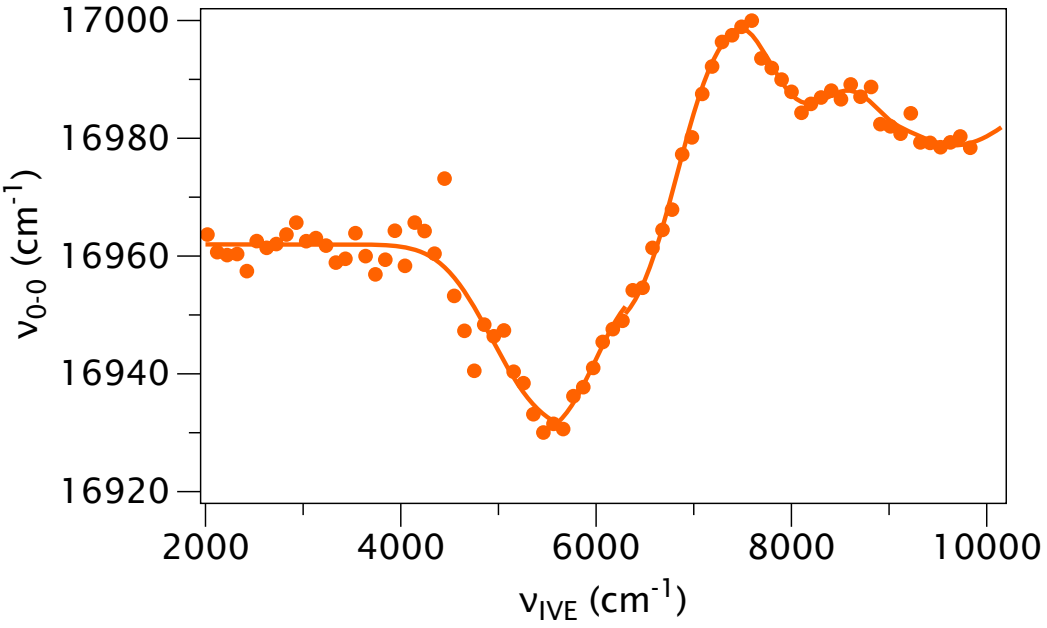

Figure A10. IVE profile of ZnCytc at 85 °C: Evolution of the wavenumber of the peak dipole strength in the 0–0 peak of the continuous-wave fluorescence spectrum from ZnCytc at 85 °C as a function of ν_{IVE}, the excitation energy above the wavenumber of the 0–0 absorption peak.

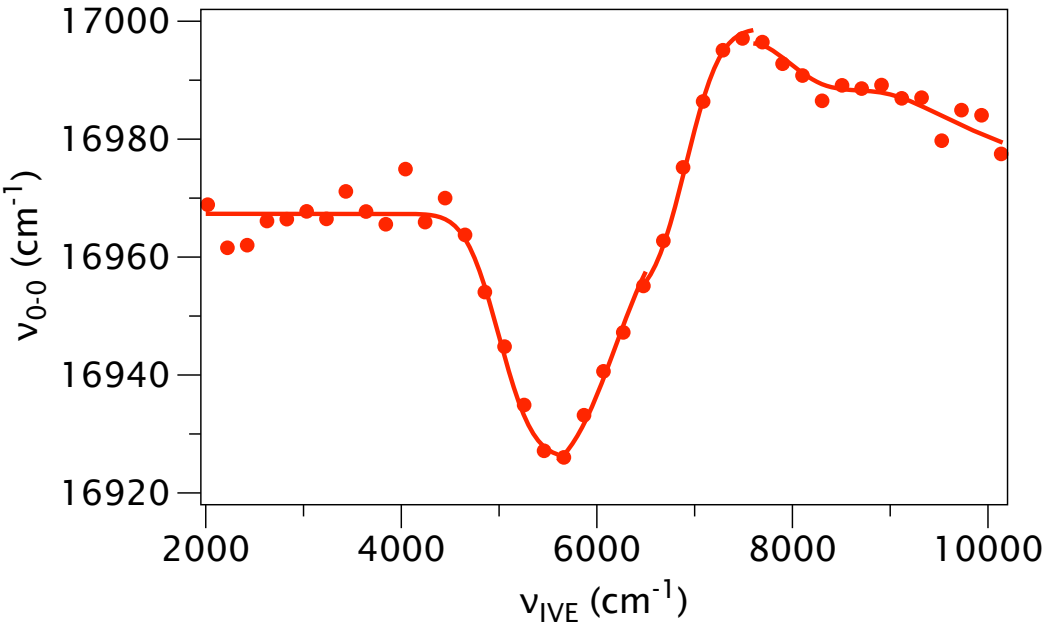

Figure A11. IVE profile of ZnCytc at 90 °C: Evolution of the wavenumber of the peak dipole strength in the 0–0 peak of the continuous-wave fluorescence spectrum from ZnCytc at 90 °C as a function of ν_{IVE}, the excitation energy above the wavenumber of the 0–0 absorption peak.

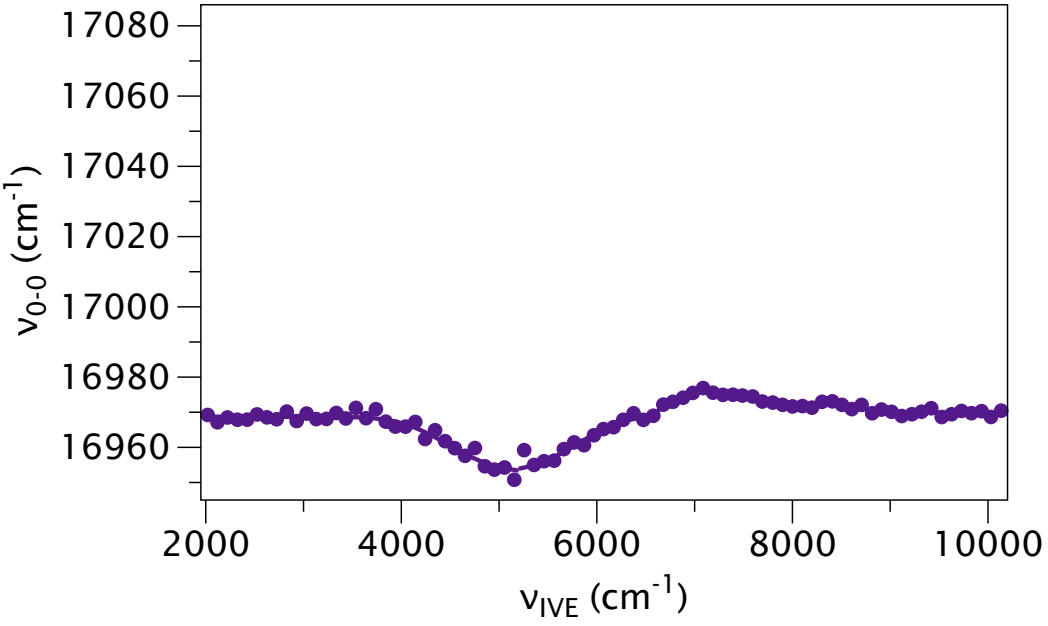

Figure A12. IVE profile of ZnCytc in the presence of 0.0 M Gdm^+: Evolution of the wavenumber of the peak dipole strength in the 0–0 peak of the continuous-wave fluorescence spectrum from ZnCytc at 20 °C as a function of ν_{IVE}, the excitation energy above the wavenumber of the 0–0 absorption peak.

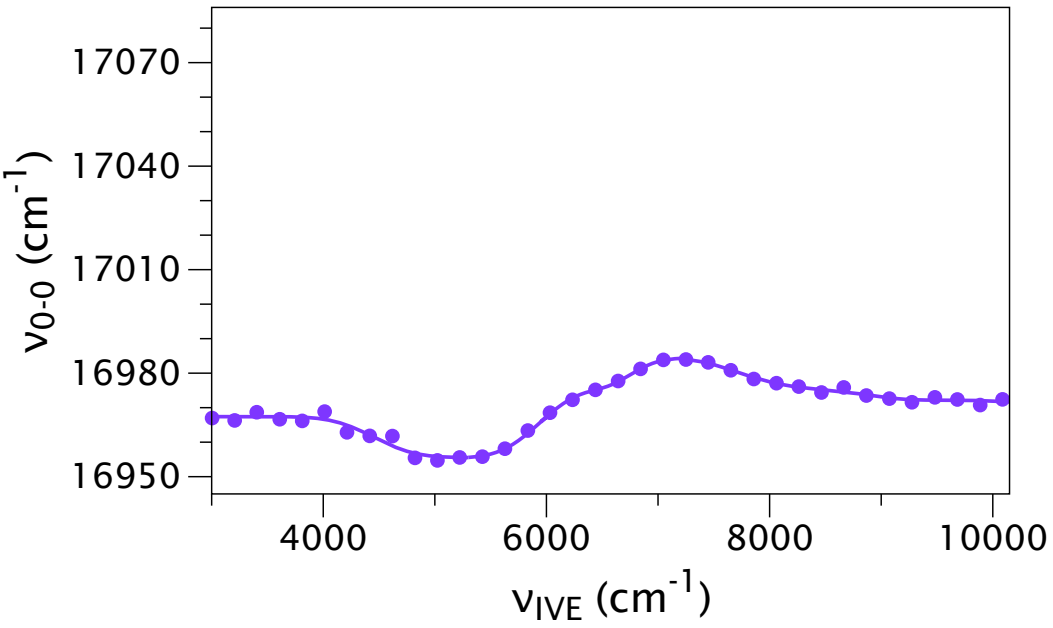

Figure A13. IVE profile of ZnCytc in the presence of 0.25 M Gdm^+: Evolution of the wavenumber of the peak dipole strength in the 0–0 peak of the continuous-wave fluorescence spectrum from ZnCytc at 20 °C as a function of ν_{IVE}, the excitation energy above the wavenumber of the 0–0 absorption peak.

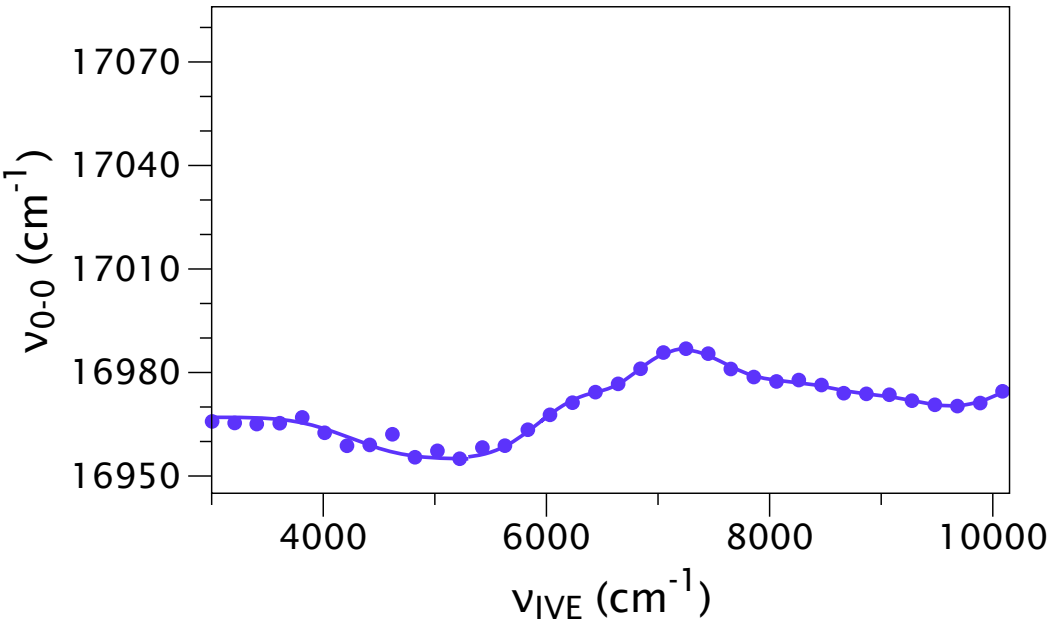

Figure A14. IVE profile of ZnCytc in the presence of 0.5 M Gdm^+: Evolution of the wavenumber of the peak dipole strength in the 0–0 peak of the continuous-wave fluorescence spectrum from ZnCytc at 20 °C as a function of ν_{IVE}, the excitation energy above the wavenumber of the 0–0 absorption peak.

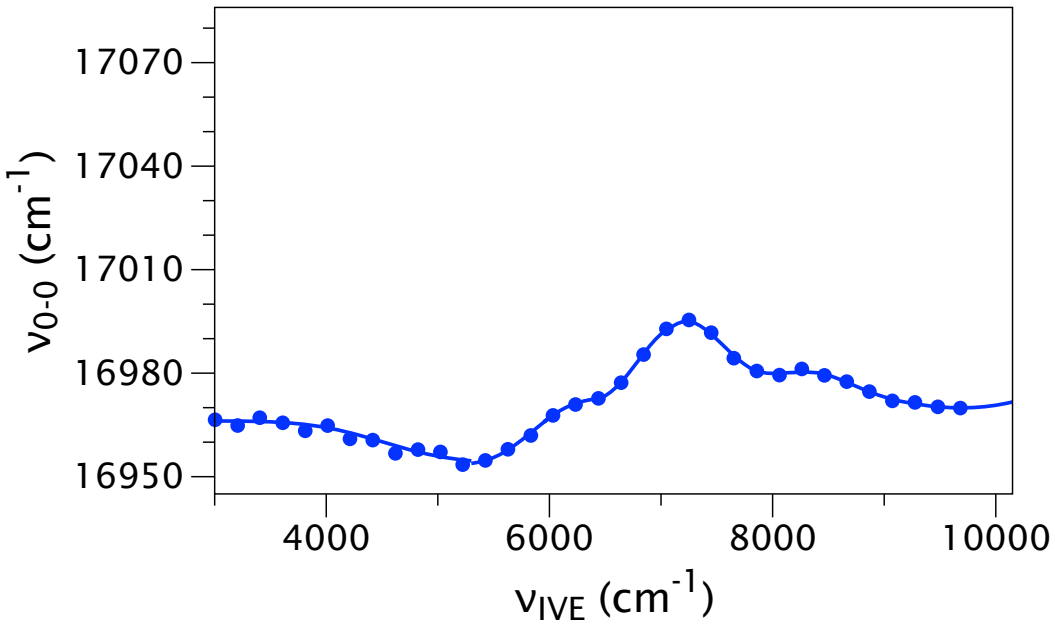

Figure A15. IVE profile of ZnCytc in the presence of 1.0 M Gdm^+: Evolution of the wavenumber of the peak dipole strength in the 0–0 peak of the continuous-wave fluorescence spectrum from ZnCytc at 20 °C as a function of ν_{IVE}, the excitation energy above the wavenumber of the 0–0 absorption peak.

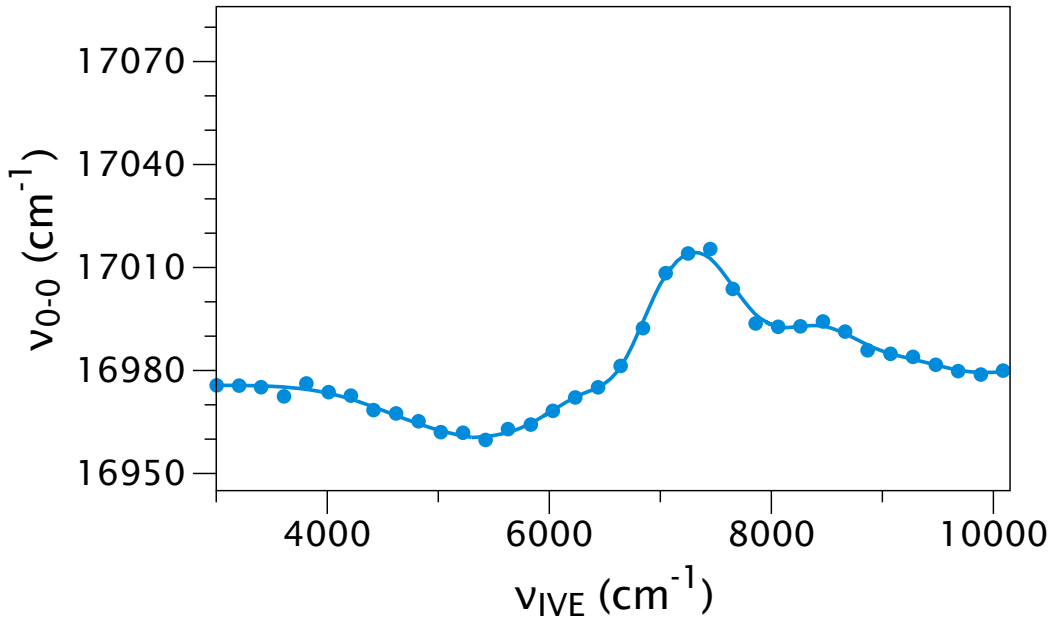

Figure A16. IVE profile of ZnCytc in the presence of 1.5 M Gdm^+: Evolution of the wavenumber of the peak dipole strength in the 0–0 peak of the continuous-wave fluorescence spectrum from ZnCytc at 20 °C as a function of ν_{IVE}, the excitation energy above the wavenumber of the 0–0 absorption peak.

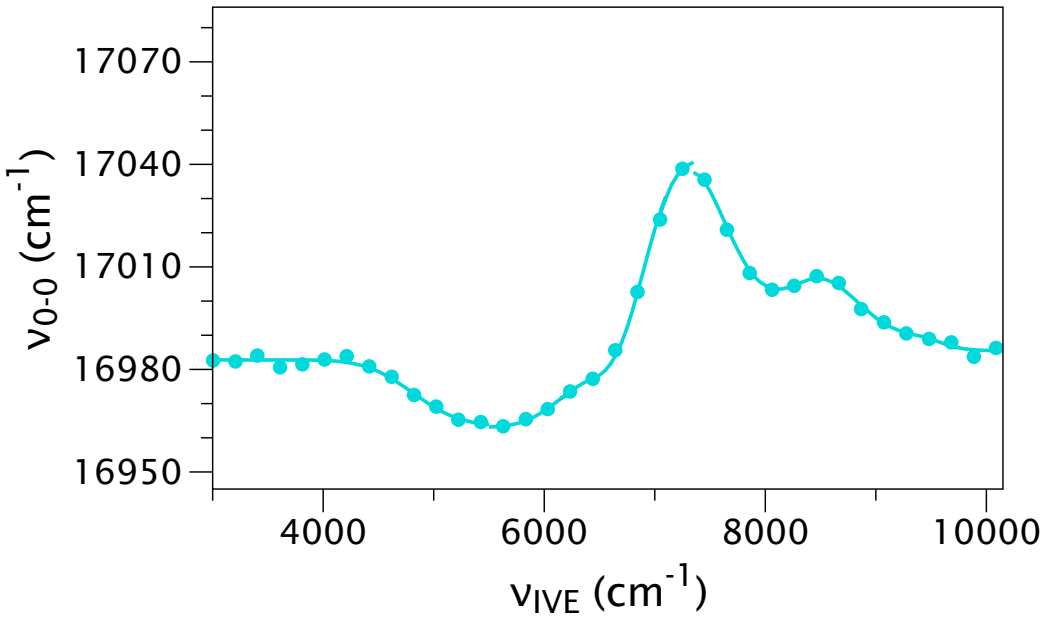

Figure A17. IVE profile of ZnCytc in the presence of 2.0 M Gdm^+: Evolution of the wavenumber of the peak dipole strength in the 0–0 peak of the continuous-wave fluorescence spectrum from ZnCytc at 20 °C as a function of ν_{IVE}, the excitation energy above the wavenumber of the 0–0 absorption peak.

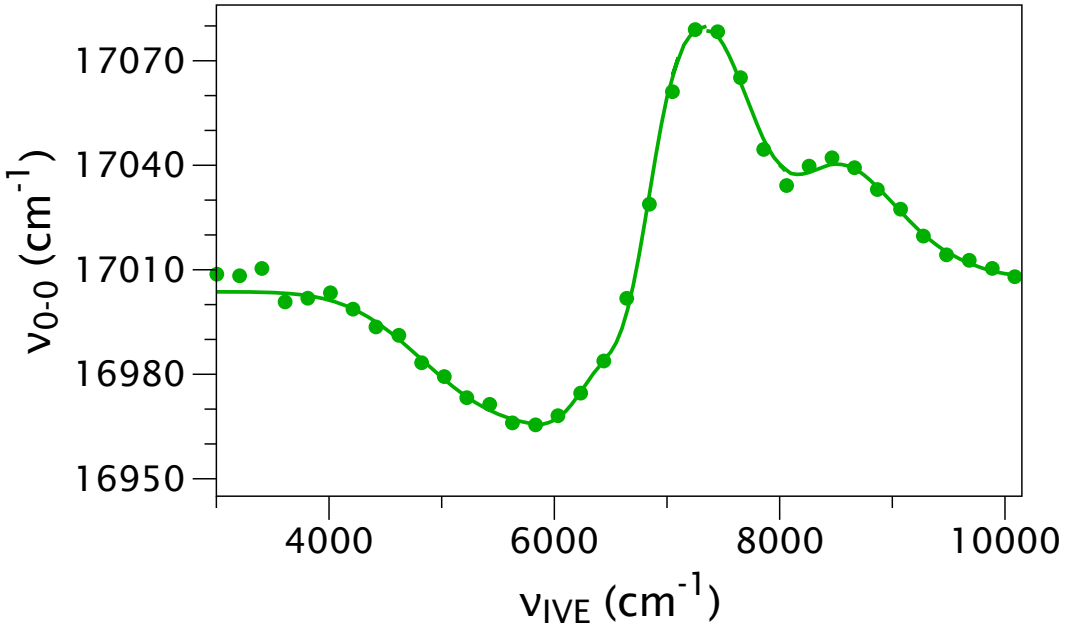

Figure A18. IVE profile of ZnCytc in the presence of 2.5 M Gdm^+: Evolution of the wavenumber of the peak dipole strength in the 0–0 peak of the continuous-wave fluorescence spectrum from ZnCytc at 20 °C as a function of ν_{IVE}, the excitation energy above the wavenumber of the 0–0 absorption peak.

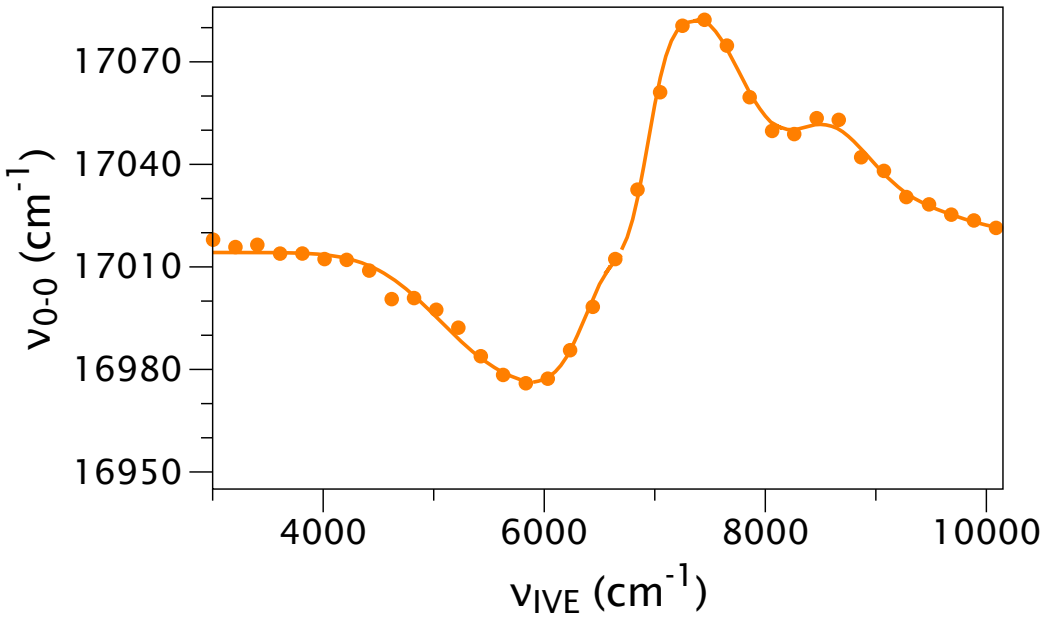

Figure A19. IVE profile of ZnCytc in the presence of 3.0 M Gdm^+: Evolution of the wavenumber of the peak dipole strength in the 0–0 peak of the continuous-wave fluorescence spectrum from ZnCytc at 20 °C as a function of ν_{IVE}, the excitation energy above the wavenumber of the 0–0 absorption peak.

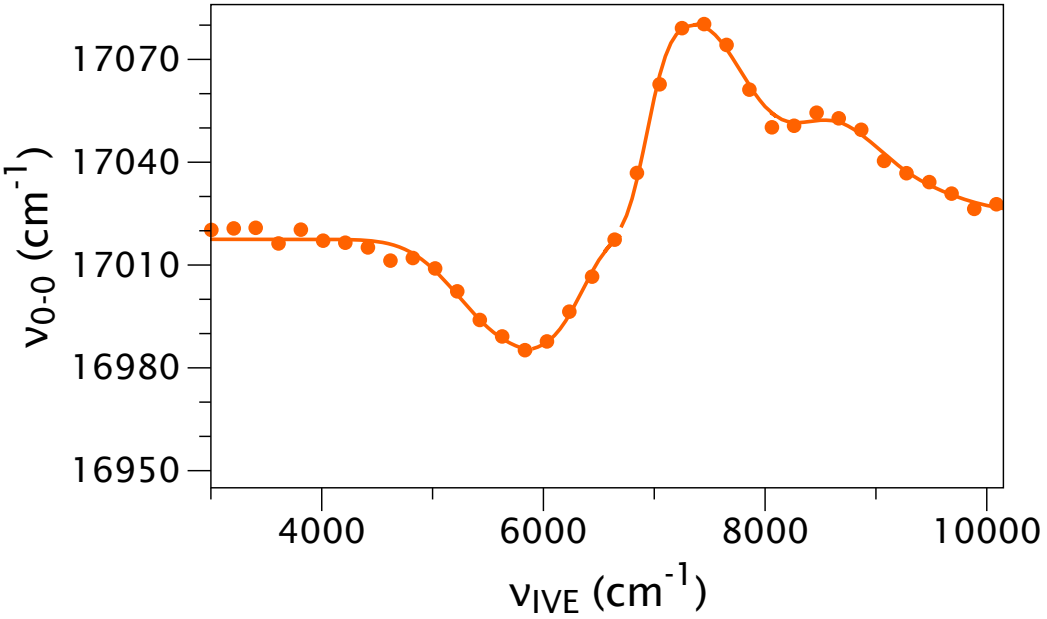

Figure A20. IVE profile of ZnCytc in the presence of 4.0 M Gdm^+: Evolution of the wavenumber of the peak dipole strength in the 0–0 peak of the continuous-wave fluorescence spectrum from ZnCytc at 20 °C as a function of ν_{IVE}, the excitation energy above the wavenumber of the 0–0 absorption peak.

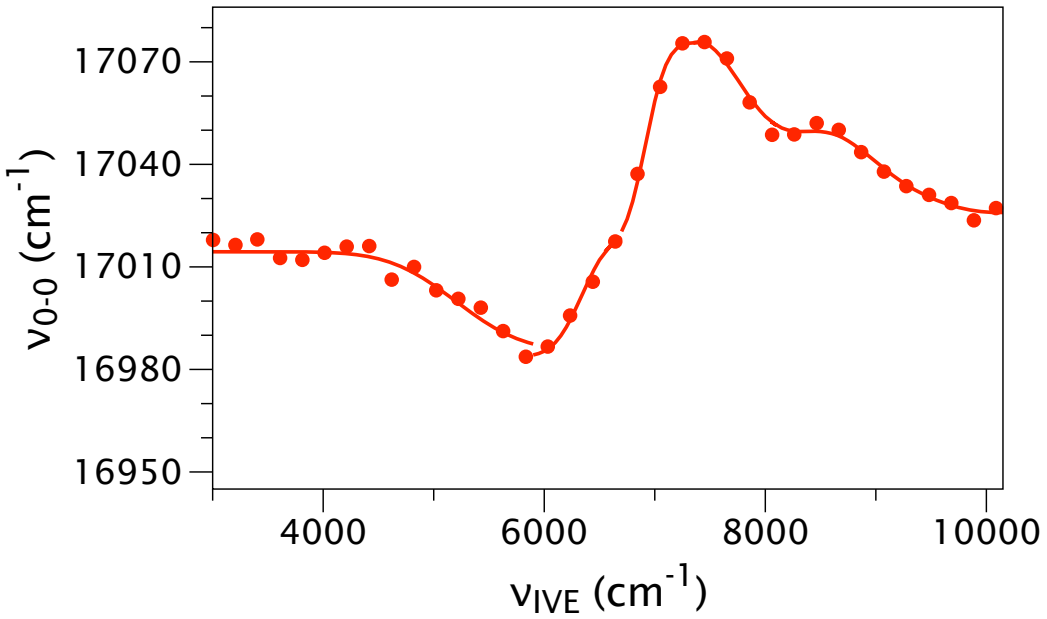

Figure A21. IVE profile of ZnCytc in the presence of 5.0 M Gdm^+: Evolution of the wavenumber of the peak dipole strength in the 0–0 peak of the continuous-wave fluorescence spectrum from ZnCytc at 20 °C as a function of ν_{IVE}, the excitation energy above the wavenumber of the 0–0 absorption peak.

LITERATURE CITED

LITERATURE CITED

(1) Frauenfelder, H.; Sligar, S. G.; Wolynes, P. G. The energy landscapes and motions of proteins. *Science* **1991**, *254*, 1598. DOI: 10.1126/science.1749933.

(2) Onuchic, J. N.; Luthey-Schulten, Z.; Wolynes, P. G. Theory of protein folding: The energy landscape perspective. *Annu. Rev. Phys. Chem.* **1997**, *48*, 545.

(3) Dill, K. A.; Chan, H. S. From Levinthal to pathways to funnels. *Nature Struct. Biol.* **1997**, *4*, 10.

(4) Chan, H. S.; Dill, K. A. Protein folding in the landscape perspective: Chevron plots and Non-Arrhenius kinetics. *Proteins: Struct. Funct. Genet.* **1998**, *30*, 2.

(5) Dill, K. A. Polymer principles and protein folding. *Protein Sci.* **1999**, *8*, 1166. DOI: 10.1110/ps.8.6.1166.

(6) Bashkin, J. S.; McLendon, G.; Mukamel, S.; Marohn, J. Influence of medium dynamics on solvation and charge separation reactions: comparison of a simple alcohol and a protein "solvent". *J. Phys. Chem.* **1990**, *94*, 4757. DOI: 10.1021/j100375a001.

(7) Riter, R. E.; Edington, M. D.; Beck, W. F. Protein-matrix solvation dynamics in the α subunit of *C*-phycocyanin. *J. Phys. Chem.* **1996**, *100*, 14198. DOI: 10.1021/jp960453j.

(8) Vanderkooi, J. M. The protein state of matter. *Biochim. Biophys. Acta* **1998**, *1386*, 241.

(9) Tripathy, J.; Beck, W. F. Nanosecond-regime correlation timescales for equilibrium protein structural fluctuations of metal-free cytochrome *c* from picosecond time-resolved fluorescence spectroscopy and the dynamic Stokes shift. *J. Phys. Chem. B* **2010**, *114*, 15958. DOI: 10.1021/jp1044964.

(10) Lampa-Pastirk, S.; Lafuente, R. C.; Beck, W. F. Excited-state axial-ligand photodissociation and nonpolar protein-matrix reorganization in Zn(II)-substituted cytochrome *c*. *J. Phys. Chem. B* **2004**, *108*, 12602. DOI: 10.1021/jp049587k.

(11) Bushnell, G. W.; Louie, G. V.; Brayer, G. D. High-resolution three-dimensional structure of horse heart cytochrome *c*. *J. Mol. Biol.* **1990**, *214*, 585. DOI: 10.1016/0022-2836(90)90200-6.

(12) Maroncelli, M.; Kumar, P. V.; Papazyan, A.; Horng, M. L.; Rosenthal, S. J.; Fleming, G. R. Studies of the inertial component of polar solvation dynamics. In *Ultrafast Reaction Dynamics and Solvent Effects*; Guaduel, Y., Rossky, P. J., Eds.; AIP Press: Woodbury, NY, 1994, p 310.

(13) Maroncelli, M. The dynamics of solvation in polar solvents. *J. Mol. Liq.* **1993**, *57*, 1. DOI: 10.1016/0167-7322(93)80045-W.

(14) Stratt, R. M.; Maroncelli, M. Nonreactive dynamics in solution: the emerging molecular view of solvation dynamics and vibrational relaxation. *J. Phys. Chem.* **1996**, *100*, 12981. DOI: 10.1021/jp9608483.

(15) Fleming, G. R.; Cho, M. Chromophore-solvent dynamics. *Annu. Rev. Phys. Chem.* **1996**, *47*, 109. DOI: 10.1146/annurev.physchem.47.1.109.

(16) Cho, B. M.; Carlsson, F.; Jimenez, R. Photon echo spectroscopy of porphyrins and heme proteins: effects of quasidegenerate electronic structure on the peak shift decay. *J. Chem. Phys.* **2006**, *124*, 144905. DOI: 10.1063/1.2186318.

(17) Maroncelli, M.; Fleming, G. R. Picosecond solvation dynamics of coumarin 153: the importance of molecular aspects of solvation. *J. Chem. Phys.* **1987**, *86*, 6221. DOI: 10.1063/1.452460.

(18) Barthel, E. R.; Martini, I. B.; Schwartz, B. J. How does the solvent control electron transfer? Experimental and theoretical studies of the simplest charge transfer reaction. *J. Phys. Chem. B* **2001**, *105*, 12230. DOI: 10.1021/jp011150e.

(19) Nilsson, L.; Halle, B. Molecular origin of time-dependent fluorescence shifts in proteins. *Proc. Natl. Acad. Sci. U.S.A.* **2005**, *102*, 13867. DOI: 10.1073/pnas.0504181102.

(20) Lampa-Pastirk, S.; Beck, W. F. Intramolecular vibrational preparation of the unfolding transition state of Zn^{II}-substituted cytochrome *c*. *J. Phys. Chem. B* **2006**, *110*, 22971. DOI: 10.1021/jp0654359.

(21) Miller, R. J. D. Vibrational energy relaxation and structural dynamics of heme proteins. *Annu. Rev. Phys. Chem.* **1991**, *42*, 581.

(22) Owrutsky, J. C.; Raftery, D.; Hochstrasser, R. M. Vibrational relaxation dynamics in solution. *Annu. Rev. Phys. Chem.* **1994**, *45*, 519.

(23) Lazaridis, T.; Karplus, M. "New view" of protein folding reconciled with the old through multiple unfolding simulations. *Science* **1997**, *278*, 1928.

(24) Leopold, P. E.; Montal, M.; Onuchic, J. N. Protein folding funnels: a kinetic approach to the sequence-structure relationship. *Proc. Natl. Acad. Sci. U.S.A.* **1992**, *89*, 8721. DOI: 10.1073/pnas.89.18.8721.

(25) Barns, K. J.; Lampa-Pastirk, S.; Dillman, K. L.; Beck, W. F. Intramolecular vibrational excitation of unfolding reactions in Zn^{II}-substituted and metal-free cytochromes *c*: activation enthalpies from integrated fluorescence Stokes shift and lineshape excitation profiles. *J. Phys. Chem. B* **2008**, *112*, 15108. DOI: 10.1021/jp803756n.

(26) Bolton, J. R.; Hall, D. O. Photochemical conversion and storage of solar energy. *Annu. Rev. Energy* **1979**, *4*, 353.

(27) van Grondelle, R.; Dekker, J. P.; Gillbro, T.; Sundström, V. Energy transfer and trapping in photosynthesis. *Biochim. Biophys. Acta* **1994**, *1187*, 1. DOI: 10.1016/0005-2728(94)90166-X.

(28) Knox, R. S. Excitation energy transfer and migration: theoretical aspects. In *Bioenergetics in Photosynthesis*; Govindjee, G., Ed.; Academic Press: New York, 1975, p 183.

(29) Sundström, V.; van Grondelle, R. Energy transfer in photosynthetic light-harvesting antennas. *J. Opt. Soc. Am. B* **1990**, *7*, 1595.

(30) Stenberg-Yfrach, G.; Rigaud, J.-L.; Durantini, E. N.; Moore, A. L.; Gust, D.; Moore, T. A. Light-driven production of ATP catalysed by F0F1-ATP synthase in an artificial photosynthetic membrane. *Nature* **1998**, *392*, 479.

(31) Krauss, N.; Hinrichs, W.; Witt, I.; Fromme, P.; Pritzkow, W.; Dauter, Z.; Betzel, C.; Wilson, K. S.; Witt, H. T.; Saenger, W. Three-dimensional structure of system I of photosynthesis at 6 Å resolution. *Nature* **1993**, *361*, 326.

(32) Deisenhofer, J.; Epp, O.; Miki, K.; Huber, R.; Michel, H. X-ray structure analysis of a membrane protein complex: electron density map at 3 Å resolution and a model of the chromophores of the photosynthetic reaction center from Rhodopseudomonas viridis. *J. Mol. Biol.* **1984**, *180*, 385. DOI: 10.1016/S0022-2836(84)80011-X.

(33) Zuber, H. Structure and function of light-harvesting complexes and their polypeptides. *Photochemistry and Photobiology* **1985**, *42*, 821.

(34) Deisenhofer, J.; Michel, H. The photosynthetic reaction center from the purple bacterium *Rhodopseudomonas viridis*. *Science* **1989**, *245*, 1463. DOI: 10.1126/science.245.4925.1463.

(35) Feher, G.; Allen, J. P.; Okamura, M. Y.; Rees, D. C. Structure and function of bacterial photosynthetic reaction centers. *Nature* **1989**, *339*, 111.

(36) Schiffer, M.; Norris, J. R. Structure and function of the photosynthetic reaction center of Rhodobacter sphaeroides. In *The Photosynthetic Reaction Center*; Deisenhofer, J., Norris, J. R., Eds.; Academic Press, Inc.: San Diego, 1993; Vol. I, p 1.

(37) Rhee, K.-H.; Morris, E. P.; Barber, J.; Kühlbrandt, W. Three-dimensional structure of the plant photosystem II reaction centre at 8 Å resolution. *Nature* **1998**, *396*, 283.

(38) Zouni, A.; Witt, H.-T.; Kern, J.; Fromme, P.; Krauß, N.; Saenger, W.; Orth, P. Crystal structure of photosystem II from *Synechococcus elongatus* at 3.8 Å resolution. *Nature* **2001**, *409*, 739.

(39) Jordan, P.; Fromme, P.; Witt, H. T.; Klukas, O.; Saenger, W.; Krauß, N. Three-dimensional structure of cyanobacterial photosystem I at 2.5 Å resolution. *Nature* **2001**, *411*, 909.

(40) van Amerongen, H.; Dekker, J. P. Light-harvesting in photosystem II. In *Light-Harvesting Antennas in Photosynthesis*; Green, B. R., Parson, W. W., Eds.; Kluwer Academic Publishers: Dordrecht, 2003, p 219.

(41) Standfuss, J.; Terwisscha van Scheltinga, A. C.; Lamborghini, M.; Kühlbrandt, W. Mechanisms of photoprotection and nonphotochemical quenching in pea light-

harvesting complex at 2.5 Å resolution. *EMBO J.* **2005**, *24*, 919. DOI: 10.1038/sj.emboj.7600585.

(42) Book, L. D.; Ostafin, A. E.; Ponomarenki, N.; Norris, J. R.; Scherer, N. F. Exciton delocalization and initial dephasing dynamics of purple bacterial LH2. *J. Phys. Chem. B* **2000**, *104*, 8295.

(43) van Amerongen, H.; van Grondelle, R. Understanding the energy transfer function of LHCII, the major light-harvesting complex of green plants. *J. Phys. Chem. B* **2001**, *105*, 604. DOI: 10.1021/jp0028406.

(44) Förster, T. Intermolecular energy transfer and fluorescence. *Annu. Phys.* **1968**, *2*, 55.

(45) Horton, P.; Ruban, A. Molecular design of the photosystem II light-harvesting antenna: photosynthesis and photoprotection. *J. Exp. Bot.* **2005**, *56*, 365. DOI: 10.1093/jxb/eri023.

(46) Sundström, V. Photosynthetic light harvesting, charge separation, and photoprotection: the primary steps. In *Photobiology: The Science of Life and Light*; Second Edition ed.; Björn, L. O., Ed.; Springer: New York, 2007, p 289.

(47) Johnson, M. P.; Ruban, A. V. Photoprotective energy dissipation in higher plants involves alteration of the excited state energy of the emitting chlorophyll(s) in the light harvesting antenna II (LHCII). *J Biol Chem* **2009**, *284*, 23592. DOI: 10.1074/jbc.M109.013557.

(48) Lampa-Pastirk, S.; Beck, W. F. Polar solvation dynamics in Zn(II)-substituted cytochrome *c*: diffusive sampling of the energy landscape in the hydrophobic core and solvent-contact layer. *J. Phys. Chem. B* **2004**, *108*, 16288. DOI: 10.1021/jp0488113.

(49) Stratt, R. M. The instantaneous normal modes of liquids. *Acc. Chem. Res.* **1995**, *28*, 201. DOI: 10.1021/ar00053a001.

(50) Vanderkooi, J. M.; Adar, F.; Ericińska, M. Metallocytochromes *c*: characterization of electronic absorption and emission spectra of Sn^{4+} and Zn^{2+} cytochromes *c*. *Eur. J. Biochem.* **1976**, *64*, 381. DOI: 10.1111/j.1432-1033.1976.tb10312.x.

(51) Ruban, A. V.; Horton, P. Mechanism of ΔpH-dependent dissipation of absorbed excitation energy by photosynthetic membranes. I. Spectroscopic analysis of isolated light-harvesting complexes. *Biochim. Biophys. Acta* **1992**, *1102*, 30.

(52) Bryngelson, J. D.; Wolynes, P. G. Spin glasses and the statistical mechanics of protein folding. *Proc. Natl. Acad. Sci. U.S.A.* **1987**, *84*, 7524. DOI: 10.1073/pnas.84.21.7524.

(53) Zwanzig, R. Diffusion in a rough potential. *Proc. Natl. Acad. Sci. U.S.A.* **1988**, *85*, 2029. DOI: 10.1073/pnas.85.7.2029.

(54) Ansari, A.; Berendzen, J.; Bowne, S. F.; Frauenfelder, H.; Iben, I. E.; Sauke, T. B.; Shyamsunder, E.; Young, R. D. Protein states and proteinquakes. *Proc. Natl. Acad. Sci. U.S.A.* **1985**, *82*, 5000. DOI: 10.1073/pnas.82.15.5000.

(55) Sali, A.; Shakhnovich, E.; Karplus, M. How does a protein fold? *Nature* **1994**, *369*, 248.

(56) Shea, J.-E.; Brooks III, C. L. From folding theories to folding proteins: a review and assessment of simulation studies of protein folding and unfolding. *Annu. Rev. Phys. Chem.* **2001**, *52*, 499.

(57) Bai, Y.; Sosnice, T. R.; Mayne, L.; Englander, S. W. Protein folding intermediates: native-state hydrogen exchange. *Science* **1995**, *269*, 192. DOI: 10.1126/science.7618079.

(58) Anni, H.; Vanderkooi, J. M.; Mayne, L. Structure of zinc-substituted cytochrome *c*: nuclear magnetic resonance and optical spectroscopic studies. *Biochemistry* **1995**, *34*, 5744. DOI: 10.1021/bi00017a006.

(59) Qian, C.; Yao, Y.; Tong, Y.; Wang, J.; Tang, W. Structural analysis of zinc-substituted cytochrome *c*. *J. Biol. Inorg. Chem.* **2003**, *8*, 394. DOI: 10.1007/s00775-002-0428-1.

(60) Elias, H.; Chou, M. H.; Winkler, J. R. Electron-transfer kinetics of Zn-substituted cytochrome *c* and its $Ru(NH_3)_5$(Histidine-33) derivative. *J. Am. Chem. Soc.* **1988**, *110*, 429. DOI: 10.1021/ja00210a019.

(61) Ye, S.; Shen, C.; Cotton, T. M.; Kostić, N. M. Characterization of zinc-substituted cytochrome *c* by circular dichroism and resonance Raman spectroscopic methods. *J. Inorg. Biochem.* **1997**, *65*, 219. DOI: 10.1016/S0162-0134(97)00001-9.

(62) Gouterman, M. Optical spectra and electronic structure of porphyrins and related rings. In *The Porphyrins*; Dolphin, D., Ed.; Academic Press: New York, 1978; Vol. 3, p 1.

(63) Miller, J. R.; Dorough, G. D. Pyridinate complexes of some metallo-derivatives of tetraphenylporphine and tetraphenylchlorin. *J. Am. Chem. Soc.* **1952**, *74*, 3977.

(64) Nappa, M.; Valentine, J. S. The influence of axial ligands on metalloporphyrin visible absorption spectra. Complexes of tetraphenylporphinatozinc. *J. Am. Chem. Soc.* **1978**, *100*, 5075. DOI: 10.1021/ja00484a027.

(65) Humphry-Baker, R.; Kalyanasundaram, K. Influence of axial ligation on the fluorescence of tetrakisphenylporphyrins. *J. Photochem.* **1985**, *31*, 105. DOI: 10.1016/0047-2670(85)85078-4.

(66) Kadish, K. M.; Shiue, L. R. Reactions of metalloporphyrin π radicals. 3. Solvent- and ligand-binding effects on the one-electron oxidation of 5,10,15,20-tetraphenylporphyrin d10 metal ions in nonaqueous media. *Inorg. Chem.* **1982**, *21*, 3623.

(67) Vogel, G. C.; Beckmann, B. A. Binding of pyridine to phenyl-substituted derivatives of zinc tetraphenylporphine. *Inorg. Chem.* **1976**, *15*, 483. DOI: 10.1021/ic50156a054.

(68) Scheidt, R. W. Porphyrin stereochemistry. In *The Porphyrins*; Dolphin, D., Ed.; Academic Press: New York, 1978; Vol. 3, p 463.

(69) Fleischer, E. B.; Miller, C. K.; Webb, L. E. Crystal and molecular structures of some metal tetraphenylporphines. *J. Am. Chem. Soc.* **1964**, *86*, 2342. DOI: 10.1021/ja01066a009.

(70) Schauer, C. K.; Anderson, O. P.; Eaton, S. S.; Eaton, G. R. Crystal and molecular structure of a six-coordinate zinc porphyrin: bis(tetrahydrofuran)(5,10,15,20-tetraphenylporphinato)zinc(II). *Inorg. Chem.* **1985**, *24*, 4082. DOI: 10.1021/ic00218a024.

(71) Scheidt, R. W.; Eigenbrot, C. W.; Ogiso, M.; Hatano, K. Stereochemistry of a porphyrin atropisomer. The molecular and crystal structure of six-coordinate [5*α*, 10*β*-bis(*o*-nicotinamidophenyl)-15,20-diphenylporphinato]zinc(II). *Bull. Chem. Soc. Jpn.* **1987**, *60*, 3529. DOI: 10.1246/bcsj.60.3529.

(72) Tezcan, A. F.; Findley, W. M.; Crane, B. R.; Ross, S. A.; Lyubovitsky, J. G.; Gray, H. B.; Winkler, J. R. Using deeply trapped intermediates to map the cytochrome c folding landscape. *Proc. Natl. Acad. Sci. U.S.A.* **2002**, *99*, 8626. DOI: 10.1073/pnas.132254499.

(73) Lesch, H.; Stadlbauer, H.; Friedrich, J.; Vanderkooi, J. M. Stability diagram and unfolding of a modified cytochrome c: what happens in the transformation regime? *Biophys. J.* **2002**, *82*, 1644. DOI: 10.1016/S0006-3495(02)75515-X.

(74) McQuarrie, D. A. *Statistical Mechanics*; HarperCollins Publishers: New York, 1976.

(75) Gómez, J.; Hilser, V. J.; Xie, D.; Freire, E. The heat capacity of proteins. *Proteins Struct. Funct. Genetics* **1995**, *22*, 404.

(76) Krishna, M. M. G.; Lin, Y.; Rumbley, J. N.; Englander, S. W. Cooperative omega loops in cytochrome *c*: Role in folding and function. *J. Mol. Biol.* **2003**, *331*, 29. DOI: 10.1016/S0022-2836(03)00697-1.

(77) Maity, H.; Maity, M.; Englander, S. W. How cytochrome *c* folds, and why: submolecular foldon units and their stepwise sequential stabilization. *J. Mol. Biol.* **2004**, *343*, 223. DOI: 10.1016/j.jmb.2004.08.005.

(78) Maity, H.; Maity, M.; Krishna, M. M. G.; Mayne, L.; Englander, S. W. Protein folding: the stepwise assembly of foldon units. *Proc. Natl. Acad. Sci. U.S.A.* **2005**, *102*, 4741. DOI: 10.1073/pnas.0501043102.

(79) Berg, M. Viscoelastic continuum model of nonpolar solvation. 1. Implications for multiple time scales in liquid dynamics. *J. Phys. Chem. A* **1998**, *102*, 17. DOI: 10.1021/jp9722061.

(80) Nandi, N.; Bagchi, B. Dielectric relaxation of biological water. *J. Phys. Chem. B* **1997**, *101*, 10954. DOI: 10.1021/jp971879g.

(81) Pal, S. K.; Peon, J.; Zewail, A. H. Biological water at the protein surface: dynamical solvation probed directly with femtosecond resolution. *Proc. Natl. Acad. Sci. U.S.A.* **2002**, *99*, 1763. DOI: 10.1073/pnas.042697899.

(82) Pal, S. K.; Peon, J.; Bagchi, B.; Zewail, A. H. Biological water: femtosecond dynamics of macromolecular hydration. *J. Phys. Chem. B* **2002**, *106*, 12376. DOI: 10.1021/jp0213506.

(83) Bagchi, B. Water dynamics in the hydration layer around proteins and micelles. *Chem. Rev.* **2003**, *105*, 3197. DOI: 10.1021/cr020661+.

(84) Kauzmann, W. Some factors in the interpretation of protein denaturation. *Adv. Protein Chem.* **1959**, *14*, 1.

(85) Kuntz, I. D., Jr.; Kauzmann, W. Hydration of proteins and polypeptides. *Adv. Protein Chem.* **1974**, *28*, 239. DOI: 10.1016/S0065-3233(08)60232-6.

(86) Makhatadze, G. I.; Privalov, P. L. Contribution of hydration to protein folding thermodynamics I. The enthalpy of hydration. *J. Mol. Biol.* **1993**, *232*, 639. DOI: 10.1006/jmbi.1993.1416.

(87) Honig, B.; Yang, A.-S. Free energy balance in protein folding. *Adv. Protein Chem.* **1995**, *46*, 27. DOI: 10.1016/S0065-3233(08)60331-9.

(88) Matyushov, D. V. Nanosecond Stokes shift dynamics, dynamical transition, and gigantic reorganization energy of hydrated heme proteins. *J. Phys. Chem. B* **2011**, *115*, 10715. DOI: 10.1021/jp200409z.

(89) Pal, S. K.; Zewail, A. H. Dynamics of water in biological recognition. *Chem. Rev.* **2004**, *104*, 2099. DOI: 10.1021/cr020689l.

(90) Halle, B.; Davidovic, M. Biomolecular hydration: from water dynamics to hydrodynamics. *Proc. Natl. Acad. Sci. U.S.A.* **2003**, *100*, 12135.

(91) Halle, B. Protein hydration dynamics in solution: a critical survey. *Phil. Trans. R. Soc. Lond. B* **2004**, *359*, 1207. DOI: 10.1098/rstb.2004.1499.

(92) Modig, K.; Liepinsh, E.; Otting, G.; Halle, B. Dynamics of protein and peptide hydration. *J. Am. Chem. Soc.* **2004**, *126*, 102. DOI: 10.1021/ja038325d.

(93) Ebbinghaus, S.; Kim, S. J.; Heyden, M.; Yu, X.; Heugen, U.; Gruebele, M.; Leitner, D. M.; Havenith, M. An extended dynamical hydration shell around proteins. *Proc. Natl. Acad. Sci. U.S.A.* **2007**, *104*, 20749. DOI: 10.1073/pnas.0709207104.

(94) Qiu, W.; Zhang, L.; Okobia, O.; Yang, Y.; Wang, L.; Zhong, D.; Zewail, A. H. Ultrafast solvation dynamics of human serum albumin: correlations with conformational transitions and site-selected recognition. *J. Phys. Chem. B* **2006**, *110*, 10540. DOI: 10.1021/jp055989w.

(95) Jimenez, R.; Fleming, G. R.; Kumar, P. V.; Maroncelli, M. Femtosecond solvation dynamics of water. *Nature* **1994**, *369*, 471. DOI: 10.1038/369471a0.

(96) Riter, R. E.; Willard, D. M.; Levinger, N. E. Water immobilization at surfactant interfaces in reverse micelles. *J. Phys. Chem. B* **1998**, *102*, 2705. DOI: 10.1021/jp973330n.

(97) Fayer, M. D.; Levinger, N. E. Analysis of water in confined geometries and at interfaces. *Annu. Rev. Anal. Chem.* **2010**, *3*, 89. DOI: 10.1146/annurev-anchem-070109-103410.

(98) Pierce, D. W.; Boxer, S. G. Dielectric relaxation in a protein matrix. *J. Phys. Chem.* **1992**, *96*, 5560. DOI: 10.1021/j100192a069.

(99) Pal, S. K.; Mandal, D.; Sukul, D.; Sen, S.; Bhattacharyya, K. Solvation dynamics of DCM in human serum albumin. *J. Phys. Chem. B* **2001**, *105*, 1438. DOI: 10.1021/jp002368o.

(100) Cohen, B. E.; McAnaney, T. B.; Park, E. S.; Jan, Y. N.; Boxer, S. G.; Jan, L. Y. Probing protein electrostatics with a synthetic fluorescent amino acid. *Science* **2002**, *296*, 1700. DOI: 10.1126/science.1069346.

(101) Sahu, K.; Mondal, S. K.; Ghosh, S.; Roy, D.; Bhattacharyya, K. Temperature dependence of solvation dynamics and anisotropy decay in a protein: ANS in bovine serum albumin. *J. Chem. Phys.* **2006**, *124*, 124909. DOI: 10.1063/1.2178782.

(102) Toptygin, D.; Gronenborn, A. M.; Brand, L. Nanosecond relaxation dynamics of protein GB1 identified by the time-dependent red shift in the fluorescence of tryptophan and 5-fluorotryptophan. *J. Phys. Chem. B.* **2006**, *110*, 26292. DOI: 10.1021/jp064528n.

(103) Abbyad, P.; Shi, X.; Childs, W.; McAnaney, T. B.; Cohen, B. E.; Boxer, S. G. Measurement of solvation responses at multiple sites in a globular protein. *J. Phys. Chem. B* **2007**, *111*, 8269. DOI: 10.1021/jp0709104.

(104) Halle, B.; Nilsson, L. Does the dynamic Stokes shift report on slow protein hydration dynamics? *J. Phys. Chem. B* **2009**, *113*, 8210. DOI: 10.1021/jp9027589.

(105) Fenimore, P. W.; Frauenfelder, H.; McMahon, B. H.; Young, R. D. Bulk-solvent and hydration-shell fluctuations, similar to α- and β-fluctuations in glasses, control protein motions and functions. *Proc. Natl. Acad. Sci. U.S.A.* **2004**, *101*, 14408. DOI: 10.1073/pnas.0405573101.

(106) Frauenfelder, H.; Chen, G.; Berendzen, J.; Fenimore, P. W.; Jansson, H.; McMahon, B. H.; Stroe, I. R.; Swenson, J.; Young, R. D. A unified model of protein dynamics. *Proc. Natl. Acad. Sci. U.S.A.* **2009**, *106*, 5129. DOI: 10.1073/pnas.0900336106.

(107) Lebard, D. N.; Matyushov, D. V. Protein-water electrostatics and principles of bioenergetics. *Phys. Chem. Chem. Phys.* **2010**, *12*, 15335. DOI: 10.1039/c0cp01004a.

(108) Friesen, A. D.; Matyushov, D. V. Non-Gaussian statistics of electrostatic fluctuations of hydration shells. *J. Chem. Phys.* **2011**, *135*, 104501. DOI: 10.1063/1.3633478.

(109) Martin, D. R.; Matyushov, D. V. Non-Gaussian statistics and nanosecond dynamics of electrostatic fluctuations affecting optical transitions in proteins. *J. Phys. Chem. B* **2012**, *116*, 10294. DOI: 10.1021/jp305757t.

(110) Friesen, A. D.; Matyushov, D. V. Surface polarity and nanoscale solvation. *J. Phys. Chem. Lett.* **2012**, *3*, 3685. DOI: 10.1021/jz301672e.

(111) Kang, T. J.; Yu, J.; Berg, M. Rapid solvation of a nonpolar solute measured by ultrafast transient hole burning. *Chem. Phys. Lett.* **1990**, *174*, 476.

(112) Saven, J. G.; Skinner, J. L. A molecular theory of the line shape: inhomogeneous and homogeneous electronic spectra of dilute chromophores in nonpolar fluids. *J. Chem. Phys.* **1993**, *99*, 4391.

(113) Fourkas, J. T.; Benigno, A.; Berg, M. Time-resolved nonpolar solvation dynamics in supercooled and low viscosity n-butylbenzene. *J. Chem. Phys.* **1993**, *99*, 8552.

(114) Fourkas, J. T.; Berg, M. Temperature-dependent ultrafast solvation dynamics in a completely nonpolar system. *J. Chem. Phys.* **1993**, *98*, 7773.

(115) Bagchi, B. Molecular theory of nonpolar solvation dynamics. *J. Chem. Phys.* **1994**, *100*, 6658.

(116) Ladanyi, B. M.; Stratt, R. M. Short-time dynamics of solvation: relationship between polar and nonpolar solvation. *J. Phys. Chem.* **1996**, *100*, 1266.

(117) Berg, M. A viscoelastic continuum model of nonpolar solvation. III. Electron solvation and nonlinear coupling effects. *J. Chem. Phys.* **1999**, *110*, 8577. DOI: 10.1063/1.478765.

(118) Yu, A.; Tolbert, C. A.; Farrow, D. A.; Jonas, D. M. Solvatochromism and solvation dynamics of structurally related cyanine dyes. *J. Phys. Chem. A* **2002**, *106*, 9407. DOI: 10.1021/jp0205867.

(119) Frisch, M. J.; Trucks, G. W.; Schlegel, H. B.; Scuseria, G. E.; Robb, M. A.; Cheeseman, J. R.; Montgomery, J. A., Jr; Vreven, T.; Kudin, K. N.; Burant, J. C.; Millam, J. M.; Iyengar, S. S.; Tomasi, J.; Barone, V.; Mennucci, B.; Cossi, M.; Scalmani, G.; Rega, N.; Petersson, G. A.; Nakatsuji, H.; Hada, M.; Ehara, M.; Toyota, K.; Fukuda, R.; Hasegawa, J.; Ishida, M.; Nakajima, T.; Honda, Y.; Kitao, O.; Nakai, H.; Klene, M.; Li, X.; Knox, J. E.; Hratchian, H. P.; Cross, J. B.; Bakken, V.; Adamo, C.; Jaramillo, J.; Gomperts, R.; Stratmann, R. E.; Yazyev, O.; Austin, A. J.; Cammi, R.; Pomelli, C.; Ochterski, J. W.; Ayala, P. Y.; Morokuma, K.; Voth, G. A.; Salvador, P.; Dannenberg, J. J.; Zakrzewski, V. G.; Dapprich, S.; Daniels, A. D.; Strain, M. C.; Farkas, O.; Malick, D. K.; Rabuck, A. D.; Raghavachari, K.; Foresman, J. B.; Ortiz, J. V.; Cui, Q.; Baboul, A. G.; Clifford, S.; Cioslowski, J.; Stefanov, B. B.; Liu, G.; Liashenko, A.; Piskorz, P.; Komaromi, I.; Martin, R. L.; Fox, D. J.; Keith, T.; Al-Laham, M. A.; Peng, C. Y.; Nanayakkara, A.; Challacombe, M.; Gill, P. M. W.; Johnson, B.; Chen, W.; Wong, M. W.; Gonzalez, C.; Pople, J. A. *Gaussian 03, Revision D.01*; Gaussian, Inc.: Wallingford, CT, 2004.

(120) Guo, X.; Bandyopadhyay, P.; Schilling, B.; Young, M. M.; Fujii, N.; Aynechi, T.; Guy, R. K.; Kuntz, I. D.; Gibson, B. W. Partial acetylation of lysine residues improves intraprotein cross-linking. *Anal. Chem.* **2008**, *80*, 951. DOI: 10.1021/ac701636w.

(121) Åberg, U.; Åkesson, E.; Alvarez, J.-L.; Fedchenia, I.; Sundström, V. Femtosecond spectral evolution monitoring the bond-twisting event in barrierless

isomerization in solution. *Chem. Phys.* **1994**, *183*, 269. DOI: 10.1016/0301-0104(94)00022-0.

(122) Xu, Q.-H.; Fleming, G. R. Isomerization dynamics of 1,1'-diethyl-4,4'-cyanine (1144C) studied by different third-order nonlinear spectroscopic measurements. *J. Phys. Chem. A* **2001**, *105*, 10187. DOI: 10.1021/jp011924r.

(123) Peteanu, L. A.; Schoenlein, R. W.; Wang, Q.; Mathies, R. A.; Shank, C. V. The first step in vision occurs in femtoseconds: complete blue and red spectral studies. *Proc. Natl. Acad. Sci. U.S.A.* **1993**, *90*, 11762. DOI: 10.1073/pnas.90.24.11762.

(124) Mathies, R. A.; Brito Cruz, C. H.; Pollard, W. T.; Shank, C. V. Direct observation of the femtosecond excited-state *cis-trans* isomerization in bacteriorhodopsin. *Science* **1988**, *240*, 777. DOI: 10.1126/science.3363359.

(125) Barkhuijsen, H.; de Beer, R.; van Ormondt, D. Improved algorithm for noniterative time-domain model fitting to exponentially damped magnetic resonance signals. *J. Magn. Reson.* **1987**, *73*, 553.

(126) Zhu, L.; Li, P.; Huang, M.; Sage, J. T.; Champion, P. M. Real time observation of low frequency heme protein vibrations using femtosecond coherence spectroscopy. *Phys. Rev. Lett.* **1994**, *72*, 301. DOI: 10.1103/PhysRevLett.72.301.